UiT The Arctic University of Norway

Andrei Karzhou

Acoustical properties of solid-liquid composites and related computational problems

A dissertation for the degree of Philosophiae Doctor

Faculty of Engineering Science and Technology
Department of Computer Science and Computational Engineering

May 2023

Preface

This thesis has been submitted in fulfillment of the requirements of the degree Philosophiae Doctor at UiT – The Arctic University of Norway, campus Narvik. The research presented in the thesis has been conducted between 2018 and 2023 at UiT – The Arctic University of Norway, campus Narvik, under the supervision of Klas Pettersson, and under co-supervision of Irina Pettersson and Rune Dalmo.

The thesis is a collection of four papers, presented in chronological order of writing. The common theme for them is sound propagation. The papers are preceded by an introductory chapter that relates them to each other and provides state-of-the-art and motivation for the work, as well as a chapter covering main approaches and methods used in the analysis.

Acknowledgements

First of all, I express my deepest gratitude to my main supervisor Klas Pettersson for giving me an opportunity to work under his supervision. I am very thankful to my co-supervisor Irina Pettersson for her knowledge, guidance and care through my study. I thank Rune Dalmo, my co-supervisor, for his support and help during the last years. I would like to give thanks to Larisa Beilina for introducing me to the topic of inverse problems. I am grateful to Børre Bang for his support and assistance throughout the project.

Secondly, I would like to extend my gratitude to the Department of Computer Science and Computational Engineering at UiT The Arctic University of Norway, and all my colleagues for creating a great working environment.

I also would like to thank University of Gävle and Chalmers University of Technology for the hosting and opportunities provided during the course of the project.

Last but not least, I'm very thankful to my wife Tatiana for her patience and believing in me, and my parents Natallia and Vladimir for their supporting through my life.

Andrei Karzhou

Narvik, May 10, 2023

List of Papers

PAPER I

A. Karzhou, I. Pettersson, and K. Pettersson. "Insertion loss of macro-perforated plates with viscoelastic filling". Submitted to *Acta Acustica*, 2023.

PAPER II

A. Karzhou. "An iterative FEM-scheme for a fluid-solid acoustic problem". Submitted to *AIP Conference Proceedings: Harmonic Analysis, related Function Spaces, and their Applications*, 2023.

PAPER III

K. Pettersson, A. Karzhou, and I. Pettersson. "A Feedforward Neural Network for Modeling of Average Pressure Frequency Response". Published in *Acoustics Australia, 50(2), 185–201 (2022)*.

PAPER IV

A. Karzhou, I. Pettersson, L. Beilina, and K. Pettersson. "Numerical validation of optimization approach for solution of coefficient inverse problem in pseudo-frequency domain", To appear in *Springer's conference proceeding Gas Dynamics with Applications in Industry and Life Sciences – On Gas Kinetic/Dynamics and Life Science Seminar, March 25—26, 2021 and March 17--18, 2022, Springer, Cham, Switzerland.*

Contents

List of Figures

Chapter 1

Introduction

This thesis concerns the study of acoustical performance and characterisation of solid-liquid composites. The main body of the thesis consists of four papers, I–IV. Paper I presents the results of the experimental work, the main goal of which is to perform a comparative study of the insertion loss for macro-perforated plates filled with viscoelastic material and layered solid-liquid composites. The interaction between the solid matrix and the viscous filling influences the acoustic behavior of the composite structure. In Paper II we address the acoustic fluid-solid interaction problem for plates with a rough surface, and propose an iterative method for numerical solution.

One of the fundamental tasks in acoustics is to model the sound pressure field under harmonic excitation. In most cases, the studied domain has a complex geometry. In the case when there is a need to study many different geometries, the computing of the harmonic sound pressure fields by means of solving the Helmholtz equation can quickly become unfeasible. In Paper III we apply a machine learning approach, and present a feedforward dense neural network for computing the average sound pressure over a frequency range. We demonstrate the effectiveness of this method for polygonal cylinders.

The sound waves propagation in fluid media is described by the wave equation with the corresponding boundary and initial conditions. Given the parameters of the medium, one can determine the acoustic pressure, which is called a direct task. One can also formulate a coefficient inverse problem: Given the acoustic pressure in some domain, we want to determine the wave speed function in the time-harmonic acoustic wave equation. In Paper IV we solve a coefficient inverse problem by employing the Lagrangian approach for the optimization of the Tikhonov functional.

In the next sections, we discuss the existing closely related results on the topic and describe the main contributions of the thesis.

1.1 Motivation and related works

Noise pollution across the globe affects millions of people. According to the European Environment Agency Report No 22/2019 [1], about 20% of Europe's population are exposed to long-term noise levels that are harmful to their health, that corresponds to more than 100 million people within Europe. Road traffic is traced

to about 80% of the noise problems. The sound baffles along the roads are often quite primitive structures, and the construction of such noise barriers apparently does not use modern physical or mathematical results. One of good examples of how science can help with it is the noise abatement wall [2]. The authors were able to increase the sound absorption of the wall by modifying its surface geometry and using a prefractal structure. It had led to increased interaction between acoustic waves and absorbing material.

In building acoustics, the sound insulation materials are typically formed as panels. They are used in construction of enclosing structures, cladding panels, etc. The panels ensure protection of residential premises from increased noise levels providing acoustic comfort for living quarters. Sound absorption materials find also applications in the construction of special rooms such as recording studios, meeting rooms and anechoic chambers. Sound insulation in passive security systems is of great importance. It serves to avoid interception and disclosure of oral communications through acoustic and/or vibroacoustic channels. The energy of the acoustic signal is dissipated in the traveling media, i.e. there is a transition of mechanical vibrations to heat, and the sound absorption occurs. This is the phenomenon of the irreversible transition of the energy of a sound wave into other forms of energy, in particular into heat. Absorption of sound occurs always whenever the sound waves propagate through a medium or meet the boundary between two media. Let us consider the slab shown in Figure 1.1.1.
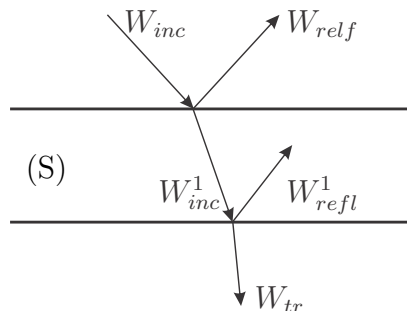
Figure 1.1.1: Transmission of a sound through the slab (S).

When sound waves with energy W_{inc} impinge on a interface between two media, a certain part of sound energy is reflected (W_{refl}). Then sound is transmitted and absorbed within the slab. In the end, the sound gets out of the slab carrying certain amount of energy W_{tr}. The absorption α, reflection β, transmission coefficient γ, and the sound insulation R are defined as follows:

$$\alpha = \frac{W_{\text{inc}} - W_{\text{refl}}}{W_{\text{inc}}}, \quad \beta = \frac{W_{\text{refl}}}{W_{\text{inc}}},$$

$$\gamma = \frac{W_{\text{tr}}}{W_{\text{inc}}}, \quad R = 10 \lg \frac{W_{\text{inc}}}{W_{\text{tr}}}.$$

The amount of sound energy transferred from one medium to another depends on the ratio of their acoustic impedances. The acoustic impedance Z is defined as the ratio of sound wave pressure p to the particle velocity v [3],

$$Z = \frac{p}{v}.$$

In room acoustics, one of the challenges is to provide a certain acoustic performance of multi-purpose auditoriums. In [4] the authors present a technique of variable sound absorption to control acoustic phenomena like reverberation, related to perception of sound. The idea is to utilize perforated systems to achieve variable solution for acoustic design of a room. There are two main approaches in variable acoustics: active and passive ones. The first approach is based on electronic control system. The sound field is captured and digitally processed to adjust reproduced sound. In passive variable acoustic approach, a large variation in sound absorption is required. It may be achieved by using specially designed curtains, movable reflectors, etc. In [4] the authors present an explored passive variable acoustic concept which could be used with automated control in multipurpose halls. The main idea is to use layered structure with movable parts (see Figure 1.1.2). This panel system has varying acoustic properties keeping the surface appearance constant.
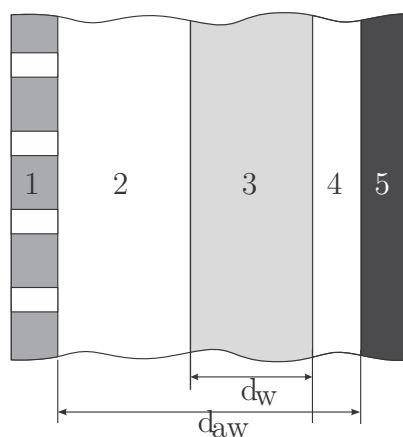
Figure 1.1.2: Cross-section of a layered structure: (1) perforated facing, (2) and (4) air, (3) mineral wool, (5) rigid surface. Tuning absorption is achieved by changing the position of the mineral wool (5) inside the air gap (2),(4).

During the last decades, the development and usage of composite materials in acoustics has become a must. In particular, in the design of sound-proof panels, the use of perforation is justified by the energy absorption due to the friction between the walls of the pores and the fluid, such as air or liquid. It is well-established that one can achieve a good damping of high frequencies using materials with very fine microstructure, such as porous materials [5]. Solid–liquid composites have been extensively studied for the last decades, and now, there are numerous examples where such structures show unexpected novel properties [6]. There is a great variation in form and dimension of the liquid inclusions, depending on the specific applications, including droplets, liquid networks, and isolated liquid inclusions. Solid-liquid composites find their applications in soft robotics, soft electronics, as well in chemical and biological systems.

Acoustic performance of micro- and macro-perforated screens are well studied both experimentally and numerically. Classical models for absorption and transmission coefficients for perforated screens and porous materials with perforated facings have been developed in [5, 7]. Modelling the porous media as an equivalent fluid,

acoustic characteristics are then written in terms of the effective density, bulk modulus, and acoustic impedance.

The geometry of the perforation might also affect the sound attenuation. For example, in [8] the authors study sound absorption for perforated panels with oblique perforations backed by an air cavity. It is shown that such geometry of the resonator leads to the increase of the effective thickness of the panel, essentially improving the low-frequency performance of the sound absorber. There are also studies addressing a possibility to increase the sound absorption by adding isolated masses in the poroelastic material. For example, [9] describes the effect of circular periodic inclusions on the sound absorption. In particular, this theoretical study shows that a structure with inclusions can possess a quasi-total absorption peak below the quarter-wavelength resonance frequency. Another example is the experimental study of the insertion loss for a poroelastic material with randomly placed inclusions [10]. The mass inclusions act as resonant systems, increasing the structure impedance, that leads to the increase in the insertion loss. It should be noted that the authors observe some reduction in the insertion loss at higher frequencies, but it is much less than the increases in the targeted bandwidth.

Inspired by the latter results, we decided to combine the idea of the perforation usage together with inclusions in order to investigate if it is possible to achieve higher sound reduction. To the best of our knowledge, such measurements have not been described in the literature. In Paper I, we have chosen to focus on one of the standard acoustic characteristics, the insertion loss, which is defined in terms of the sound pressure level and does not require the knowledge of the source strength. Due to this reason, the insertion loss is often used for comparison of sound insulation properties of different structures and materials. In Paper I, we perform a comparative experimental study for macro-perforated plates with the perforation filled with polyurethane and grease for the frequency range 200–3150 Hz.

The acoustic behaviour of the composite structure depends on the interaction between a solid matrix and a viscous filling, and it takes place on the interface between the two media. A coupled fluid-solid acoustic problem shows an interplay between structural deformations in the solid and the pressure load in the acoustic medium. In other words, acoustic waves in the fluid give rise to structural vibrations and vice versa. It is the interface interactions that determine the intensity of sound propagation in the structure. Moreover, the shape of the interface plays an important role for the sound propagation between fluid and solid parts. In [11] the authors consider closed resonators with absorbing properties and irregular geometry. It is shown that the geometrical irregularity of the absorbent material leads to the so-called "astride" mode localization. These localized modes determine the dissipation of the acoustic energy in the non-absorbing regions. In the noise abatement walls production, the geometry of the interface is an important factor, together with the speed of sound and the material-air density ratio [12]. One of the tasks in engineering design is to find an optimal shape for a structure susceptible to imposed constraints, as for example shape optimization in fluid-structure interaction problems (see e.g. [13, 14, 15]). There are many works devoted to the numerical methods for fluid-solid interaction acoustic problems. We refer to [16, 17, 18] and references therein. All these methods can be divided into monolithic and partitioned. In the monolithic

approach, the entire coupled system is solved simultaneously by using, e.g., the finite element method, see [19, 20, 21, 22, 23, 24]. As noted in [16], this approach might be more accurate for some multidisciplinary problems, but is often very computationally expensive, that is why the partitioned approach is often used. In such cases, the solid and fluid domains are considered as two computational domains with the interface conditions used explicitly as a coupling between the two domains. The partitioned approach is specially advantageous when the interface between the solid and fluid domains has a complicated structure. In Paper II we use the partitioned approach: We split the fluid-structure problem into fluid and structural subproblems and use separate solvers for these subproblems (see also [25]). There are several numerical PDE tools providing FEM calculations, e.g. FreeFem++ [26] (the one we have chosen for our computations) and FEniCS [27]. We verify the convergence of a suitable energy to confirm the convergence of the iteration scheme. The developed method is applied for a numerical comparative study of rough interfaces with different geometry. Namely, we compare the displacement on the side of the plate opposed to the fluid for five different periodic geometries: flat, squared, toothed, circles, and random. In this method, we divide the problem into fluid and solid subproblems, and solve them alternately, taking into account the conditions on common interface. The sound propagation in fluid part in the frequency domain is described by the wave equation. The behavior of the solid part is given by the solution of the elasto-dymanic equation. As the outcome we consider the frequency response of fluid-solid configuration.

In practice, perforated panels are often a part of more complex systems. In [4] the authors propose the layered structure for automated control of acoustic performance in multipurpose halls. The structure is formed by perforated facing backed by movable parts, and the geometry of air part can be complex. Modeling acoustics problems in building acoustics, vehicle interior noise problems, or noise reduction, requires computing average sound pressure, which in its turn is based on the computation of natural frequencies and the response to a dynamic excitation. This can be done in the time or in the frequency domain. Sound waves, as vibrations, are described by a time dependent wave equation, which can be reduced to a time independent Helmholtz equation by assuming harmonic dependence on time [28]. Moreover, it is sometimes necessary to model sound pressure field under harmonic excitation for many different geometries of fluid domain. In this case, solving Helmholtz equation may become too costly. On the other hand, application of machine learning methods in acoustics has made significant progress in recent years. A comprehensive overview of the recent advances is given in [29]. The frequency response problem, being the basis in modeling of acoustic problems, is not specifically addressed in [29], as any other combination of machine learning techniques and modeling with partial differential equations (PDEs).

In Paper III we consider a family of cylinders with the same height and varying cross-sections. We use five points defining the polygonal cylindrical domain. The idea is to build a neural network, which has the coordinates of five points on input, and the output is a scalar function giving the average pressure level over certain frequency range in the given domain. It turns out, that it is possible to construct such a neural network which predicts the scalar function for over 95% of the cases

with mean absolute error of 0.01 (the accuracy of the numerical data) if the training set includes 200,000 data points.

To find out how the sound propagates in a medium, and to determine the sound pressure, one needs to solve a time-dependent acoustic wave equation with the appropriate initial and boundary conditions. In this case, the material parameters of the medium must be known in advance. If the fluid medium is homogeneous and isotropic, then the speed of sound is constant. The presence of local changes in the material properties of the medium indicates that the latter contains heterogeneities. In turn, this means that the speed of sound waves becomes a function of the point. In many cases it is possible to reconstruct material parameters of the medium by solving an inverse problem. Namely, given the observed data in the bulk or on the boundary of the domain of interest, one determines the speed function (coefficient in the time-dependent wave equation). The inverse problem can be solved in time- and frequency domains. There are numerous practical applications of inverse problems, and in particular of the coefficient inverse problems. Among them are the subsurface imaging, nondestructive testing of materials and detection of landmines [30, 31, 32, 33], construction of photonic crystals [34] and cloaking materials [35], remote sensing and medical imaging [36, 37].

In Paper IV we reconstruct material parameters of the medium by solving an inverse problem given the observed data in the pseudo-frequency domain. This is a so-called coefficient inverse problem. We employ the Lagrangian approach for the optimization of the Tikhonov functional, that is similar to the one applied in [30, 38, 39] for the solution to time-dependent coefficient inverse problems. Most of the inverse problems appearing in natural sciences are ill-posed and unstable. In particular, it means that any arbitrarily small errors in the input data lead to large errors in the solution of the inverse problem. To overcome these difficulties, we have used a regularizing functional introduced by Tikhonov [40]. The essence of this regularization method is to add some additional (a priori) constraints in order to solve the ill-posed problem. For example, we may assume that the solution of the direct task has a certain degree of smoothness. In our work we consider several regularizing terms for different arrangements of inclusions. In the result, it becomes possible to provide reconstruction procedure. It turns out, that the approach gives a acceptable reconstruction even for very noisy data.

1.2   Summary of main results

In accordance with the objectives, the following has been carried out: an experimental study of the insertion loss for layered solid-liquid composites and macro-perforated plates filled with viscoelastic material. The experimental data have been processed, and a comparison of the data with existing models has been provided. In order to improve the computational methods for modeling of interaction of the solid framework of perforated panels with viscoelastic filler, an iterative scheme within fluid-solid interaction has been proposed and validated. A machine learning model to predict the average sound pressure for the domains with complex geometry has

been proposed and validated. The solution of an inverse problem for material heterogeneity recovery, based on the scattered acoustic field data in a computational domain, has been presented and evaluated.

Paper I

In this paper, we present a comparative experimental study of sound insertion loss for perforated plates with viscoelastic filling. The plates are made of steel and high density polyethylene. We use polyurethane and an emulsified oil lubricant as filling materials. In the first part of the experiment, we study the effect of the filling on the sound absorption for throughout filled perforation. The conclusion is that the insertion loss for both solid and perforated plates complies the mass law for most of the frequencies. However, we observe a considerable difference in the insertion loss for some narrow frequency ranges. For example, the insertion loss of 20 mm thick plastic plates with the polyurethane filling reveals the difference up to 17 dB compared with the solid plate, in the frequency range 1450–1600 Hz. The second part of the experiment is devoted to layered plates with viscoelastic inclusions. We have found that for most of the frequencies, the inserting a perforated layer with pseudoplastic filling (grease) between two solid plates without considerable changes in mass, results in the effective decrease of the insertion loss. For example, the mass of a layered sample with 10 mm filled perforated plate between the two solid plastic ones and of a 10 mm solid metal sample differ by about 2%. However,the difference in the sound insertion loss achieves 10 dB for frequencies in the range 800–1600 Hz. Similar results is for a solid 10 mm plastic sample and a layered 9 mm plastic sample with pseudoplastic inclusions, the difference in the insertion loss is more than 10 dB for frequencies 630–3150 Hz, for essentially the same mass.

Paper II

In Paper II, we present an iterative algorithm for solving a fluid-structure interaction problem under a harmonic excitation. We study the convergence of the iterative algorithm numerically, and apply the proposed algorithm for fluid-solid structures with different periodic, as well as random interface structure. Aiming to get an indication about the impact of the geometry on the sound damping, we calculate the L^2-norm of the displacement on the back side of the elastic plate. It has been found that all studied structures reveal a similar trend and similar values of the L^2-norm of the displacement in the solid part. However, for a few frequencies, the norm of the displacement for the random geometry is larger compared to periodic interface. For example, at the frequency $f_a = 860$ Hz, there is a peak in the displacement plot for all materials and interfaces. This peak is associated to the resonance in the fluid domain. We compute the cross energy on the interface, as well as the H^1-norms of the sound pressure and displacements in fluid and solid domains, respectively. The algorithm converges in all cases already after ten iterations.

Paper III

The sound pressure field in fluids under a harmonic load is modeled by the Helmholtz equation. If the objective of study is the harmonic sound pressure on the domains with many different geometries for wide ranges of frequencies, then solving the Helmholtz equation might quickly become too costly. In this paper, we consider polygonal cylinders, and proposed a feedforward dense neural network to predict the average sound pressure over a frequency range. To generate the data, we use finite elements, and numerically compute the frequency response of the average sound pressure by an eigenmode decomposition of the pressure. We evaluate the performance of the neural network. We provide the analysis for the accuracy of the approximation. The neural network predicts the average pressure level for over 95% cases with mean absolute error 0.01 (the accuracy of the numerical data) if the training set includes 200,000 data points.

Paper IV

The acoustic coefficient inverse problem (CIP) aims to reconstruct material parameters of the medium, in particular, to determine the wave speed function in the time-harmonic acoustic wave equation, if the scattered acoustic field is given in some domain or on its boundary. In Paper IV, we solve a CIP problem in the case when the data is given in the pseudo-frequency domain, after the Laplace transform of the time-dependent data. We utilize the Lagrangian approach for the minimization a time-independent Tikhonov functional. The main contribution of the paper is the numerical study of how the higher derivatives in the functional influence the reconstruction of the material parameters. We compare functionals with L^2, H^1, and H^2 regularizing terms for different positions of inclusions. In case of the penalty term being the square of the L^2-norm, the standard functional does not yield adequate reconstruction results. We obtain the best reconstruction for smooth data, with the functional containing second derivatives of the solution to the direct problem, along with the conjugate gradient method for the functional minimization. For noisy data, the best performance is achieved by means of H^1 functional in combination with suitable smoothing of the data and constraining of wave speed function during the reconstruction procedure.

1.3   Discussion and possible future research

The experimental results in Paper I evoke several questions. It should be noted that there are neither numerical studies nor theoretical models describing sound attenuation in solid-liquid composites even with such simple geometry as filled periodic perforation. As we have observed a deviation from the classical mass law for the particular choice of the pseudoplastic filling (shear-thinning fluids with the viscosity that decreases with increasing shear rate), it would be interesting to study, both experimentally and numerically, other kinds of liquid and pseudoplastic inclusions. It is also clear that the isolated inclusions give rise to a different acoustic behaviour

compared with the exposed (throughout) filled perforation. A theoretical model could help to explain the nature of this difference.

In Paper II we have compared several geometries for the rough interface between the solid and the fluid domains, including periodic and random interfaces. It has been shown that there are only a few frequencies in the studied frequency range for which the displacement on the back side of the plate differs for different geometries. On the other hand, [2] shows that the geometry does play an important role for the soundproof properties of a plate. Inspired by [2], a next step could be to apply the proposed iterative algorithm to a fluid-solid interaction problem with a prefractal geometry of the interface, and to prove the convergence analytically. A more ambitious goal is to use shape optimization technique in order to minimize the norm of the displacement on the back side of the plate.

The results in Paper III can be improved by using a more complex neural net. We expect that a convolutional neural net can give a better accuracy for less computational effort.

The coefficient inverse problem solved in Paper IV uses the data after the Laplace transform in the whole computational domain. The present algorithm, performing well even on noisy data in the bulk domain, in its current form, does not give an adequate reconstruction if the data is only given on the boundary of the computational domain. The next step would be to modify the algorithm in order to be able to reconstruct the wave speed function from the boundary data.

References

[1] The European Environment Agency. *Environmental noise in Europe — 2020.* Tech. rep. 2019. URL: https://www.eea.europa.eu/publications/environmental-noise-in-europe.

[2] B. Sapoval, M. Filoche, M. Chappat, and D. Peyrard. *Noise abatement wall.* US Patent 7,308,965. Dec. 2007.

[3] "Springer Handbook of Acoustics". In: ed. by T. D. Rossing. Springer New York, NY, 2007. DOI: 10.1007/978-0-387-30425-0.

[4] A. Pereira, A. Gaspar, L. Godinho, P. Amado Mendes, D. Mateus, J. Carbajo, J. Ramis, and P. Poveda. "On the Use of Perforated Sound Absorption Systems for Variable Acoustics Room Design". In: *Buildings* 11.11 (2021). DOI: 10.3390/buildings11110543.

[5] J.F. Allard and N. Atalla. *Propagation of Sound in Porous Media: Modelling Sound Absorbing Materials, Second Edition.* Dec. 2009, p. 358. ISBN: 9780470746615. DOI: 10.1002/9780470747339.

[6] R. W. Style, R. Tutika, J. Young Kim, and M. D. Bartlett. "Solid–liquid composites for soft multifunctional materials". In: *Advanced Functional Materials* 31.1 (2021), p. 2005804.

[7] N. Atalla, R. Panneton, F. C. Sgard, and X. Olny. "Acoustic absorption of macro-perforated porous materials". In: *Journal of sound and vibration* 243.4 (2001), pp. 659–678.

[8] J. Carbajo, S. Ghaffari Mosanenzadeh, S. Kim, and N. X. Fang. "Sound absorption of acoustic resonators with oblique perforations". In: *Applied Physics Letters* 116.5 (2020), p. 054101. DOI: 10.1063/1.5132886.

[9] J.-P. Groby, O. Dazel, A. Duclos, L. Boeckx, and L. Kelders. "Enhancing the absorption coefficient of a backed rigid frame porous layer by embedding circular periodic inclusions". In: *The Journal of the Acoustical Society of America* 130.6 (2011), pp. 3771–3780.

[10] M. R. F. Kidner, C. R. Fuller, and B. Gardner. "Increase in transmission loss of single panels by addition of mass inclusions to a poro-elastic layer: Experimental investigation". In: *Journal of Sound and Vibration* 294.3 (2006), pp. 466–472.

[11] S. Félix, B. Sapoval, M. Filoche, and M. Asch. "Enhanced wave absorption through irregular interfaces". In: *Europhysics Letters* 85.1 (Jan. 2009), p. 14003. DOI: 10.1209/0295-5075/85/14003.

[12] V. Kubytskyi, M. Filoche, and B. Sapoval. "Increased absorption due to localized resonances". In: *41st International Congress and Exposition on Noise Control Engineering 2012, INTER-NOISE 2012* 10 (Jan. 2012), pp. 8196–8203.

[13] N. Aghajari and M. Schäfer. "Efficient shape optimization for fluid–structure interaction problems". In: *Journal of Fluids and Structures* 57 (2015), pp. 298–313. ISSN: 0889-9746. DOI: 10.1016/j.jfluidstructs.2015.06.011.

[14] L. L. Chen, H. Lian, Z. Liu, H. B. Chen, E. Atroshchenko, and S. P. A. Bordas. "Structural shape optimization of three dimensional acoustic problems with isogeometric boundary element methods". In: *Computer Methods in Applied Mechanics and Engineering* 355 (2019), pp. 926–951. ISSN: 0045-7825. DOI: 10.1016/j.cma.2019.06.012.

[15] P. Kliewe, A. Laurain, and K. Schmidt. "Shape optimization in acoustic–structure interaction". In: *Engineering Computations* 39.1 (Jan. 2022), pp. 172–200. ISSN: 0264-4401. DOI: 10.1108/EC-07-2021-0379.

[16] Gene Hou, Jin Wang, and Anita Layton. "Numerical Methods for Fluid-Structure Interaction — A Review". In: *Communications in Computational Physics* 12.2 (2012), pp. 337–377. DOI: 10.4208/cicp.291210.290411s.

[17] G. Sandberg, P.-A. Wernberg, and P. Davidsson. "Fundamentals of Fluid-Structure Interaction". In: June 2009, pp. 23–101. ISBN: 978-3-211-89650-1. DOI: 10.1007/978-3-211-89651-8_2.

[18] H. J. Bungartz and M. Schäfer. *Fluid-Structure Interaction: Modelling, Simulation, Optimisation.* Lecture Notes in Computational Science and Engineering. Springer Berlin Heidelberg, 2007. ISBN: 9783540345961. URL: https://books.google.com.gi/books?id=-6NSKaCcGXkC.

[19] S. Marburg and B. Nolte. *Computational Acoustics of Noise Propagation in Fluids - Finite and Boundary Element Methods.* Mar. 2008. ISBN: 978-3-540-77447-1. DOI: 10.1007/978-3-540-77448-8_18.

[20] T. Richter. *Fluid-structure Interactions: Models, Analysis and Finite Elements.* Lecture Notes in Computational Science and Engineering. Springer International Publishing, 2017.

[21] G. Sandberg and R. Ohayon. *Computational Aspects of Structural Acoustics and Vibration.* Vol. 505. Jan. 2009. ISBN: 978-3-211-89650-1. DOI: 10.1007/978-3-211-89651-8.

[22] W. Zhao, L. Chen, H. Chen, and S. Marburg. "Topology optimization of exterior acoustic-structure interaction systems using the coupled FEM-BEM method". In: *International Journal for Numerical Methods in Engineering* 119.5 (2019), pp. 404–431. DOI: 10.1002/nme.6055.

[23] G. H. Yoon. "Unified Analysis with Mixed Finite Element Formulation for Acoustic-Porous-Structure Multiphysics System". In: *Journal of Computational Acoustics* 23.01 (2015), p. 1550002. DOI: 10.1142/S0218396X15500022.

[24] S. Zörner and M. Kaltenbacher. "Fluid–structure–acoustic interaction, Algorithms and implementation using the finite element method". In: *V European Conference on Computational Fluid Dynamics, ECCOMAS CFD 2010.* Lisbon, Portugal, 2010, pp. 879–888.

[25] M. R. Dörfel and B." Simeon. "Analysis and Acceleration of a Fluid-Structure Interaction Coupling Scheme". In: *Numerical Mathematics and Advanced Applications 2009.* Ed. by P. Kreiss G. and Lötstedt, A. Målqvist, and M. Neytcheva. Berlin, Heidelberg: Springer Berlin Heidelberg, 2010, pp. 307–315. ISBN: 978-3-642-11795-4.

[26] F. Hecht. "New development in FreeFem++". In: *J. Numer. Math.* 20.3-4 (2012), pp. 251–265. ISSN: 1570-2820. URL: https://freefem.org.

[27] M. S. Alnæs et al. "The FEniCS Project Version 1.5". In: *Archive of Numerical Software* 3.100 (2015). DOI: 10.11588/ans.2015.100.20553.

[28] E. Skudrzyk. *The foundations of acoustics: basic mathematics and basic acoustics.* Springer Science & Business Media, 2012.

[29] M. J. Bianco, P. Gerstoft, J. Traer, E. Ozanich, M. A. Roch, S. Gannot, and C.-A. Deledalle. "Machine learning in acoustics: Theory and applications". In: *The Journal of the Acoustical Society of America* 146.5 (2019), pp. 3590–3628.

[30] L. Beilina, N. T. Thanh, M. V. Klibanov, and J. B. Malmberg. "Reconstruction of shapes and refractive indices from backscattering experimental data using the adaptivity". In: *Inverse Problems* 30.10 (2014), p. 105007.

[31] A. V. Kuzhuget, L. Beilina, M. V. Klibanov, Anders Sullivan, Lam Nguyen, Michael A Fiddy, ARL Team, et al. "Blind backscattering experimental data collected in the field and an approximately globally convergent inverse algorithm". In: *Inverse Problems* 28.9 (2012), p. 095007.

[32] N. T. Thanh, L. Beilina, M. V. Klibanov, and M. A. Fiddy. "Reconstruction of the refractive index from experimental backscattering data using a globally convergent inverse method". In: *SIAM Journal on Scientific Computing* 36.3 (2014), B273–B293.

[33] N. T. Thanh, L. Beilina, M. V. Klibanov, and M. A. Fiddy. "Imaging of buried objects from experimental backscattering time-dependent measurements using a globally convergent inverse algorithm". In: *SIAM Journal on Imaging Sciences* 8.1 (2015), pp. 757–786.

[34] J. D. Joannopoulos, S. G. Johnson, J. N. Winn, and R. D. Meade. "Molding the flow of light". In: *Princet. Univ. Press. Princeton, NJ [ua]* (2008).

[35] A. Greenleaf, Y. Kurylev, M. Lassas, and G. Uhlmann. "Cloaking devices, electromagnetic wormholes, and transformation optics". In: *SIAM review* 51.1 (2009), pp. 3–33.

[36] M. Pastorino. *Microwave imaging.* John Wiley & Sons, 2010.

[37] O. Scherzer. *Handbook of mathematical methods in imaging.* Springer Science & Business Media, 2010.

[38] L. Beilina. "Domain decomposition finite element/finite difference method for the conductivity reconstruction in a hyperbolic equation". In: *Communications in Nonlinear Science and Numerical Simulation* 37 (2016), pp. 222–237.

[39] J. B. Malmberg and L. Beilina. "An Adaptive Finite Element Method in Quantitative Reconstruction of Small Inclusions from Limited Observations". In: *Appl. Math* 12.1 (2018), pp. 1–19.

[40] A. N. Tikhonov. "On the solution of ill-posed problems and the method of regularization". In: *Doklady akademii nauk.* Vol. 151. 3. Russian Academy of Sciences. 1963, pp. 501–504.

Chapter 2

Approaches and Methods

In this chapter we present methods and approaches for experimental studies of sound attenuation in panels and concomitant computational problems. We describe shortly the mass law for the insertion loss, and some impedance models for perforated screens. Then we introduce functional spaces and variational methods, as well as sensitivity analysis with shape derivatives. Finally, we describe the machine learning approach focusing on the stochastic gradient descent optimizer ADAM.

2.1 Experimental study of sound attenuation

There are several classical techniques to study sound attenuation experimentally. In room acoustics, the standard technique for measurement of the sound transmission loss (TL) is given in [1] and [2]. These standards require entering two rooms with separating frame where the studied specimen is mounted. Then the specimen is exposed to the diffuse acoustic field excitation in the reverberant source room. One measures the average sound pressure level in both receiving and source rooms, as well as the reverberation time in the receiving room. Then the TL is derived based on the pressure-pressure calculations. There is another way to derive the TL, which is based on the pressure-intensity calculations. In this case, the measurement of the sound pressure level in the source room and the sound intensity on the receiving side are required [3, 4].

A procedure for measurement of the absorption coefficient is described in [5]. This standard requires diffuse field conditions in the reverberant room. The sample area should be between 10 m^2 and 12 m^2. Another approach is to measure the absorption coefficient under normal incidence using a wave tube [6]. The classical Brüel & Kjær Impedance Tube Kit type 4206 [7] allows to measure samples of two possible diameters: 29 mm and 100 mm, in the frequency range 50 Hz to 6.4 kHz.

In Paper I we present the insertion loss (IL) measurements done in a much more flexible experimental setup. We measure the IL for different solid-liquid composites with the one for solid plates. The experimental results are then compared with the theoretical models, in particular, with the classical mass law model presented below.

2.1.1 Mass law

Any sound barrier (panel) inserted in the acoustic field change it in some way. For a relatively wide frequency range above the first panel resonance, the surface density of the panel determines its transmission loss. The upper limit of the frequency range is defined by the critical frequency f_c, at which the wave coincidence phenomenon is encountered.

The transmission loss TL or sound reduction index for large panels in the diffusive incident field depends on surface mass density of the plate μ in $\mathrm{kg\,m^{-2}}$, angular frequency ω in $\mathrm{rad\,s^{-1}}$, and characteristic impedance of the surrounding media $\rho_0 c$ in $\mathrm{Pa\,m^{-1}\,s}$ as follows [8]:

$$\mathrm{TL} = 20 \log_{10}\left(\frac{\mu\omega}{2\rho_0 c}\right) - 10 \log_{10}\left(\ln\left[1 + \left(\frac{\mu\omega}{2\rho_0 c}\right)^2\right]\right), \qquad (2.1.1)$$

where ρ_0 and c are the mass density in $\mathrm{kg\,m^{-3}}$ and speed of sound in $\mathrm{m\,s^{-1}}$ in the fluid medium, correspondingly.

The second term in (2.1.1) is a slowly varying function of the frequency. Moreover, in practice, the following formula for the sound transmission loss is used [8]:

$$\mathrm{TL} \approx 20 \log_{10}\mu + 20 \log_{10}f - 47. \qquad (2.1.2)$$

In the case of normal incidence in air, the acoustic behaviour of the single leaf panel is given by

$$\mathrm{TL}_n \approx 20 \log_{10}(\mu f) - 42, \qquad (2.1.3)$$

where f denotes frequency, μ the mass per unit area of the panel in $\mathrm{kg\,m^{-2}}$.

Formulae (2.1.1) and (2.1.3) represent the so-called mass law for $f << f_c$. The mass law shows the quasilinear dependence of the transmission loss on the mass of the panel. According to (2.1.1), (2.1.3) the transmission loss is complemented by 6 dB per octave. Another view on the mass law is that doubling of the mass of a plate yields approximately 6 dB reduction in the level of sound transmitted through the plate (see Figure 2.1.1).

For the frequencies above the critical one $f > f_c$, the transmission loss for single leaf panels starts to deviate from the mass law. In the case of diffusive incident field TL is written as

$$\mathrm{TL} = 20 \log_{10}(\mu f) + 10 \log_{10}\frac{f}{f_c} + 10 \log_{10}\eta + 5 \log_{10}\left(1 - \frac{f_c}{f}\right) - 47, \qquad (2.1.4)$$

where η is the loss factor defined by the bending stiffness of the plate D as $D = D_0(1 + i\eta)$. The radiation losses should also be added to the total loss. For frequencies $f > f_c$, the radiation losses can be calculated as follows:

$$\eta_{rad} = \frac{\rho_0 c}{\omega\mu\sqrt{1 - f_c/f}},$$

with $\omega = 2\pi f$ being the angular frequency. It should be noted that for plate of finite size separating closed spaces, the effect of the boundary conditions can affect the sound transmission through the plate [8].
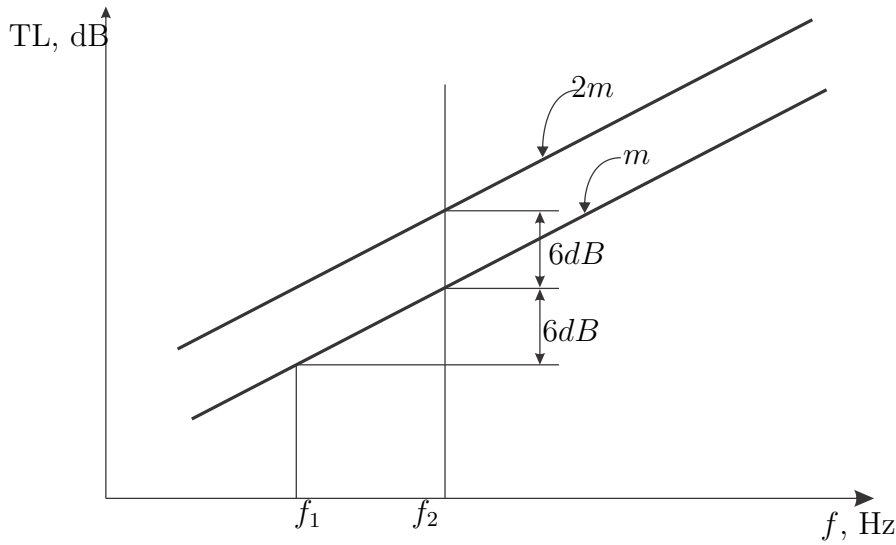
Figure 2.1.1: Mass law: doubling either the weight of the panel or the frequency brings a 6 dB increase in transmission loss.

2.1.2 Impedance approach for perforated screens

Describing the sound attenuation of perforated plates requires a different approach. Namely, the perforated plates do not follow the mass law. A unified approach for macro-perforated plates based on calculating the impedance of the plate, is presented in [9]. The main idea is to evaluate the normal surface impedance of the perforated plate based on the surface impedance of a single perforation. The panel can be backed either by a semi-infinite fluid (air in our case) or by a cavity.

In the model developed in [9], the plates with throughout perforation are described in terms of an equivalent fluid based on the Johnson–Allard's theory of porous media, taking into account equivalent tortuosity, that is the ratio of actual flow path length to the straight distance between the ends of the flow path. When the sound impinges the perforated panel, the distortion of the air flow occurs in a small region around the perforation. It turns out that in order to take into account this flow distortion, one needs to correct the tortuosity of the perforated panel. The correction of the tortuosity must be provided in accordance with the media in which the perforated system emits sound waves. The tortuosity is modified by the correction term which is a function of the correction length ϵ_e. The latter is connected to the radiation of a circular piston in free air as well as to the tortuosity of the medium in which the perforated panel radiates.

Different perforated systems considered in [9] are shown in Figure 2.1.2, and the corresponding equivalent tortuosities are given in (2.1.5), (2.1.6), and (2.1.7) below.

$$\alpha_\infty^a(\omega) = 1 + \frac{2\epsilon_e}{d}, \tag{2.1.5}$$

$$\alpha_\infty^b(\omega) = 1 + \frac{2\epsilon_e}{d}, \tag{2.1.6}$$

$$\alpha_\infty^c(\omega) = 1 + \frac{2\epsilon_e}{d}\left(1 + Re(\tilde{\alpha}_p)\right), \tag{2.1.7}$$
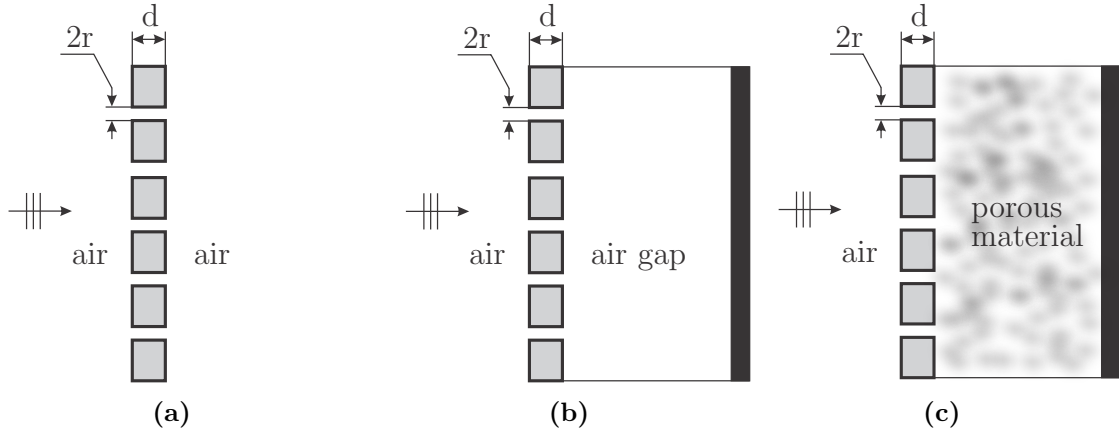
Figure 2.1.2: Perforated systems: (a) a perforated panel coupled with a semi-infinite fluid medium, (b) a perforated plate backed by a cavity, and (c) a perforated plate in contact with a rigid frame porous layer.

where $Re(\tilde{\alpha}_p)$ is the real part of the dynamic tortuosity of the porous layer.
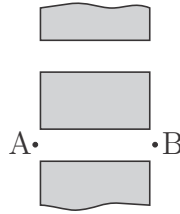
Figure 2.1.3: Cut through perforation.

The general model developed in [9], leads to different expressions for the total input impedance Z_A (see Figure 2.1.3) for each perforated systems shown in Figure 2.1.2.

For the case of macro-perforated plate coupled with a semi-infinite fluid medium (air) as shown in Figure 2.1.2(a), in front of the perforated panel the impedance Z_A^a is as follows

$$Z_A^a = j\frac{\omega\rho_0}{\phi}d\alpha_\infty^a\left(1+\frac{\alpha_\infty^a}{4}\right) + \sigma d + Z_B^a, \qquad (2.1.8)$$

where ω is angular frequency, ρ_0 is the air density, ϕ is the porosity of the perforated plate, σ is the flow resistivity, Z_B^a is the free air impedance.

For the case of perforated-air layer combination shown in Figure 2.1.2(b):

$$Z_A^b = 2(2\epsilon_e + d)\frac{R_s}{r\phi} + j(2\epsilon_e + d)\frac{\omega\rho_0}{\phi} + Z_B^b, \qquad (2.1.9)$$

where r is the radius of perforation, $R_s = 0.5\sqrt{2\eta\omega\rho_0}$ denotes the surface resistance with the dynamic viscosity of air η, $Z_B^b = -j\rho_0c_0\cot(\frac{\omega}{c_0}L)$ is the normal surface impedance of the air layer with the thickness L and speed of sound c_0.

For the case of perforated plate in contact with porous layer backed by a rigid wall (Figure 2.1.2(c)):

$$Z_A^c = \frac{1}{\phi}(\epsilon_e(1 + Re(\tilde{\alpha}_p)) + d)j\omega\rho_0 + \frac{Z_{0,0}(B)}{\phi_p}, \qquad (2.1.10)$$

where $Z_{0,0}(B) = -jZ_c\cot(k_pL)$ with characteristic impedance Z_c and wave number k_p in material with porosity ϕ_p.

2.2 Functional Spaces and Variational methods

In this section we give a brief introduction to the Sobolev spaces, describe the idea of weak formulation, and present the key results used in Chapters II–IV. The presentation highlights only the essential definitions and propositions used in the following chapters. We follow the books [10], [11], and [12].

Classically, many physical quantities, like the temperature in a rod or the displacement of a beam from its equilibrium position, are modelled by partial differential equations satisfied in each point of the domain of interest. Modern numerical methods for solving partial differential equations, such as the finite element method, the finite volume method, the gradient discretization method, etc., make use of the variational approach, and rather analyze the integrals of functions describing such quantities with appropriate test functions, and not the values of these functions at each point. To allow for certain discontinuities of the data and the solutions, one needs to extend functional spaces, introduce a notion of weak derivative, and provide a weak formulation of the problem. Moreover, depending on the order of the differential equation, classical solutions require several continuous derivatives of the solution (second-order derivatives for heat equation and fourth-order derivatives for beam bending problems). The variational approach reduces the solution's smoothness requirements.

Indeed, let us study a simple example. Consider a one-dimensional composite material (one can think about a thin rod with length 1) made of two parts with different conductivity. In other words, the conductivity is modelled as a piecewise function:

$$a(x) = \begin{cases} 1, & 0 \le x \le 0.5, \\ 2, & 0.5 < x \le 1. \end{cases}$$

Consider the Dirichlet boundary value problem for a heat equation in this rod:

$$\begin{cases} (a(x)u'(x))' = 0, & x \in (0,1), \\ u(0) = 0, \; u(1) = 1. \end{cases} \qquad (2.2.1)$$

Here $u(x)$ is interpreted as the temperature at point $x \in [0,1]$, and the Dirichlet boundary conditions decide the temperature at the ends of the rod. Integrating equation (2.2.1) once, we see that the first derivative u' is discontinuous:

$$u'(x) = \frac{C}{a(x)} = \begin{cases} C, & 0 \le x \le 0.5, \\ C/2, & 0.5 < x \le 1, \end{cases}$$

where C is a constant. Consequently, $u(x)$ is not two times continuously differentiable, and a classical solution to problem (2.2.1) does not exist. To get the solution of boundary value problem (2.2.1), one needs to reformulate it in terms of differentiable in weak sense functions. In this case the functional space for problem (2.2.1) is the Sobolev space $H^1(0, 1)$ of square integrable functions with square integrable derivatives.

2.2.1 Functional spaces

Throughout the current section, Ω is an open set in $\mathbf{R}^d$ with a Lipschitz boundary $\partial\Omega$.

We denote by $L^2(\Omega)$ the set of measurable square (Lebesgue) integrable functions in Ω with the scalar product

$$(u, v)_{L^2(\Omega)} = \int_\Omega u(x)v(x)\,dx.$$

The corresponding norm is $\|u\|_{L^2(\Omega)} = (\int_\Omega |u|^2\,dx)^{1/2}$.

Let $C_0^\infty(\Omega)$ be a set of infinitely many times differentiable functions with compact support. A function from this space $\varphi \in C_0^\infty(\Omega)$ is called a test function. One of the most important statements in the calculus of variations is the du Bois-Reymond lemma.

Lemma 2.2.1. *Let $f \in L^2(\Omega)$. If for any $\varphi \in C_0^\infty(\Omega)$ we have*

$$\int_\Omega f(x)\varphi(x)\,dx = 0,$$

then $f(x) = 0$ almost everywhere in Ω, that is there exists a subset $E \subset \Omega$ such that the Lebesgue measure of it is zero and $f = 0$ in $\Omega \setminus E$.

Proof. Using the density of smooth functions $C_0^\infty(\Omega)$ in $L^2(\Omega)$ (see [13]), one can construct a sequence $f_n \in C_0^\infty(\Omega)$ converging to f in $L^2(\Omega)$, that is $\lim_{n\to\infty} \|f - f_n\|_{L^2(\Omega)} = 0$. Then, by the assumption,

$$0 = \lim_{n\to\infty} \int_\Omega f(x)f_n(x)\,dx = \int_\Omega |f(x)|^2\,dx,$$

that yields $f(x) = 0$ almost everywhere. $\qquad\square$

Now define the weak derivative in $L^2(\Omega)$.

Definition 2.2.2. We say that $u \in L^2(\Omega)$ is differentiable in the weak sense if there exist $v_i \in L^2(\Omega)$, $i = 1, \ldots, d$, such that

$$\int_\Omega u(x)\partial_{x_i}\varphi(x)\,dx = -\int_\Omega v_i(x)\varphi(x)\,dx,$$

where $\partial_{x_i}\varphi(x)$ is the partial derivative of φ with respect to x_i. We write $v_i = \partial_{x_i}u(x)$.

Clearly, if u is differentiable in the classical way, it is also possesses weak derivatives, which coincide with the classical (strong) ones. Weak derivatives can also be defined for $u \in L^1_{loc}(\Omega)$, locally integrable in Ω functions. A weak derivative, if it exists, is unique up to a set of measure zero (see [10]). Having defined the weak derivative, we can also introduce differential operators as divergence.

Definition 2.2.3. Consider a vector-valued function $u : \Omega \to \mathbf{R}^d$. We say that $w \in L^2(\Omega)$ is the divergence of u and write $w = \operatorname{div} u$ if

$$\int_\Omega u(x) \cdot \nabla \varphi(x) \, dx = - \int_\Omega w(x) \varphi(x) \, dx,$$

for any function $\varphi \in C_0^\infty(\Omega)$.

Now we can introduce the Sobolev spaces.

Definition 2.2.4. The space $H^1(\Omega)$ consists of all functions $u \in L^2(\Omega)$ such that $\partial_{x_i} u \in L^2(\Omega)$, $i = 1, \ldots, d$.

We define a norm in $H^1(\Omega)$ by

$$\|u\|_{H^1(\Omega)} = \left(\int_\Omega (|u|^2 + |\nabla u|^2) \, dx \right)^{1/2}.$$

The space $H_0^1(\Omega)$ is defined as the closure of $C_0^\infty(\Omega)$ in $H^1(\Omega)$. For continuously differentiable in Ω functions u it means simply that $u = 0$ on the boundary $\partial\Omega$.

For functions continuous in some domain containing Ω, it is straightforward to define the value on the boundary. For a general function from $L^2(\Omega)$, the value at a particular point is not defined since the functions are now defined up to a set of measure zero. The trace theorem allows one to define the trace of a $H^1(\Omega)$ function u on the boundary $\partial\Omega$ and prove that $u\big|_{\partial\Omega} \in L^2(\partial\Omega)$. Actually, a stronger result holds saying that the trace of a $H^1(\Omega)$ function belongs to a subset of $L^2(\Omega)$, which is denoted by $H^{1/2}(\Omega)$.

A mapping from some functional space to $\mathbf{R}$ (or $\mathbf{C}$) is called a functional. For example, $F(u) = \int_\Omega |\nabla u|^2 \, dx$ is a real-valued functional defined on $H^1(\Omega)$. The space of all linear continuous functionals on $H_0^1(\Omega)$ is called the dual space and is denoted by $H^{-1}(\Omega)$.

Another important result concerns the normal derivative of a $H^1(\Omega)$ function on the boundary $\partial\Omega$. Namely, given $u \in H^1(\Omega)$ such that $\Delta u \in L^2(\Omega)$, the normal derivative is $\nabla u \cdot n \in H^{-1/2}(\partial\Omega)$, where $H^{-1/2}(\partial\Omega)$ is the dual space of $H^{1/2}(\partial\Omega)$. The normal derivative is in this case defined by the duality

$$\langle \nabla u \cdot n, v \rangle := \int_{\partial\Omega} (\nabla u \cdot n) \, v \, d\sigma = \int_\Omega (v \Delta u + \nabla u \cdot \nabla v) \, dx.$$

In Paper II we use the Sobolev spaces and the trace theorem in order to write down a weak formulation of problem (II.2.7).

In Paper IV we see an example of a distribution, which is not a regular function, namely a delta function $\delta(t)$. We also define its weak derivative $\delta'(t)$ and show how to approximate it by piecewise smooth functions. The delta function $\delta(t)$ is an element of $H^{-1}(\Omega)$ and is the weak derivative of the Heaviside function (which otherwise is not differentiable).

2.2.2 Weak formulation and functional derivatives

In this section we sketch the variational approach for a scalar elliptic problem. Similar arguments are used in Paper II for a fluid-solid interaction problem where a linear elasticity system is coupled with a Stokes equation, in Paper III for an eigenvalue problem for the Laplace operator, and in Paper IV for an elliptic partial differential equation obtained by the Laplace transform of the time-dependent problem.

As a model problem, we consider a Dirichlet boundary value problem for a second-order elliptic operator with variable coefficients in divergence form:

$$-\text{div}(A(x)\nabla u(x)) = f(x), \quad x \in \Omega, \tag{2.2.2}$$

$$u = 0, \quad x \in \partial\Omega. \tag{2.2.3}$$

We assume that $f \in L^2(\Omega)$ and $A(x)$ is a measurable scalar function such that for almost all $x \in \Omega$,

$$0 < A^- \leq A(x) \leq A^+.$$

The weak formulation of (2.2.2) is obtained by multiplying (2.2.2) by a smooth test function $v \in C_0^1(\Omega)$ and integrating by parts using the Green formula:

$$\int_\Omega A(x)\nabla u \cdot \nabla v \, dx = \int_\Omega fv \, dx. \tag{2.2.4}$$

By density of $C_0^1(\Omega)$ in $H_0^1(\Omega)$ (see [11]), we extend the test function space to $H_0^1(\Omega)$. The weak (variational) formulation reads: Find $u \in H_0^1(\Omega)$ such that (2.2.4) is satisfied for any $v \in H_0^1(\Omega)$. It is convenient to write (2.2.4) is a shorter form:

$$a(u, v) = l(v),$$

where $a(u, v) = \int_\Omega A\nabla u \cdot \nabla v \, dx$ is a bilinear form on $H_0^1(\Omega)$, and $l(v) = \int_\Omega fv \, dx$ is a linear continuous functional on $H_0^1(\Omega)$.

Given a Hilbert space H, a bilinear form $a : H \times H \to \mathbf{R}$ is called continuous if there exists a constant C such that

$$|a(u, v)| \leq C\|u\|_H \|v\|_H, \quad \forall u, v \in H.$$

The bilinear form is called coercive if there exists a constant $C_0 > 0$ such that

$$a(u, u) \geq C_0\|u\|_H, \quad \forall u \in H.$$

The existence and uniqueness of a solution is established by the Lax-Milgram lemma (see Corollary 5.8 in [11]).

Lemma 2.2.5. *Let $a(u, v)$ be a continuous coercive bilinear form on H (Hilbert space), and let $f \in H^*$, with H^* being the dual space. There exists a unique $u \in H$ such that $a(u, v) = l(v)$ for any $v \in H$.*

Moreover, if the bilinear form a is symmetric, then u is a unique minimizer of

$$\min_{v \in H} F(v) = \min_{v \in H} \left(\frac{1}{2}a(v, v) - l(v)\right).$$

We compute the the directional (Gateaux-) derivative of the functional F at u in the direction of v:

$$
\begin{aligned}
\lim_{\varepsilon \to 0} \frac{F(u + \varepsilon v) - F(u)}{\varepsilon} &= \frac{d}{d\varepsilon} F(u + \varepsilon v)\big|_{\varepsilon=0} \\
&= \frac{d}{d\varepsilon} \Big[\frac{1}{2} \int_\Omega A\nabla u \cdot \nabla u \, dx - \int_\Omega fv \, dx \\
&\quad + \varepsilon \int_\Omega A\nabla u \cdot \nabla v \, dx - \varepsilon \int_\Omega fv \, dx + \frac{\varepsilon^2}{2} \int_\Omega A\nabla v \cdot \nabla v \, dx \Big]\big|_{\varepsilon=0} \\
&= \Big[\varepsilon \int_\Omega A\nabla u \cdot \nabla v \, dx - \varepsilon \int_\Omega fv \, dx + \frac{\varepsilon^2}{2} \int_\Omega A\nabla v \cdot \nabla v \, dx \Big]\big|_{\varepsilon=0} \\
&= \int_\Omega A\nabla u \cdot \nabla v \, dx - \int_\Omega fv \, dx.
\end{aligned}
$$

The point $u \in H$ is critical if the directional derivative is zero, that is u satisfies (2.2.4) for any $v \in H$.

Another type of functional derivative is the Fréchet derivative.

Definition 2.2.6. A functional $F : H \to \mathbf{R}$ is Fréchet differentiable at the point u if there exists a linear map $F'(u) \in H^*$ (differential of F at u) such that

$$
\lim_{\|v\|_H \to 0} \frac{|F(u + v) - F(u) - F'(u)v|}{\|v\|_H} = 0.
$$

The differentiability of a functional depends crucially on its growth. The following lemma (see Appendix C.1 in [14]) applies to the integral functionals of the type

$$
F(u) = \int_\Omega G(x, u(x), \nabla u(x)) \, dx,
$$

and in particular, to the functionals J_{L^2}, J_{H^1} in Paper IV.

Lemma 2.2.7. *Assume that the function $G : \Omega \times \mathbf{R} \times \mathbf{R}^d \to \mathbf{R}$ is measurable in $x \in \Omega$, continuously differentiable in $u \in \mathbf{R}$ and $p \in \mathbf{R}^d$, and the following growth conditions are satisfied:*

- *$|G(x, u, p)| \leq C(1 + |u|^{s_1} + |p|^2)$, where $s_1 \leq 2d/(d-2)$ for $d \geq 3$.*

- *$|\partial_u G(x, u, p)| \leq C(1 + |u|^{s_2} + |p|^{t_2})$ with $t_2 < 2$ if $d \leq 2$, and $s_2 \leq (d+2)/(d-2), t_2 \leq (d+2)/d$ if $d \geq 3$.*

- *$|\partial_p G(x, u, p)| \leq C(1 + |u|^{s_3} + |p|)$ with $s_3 \leq d/(d-2)$ if $d \geq 3$.*

Then the functional F is Fréchet differentiable, and the derivative is given by

$$
\langle F'(u), v \rangle = \int_\Omega (\partial_u G(x, u, \nabla u)v + \partial_p G(x, u, \nabla u) \cdot \nabla v) \, dx.
$$

If the functional F is Fréchet differentiable with the Fréchet derivative $F'(u)$, then

$$
\frac{d}{d\varepsilon} F(u + \varepsilon v)\big|_{\varepsilon=0} = \langle F'(u), v \rangle = F'(u)v.
$$

2.3   Sensitivity Analysis

In Paper IV we will differentiate functionals with respect to the coefficient $a(x)$. It is the so-called derivatives with respect to the design. Following the ideas in Section 2.2 of [15], we will show how the derivative with respect to the design is computed in our particular case of functional (IV.3.2). Namely, let us consider the following mixed boundary value problem:

$$\Delta u - s^2\, a(x) u(x) = 0, \quad x \in \Omega, \tag{2.3.1}$$
$$\nabla u \cdot \nu + su = s, \quad x \in \partial\Omega.$$

Problem (2.3.1) is obtained by applying the Laplace transform to a time-dependent wave equation. The weak form (2.3.1) reads: Find $u \in H^1(\Omega)$ such that

$$a_a(u,v) = \int_\Omega \nabla u \cdot \nabla v\, dx + \int_\Omega s^2 auv\, dx + \int_{\partial\Omega} suv\, d\sigma = \int_{\partial\Omega} sv\, d\sigma, \quad \forall v \in H^1(\Omega). \tag{2.3.2}$$

Here we indicate the dependence on a explicitly by setting a subindex in the bilinear form. The coefficient inverse problem consists in recontructing the coefficient $a(x)$ given the observed data $\widetilde{u}$ in the domain Ω. To this end, as described in Paper IV, we minimize a Tikhonov functional, and one of the choices is

$$J_{H^1}(a) = J_{H^1}(u(a), a) = \frac{1}{2}\int_\Omega (u - \widetilde{u})^2 + \frac{1}{2}\int_\Omega |\nabla(u - \widetilde{u})|^2\, dx + \frac{\gamma}{2}\int_\Omega (a-1)^2\, dx. \tag{2.3.3}$$

Here $u = u(a)$ solves (2.3.1) for a given $a(x)$, and $\gamma > 0$ is a constant. Our current goal is to compute the Fréchet derivative of $J_{H^1}(a)$ with respect to the coefficient a (called the design in this case). The proof of the differentiability of the bilinear form $a_a(u,v)$ can be found in [15], Section 2.4, it is rather technical, and is not addressed here. We focus on using the methods and results for our particular case. Namely, we prove the following lemma.

Lemma 2.3.1. *The Fréchet derivative of $J_{H^1}(a)$ at point a in the direction of δa is given by*

$$J'_{H^1}(a)\delta a = \int_\Omega (-s^2 u\lambda + \gamma(a-1))\, \delta a\, dx, \tag{2.3.4}$$

where λ solves the adjoint problem

$$a_a(\lambda, v) = \int_\Omega (u - \widetilde{u})v\, dx + \int_\Omega \nabla(u - \widetilde{u}) \cdot \nabla v, \quad \forall v \in H^1(\Omega), \tag{2.3.5}$$

with the bilinear form $a_a(\lambda, v)$ defined in (2.3.2).

Proof. We start by computing the variation of the functional $J_{H^1}(a)$:

$$\frac{d}{d\tau} J_{H^1}(u(a + \tau\delta a), a + \tau\delta a)\Big|_{\tau=0}$$
$$= \int_\Omega (u - \widetilde{u})u'_a\, dx + \int_\Omega \nabla(u - \widetilde{u}) \cdot \nabla u'_a\, dx + \gamma \int_\Omega (a-1)\delta a\, dx.$$

Obviously, the derivatives with respect to the design (coefficient a) u'_a and $\nabla u'_a$ depend on the direction of the change in design δa. The derivative u'_a is the first variation of the solution u at design a in the direction of the design change δa is defined by

$$u'_a = \frac{d}{d\tau} u(a + \tau \delta a) \Big|_{\tau=0}.$$

Our goal is to obtain an explicit expression for the variation of the functional without u'_a and $\nabla u'_a$. To do so, we introduce an adjoint variable λ solving (2.3.5). Then the terms containing u'_a and $\nabla u'_a$ in the variation of the functional will take the form

$$\int_\Omega (u - \widetilde{u}) u'_a \, dx + \int_\Omega \nabla(u - \widetilde{u}) \cdot \nabla u'_a \, dx = a_a(\lambda, u'_a).$$

Since the bilinear form is symmetric, we have $a(\lambda, u'_a) = a(u'_a, \lambda)$, and the variation of $J_{H^1}(a)$ becomes

$$\frac{d}{d\tau} J_{H^1}(u(a + \tau \delta a), a + \tau \delta a) \Big|_{\tau=0} = a_a(u'_a, \lambda) + \gamma \int_\Omega (a - 1) \delta a \, dx. \qquad (2.3.6)$$

It is left to compute $a_a(u'_a, \lambda)$. Taking the variation on both sides of (2.3.2) we obtain

$$\frac{d}{d\tau} a_{a+\tau\delta a}(u(a + \tau \delta a), v) \Big|_{\tau=0} = a'_{\delta a}(u, v) + a_a(u'_a, v) = l'_{\delta a}(v).$$

Thus,

$$a_a(u'_a, \lambda) = l'_{\delta a}(\lambda) - a'_{\delta a}(u, \lambda),$$

and it is left to compute the derivatives of the bilinear form $a(u, v)$ and the right-hand side $l(v)$ with respect to the design:

$$
\begin{aligned}
a'_{\delta a}(u, v) &= \frac{d}{d\tau} a(u(a + \tau \delta a), v) \Big|_{\tau=0} \\
&= \frac{d}{d\tau} \Big[\int_\Omega \nabla u \cdot \nabla v \, dx + \int_\Omega s^2 (a + \tau \delta a) uv \, dx + \int_{\partial\Omega} suv \, d\sigma \Big] \Big|_{\tau=0} \\
&= \int_\Omega s^2 uv \, \delta a \, dx; \\
l'_{\delta a}(v) &= 0.
\end{aligned}
$$

Combining the last expressions and (2.3.6) yields (2.3.4). The proof is complete. $\qquad\square$

2.3.1 Shape derivatives

In Section 2.4, Paper III we compute the shape derivative of an integral functional written in terms of the eigenfunctions of the Laplace operator in a cylinder.

In this section, we give a short introduction to the material derivatives for shape design sensitivity problem (see Section 3.2 in [15]). The goal is to establish a relationship between the variation in shape and the variation in a given functional. The proofs of differentiability and regularity are quite technical and is not the purpose of our exposition. For rigorous mathematical proofs we refer to [15].

We will think about the domain Ω as a continuous medium, and introduce a parameter describing the evolution (transformation) of Ω. Namely, denote by T the mapping that for each $x \in \Omega$ gives a new point $x_\tau = T(x, \tau)$. One can think about the parameter τ as time, and at $\tau = 0$ we have the original domain Ω. The design velocity is defined by

$$V(x_\tau, \tau) = \frac{dx_\tau}{d\tau} = \frac{dT(x, \tau)}{d\tau} = \frac{\partial T(x, \tau)}{\partial \tau}, \tag{2.3.7}$$

where in the last equality we have used that the initial point x does not depend on τ. We assume also that the deformation can be reversed, that is one can come to the initial point by inverting the mapping $x = T^{-1}(x_\tau, \tau)$. We can now write down a differential equation describing the design trajectory:

$$\dot{x}_\tau = \frac{dx_\tau}{d\tau} = V(x_\tau, \tau), \quad x_0 = x.$$

For small times close to $\tau = 0$, we can linearize the transformation T:

$$T(x, \tau) = x + \tau V(x), \quad V(x) := V(x, 0). \tag{2.3.8}$$

The transformed domain is denoted by $\Omega_\tau = T(\Omega, \tau)$, and the boundary of Ω_τ is denoted by Γ_τ.

Since the design now is the shape of the domain, it is convenient to indicate the dependence on the domain in the weak formulation of the problem. Let $u_\tau(x_\tau)$ be a solution of the problem in the deformed domain Ω_τ:

$$a_{\Omega_\tau}(u_\tau, v_\tau) = l_{\Omega_\tau}(v_\tau), \quad v_\tau \in Z_\tau, \tag{2.3.9}$$

where $Z_\tau \subset H^1(\Omega_\tau)$ is the space of kinematically admissible displacements.

Definition 2.3.2. The material derivative $\dot{u}(x)$ at Ω, if it exists, is defined by

$$\lim_{\tau \to 0} \frac{u_\tau(x + \tau V(x)) - u(x)}{\tau} - \dot{u}(x) = 0.$$

In case of classical solutions, the limit is pointwise, while for weak solutions we take the limit in the Sobolev norm, since the pointwise derivatives do not need to exist in the latter case. It turns out that it facilitate the computations if we write the material derivative as the sum

$$\begin{aligned}
\dot{u}(x) &= \lim_{\tau \to 0} \frac{u_\tau(x + \tau V(x)) - u(x)}{\tau} \\
&= \lim_{\tau \to 0} \frac{u_\tau(x) - u(x)}{\tau} + \lim_{\tau \to 0} \frac{u_\tau(x + \tau V(x)) - u_\tau(x)}{\tau} \\
&= u'(x) + \nabla u \cdot V(x).
\end{aligned}$$

Thus, the material derivative is the sum of the partial derivative $u'(x)$ and the convective term $\nabla u \cdot V$:

$$\dot{u}(x) = u'(x) + \nabla u \cdot V(x). \tag{2.3.10}$$

The notation $u'(x)$ should not be confused with the partial derivatives with respect to x_i, $i = 1, \ldots, d$. The limits are understood in pointwise sense for classical solutions $u(x)$ and in the Sobolev norm for weak solutions.

For our purposes, we need to obtain the expression for the material derivatives of bilinear forms and linear integral functionals. Making the change of variables under the integral so that the integration domain becomes Ω, one can prove the following lemma for the material derivative of an integral functional.

Lemma 2.3.3 (Lemma 3.2.1 [15]). *Consider $\psi_1 = \int_{\Omega_\tau} G_\tau(x_\tau) dx_\tau$, where G_τ is a function defined on Ω_τ. The material derivative of ψ_1 at Ω is*

$$\psi_1' = \int_\Omega G'(x)\, dx + \int_\Gamma G(x)(V \cdot \nu)\, d\sigma.$$

Here $G'(x)$ is the partial derivative of f with respect to τ (not to be confused with partial derivatives in x_i, $i = 1, \ldots, d$).

Note that it is only the normal component of the velocity $V \cdot \nu$ that contributes to the material derivative, which is intuitively clear since the tangential component of the velocity does not deform the domain Ω.

Now we turn to the derivation of the weak formulations (bilinear forms and linear functionals) with respect to the shape. Below, we present the formal computations, which are justified by the differentiability results in [15], Section 3.5.4. Consider the weak formulation in the form

$$a_{\Omega_\tau}(u_\tau, v_\tau) = \int_\Omega c(u_\tau, v_\tau)\, dx_\tau = \int_{\Omega_\tau} f v_\tau\, dx_\tau = l_{\Omega_\tau}(v_\tau), \quad v_\tau \in Z_\tau, \tag{2.3.11}$$

where $Z_\tau \subset H^1(\Omega_\tau)$ is the space of kinematically admissible displacements, $c(\cdot, \cdot)$ is a bilinear mapping, and $u_\tau = 0$ on Γ_τ. The proof of the following statement can be found in [15].

Lemma 2.3.4. *The material derivative $\dot{u}(x)$ at Ω solves the sensitivity equation*

$$a_{\Omega_\tau}(\dot{u}, v) = \int_\Omega \left(c(u, \nabla v \cdot V) + c(\nabla u \cdot V, v) - f(\nabla v \cdot V) \right) dx$$

$$+ \int_\Gamma (fv - c(u, v))(V \cdot \nu)\, d\sigma, \quad v \in Z,$$

and is such that $\dot{u} = 0$ on Γ. Here Z is the corresponding functional space.

It should be emphasized that the last result provides $\dot{u}$ as a solution to a problem with the same bilinear form, as for u, but with a different right-hand side. The latter is known as soon as we solve (2.3.11) for $\tau = 0$ (in the initial domain Ω) and take a given velocity vector V.

To give an example, let us study a problem which is closely related to one in Paper III, the eigenvalue shape design sensitivity problem. It is clear that the natural frequencies and modes depend on the shape of the structure. We follow the ideas in Section 3.4 [15] and differentiate a simple eigenvalue with respect to the shape of the domain. To fix the ideas, let us consider the first eigenvalue ζ of the Dirichlet Laplacian. In the deformed domain Ω_τ, the eigenvalue problem in weak form is

$$a_{\Omega_\tau}(u_\tau, v_\tau) = \int_{\Omega_\tau} \nabla u_\tau \cdot \nabla v_\tau \, dx_\tau = \zeta_\tau \int_{\Omega_\tau} u_\tau v_\tau \, dx_\tau = \zeta_\tau b_{\Omega_\tau}(u_\tau, v_\tau), \quad \forall v_\tau \in H_0^1(\Omega_\tau).$$
(2.3.12)

We normalize the eigenfunctions by

$$\|u_\tau\|_{L^2(\Omega_\tau)} = 1.$$

It is proved in [15], Section 3.5.5 that the first eigenvalue (which is simple) is differentiable. We take the material derivative on both sides of (2.3.12):

$$(a_\Omega(u, v))' = \zeta' b_\Omega(u, v) + \zeta (b_\Omega(u, v))'.$$
(2.3.13)

Our goal is to derive an explicit expression for ζ' in terms of the first eigenpair (ζ, u) in the undeformed domain Ω and the velocity $V(x)$.

Lemma 2.3.5. *The material derivative of the first eigenvalue ζ of the Dirichlet Laplacian in the direction of V is given by*

$$\zeta' = -\int_\Gamma |\nabla u \cdot \nu|^2 (V \cdot \nu) \, d\sigma.$$

where u is the first eigenfunction corresponding to the eigenvalue ζ, and ν is the external unit normal vector to Γ.

Proof. Using (2.3.10) we get:

$$(a_\Omega(u, v))' = \int_\Omega (\nabla u' \cdot \nabla v + \nabla u \cdot \nabla v') \, dx + \int_\Gamma \nabla u \cdot \nabla v (V \cdot \nu) \, d\sigma$$
$$= \int_\Omega (\nabla(\dot{u} - \nabla u \cdot V) \cdot \nabla v + \nabla u \cdot \nabla(\dot{v} - \nabla v \cdot V)) \, dx + \int_\Gamma \nabla u \cdot \nabla v (V \cdot \nu) \, d\sigma.$$

Since v_τ is an arbitrary element of $H_0^1(\Omega_\tau)$, the material derivative can be assumed to be zero $\dot{v} = 0$, and we get

$$(a_\Omega(u, v))' = \int_\Omega (\nabla(\dot{u} - \nabla u \cdot V) \cdot \nabla v - \nabla u \cdot \nabla(\nabla v \cdot V)) \, dx + \int_\Gamma \nabla u \cdot \nabla v (V \cdot \nu) \, d\sigma$$
$$= \int_\Omega (\nabla(\dot{u} - \nabla u \cdot V) \cdot \nabla v - \nabla u \cdot \nabla(\nabla v \cdot V)) \, dx + \int_\Omega \operatorname{div}((\nabla u \cdot \nabla v)V) \, dx.$$

In the last equality we have integrated by parts to transform the boundary integral into the volume integral. Similarly, using the boundary condition $u\big|_\Gamma = 0$, we have

$$(b_\Omega(u,v))' = \int_\Omega ((\dot{u} - \nabla u \cdot V)v - u(\nabla v \cdot V))\, dx + \int_\Gamma u\, v\, (V \cdot \nu)\, d\sigma$$

$$= \int_\Omega ((\dot{u} - \nabla u \cdot V)v - u(\nabla v \cdot V))\, dx.$$

Next, we take u as a test function in (2.3.13) and using the normalization condition $b_\Omega(u,u) = 1$, we obtain

$$\zeta' = (a_\Omega(u,u))' - \zeta(b_\Omega(u,u))'. \tag{2.3.14}$$

Since $\dot{u}$ can be taken as a test function in (2.3.12), and u is the solution of (2.3.12), then

$$a_\Omega(u, \dot{u}) = \zeta\, b_\Omega(u, \dot{u}),$$

and the material derivatives of the bilinear form $(a_\Omega(u,u))'$ and $(b_\Omega(u,u))'$ reduce to

$$(a_\Omega(u,u))' = -2\int_\Omega \nabla(\nabla u \cdot V) \cdot \nabla u\, dx + \int_\Omega \operatorname{div}\big(|\nabla u|^2 V\big)\, dx;$$

$$(b_\Omega(u,v))' = -2\int_\Omega (\nabla u \cdot V)u\, dx.$$

The last two equalities combined with (2.3.14) yield

$$\zeta' = 2\int_\Omega \big[-\nabla u \cdot \nabla(\nabla u \cdot V) + \zeta u(\nabla u \cdot V)\big]\, dx + \int_\Omega \operatorname{div}\big(|\nabla u|^2 V\big)\, dx$$

$$= 2\int_\Omega \big[-\nabla u \cdot \nabla(\nabla u \cdot V) + \zeta u(\nabla u \cdot V)\big]\, dx + \int_\Gamma |\nabla u|^2(V \cdot \nu)\, d\sigma,$$

Now we integrate by parts one more time and use again the fact that (ζ, u) solves (2.3.12):

$$\zeta' = -2\int_\Gamma (\nabla u \cdot \nu)(\nabla u \cdot V)\, d\sigma + \int_\Gamma |\nabla u|^2(V \cdot \nu).$$

Since $u = 0$ on Γ, the tangential component of u is also equal to zero on Γ, and $\nabla u = (\nabla u \cdot \nu)\nu$. Thus, $(\nabla u \cdot \nu)(\nabla u \cdot V) = |\nabla u \cdot \nu|^2(V \cdot \nu)$, and the final expression for the material derivative of the first eigenvalue is

$$\zeta' = -\int_\Gamma |\nabla u \cdot \nu|^2(V \cdot \nu)\, d\sigma.$$

$\square$

The methods in this section are used in Paper III to compute the material derivative of the average sound pressure level in cylindrical domains.

2.4   Machine Learning

Paper III presents a machine learning approach for computing the average sound pressure under the harmonic load over some frequency range. We generate the test data by numerically computing the eigenmodes of the Laplace operator in polygonal domains. For machine learning we have used Tensorflow [16], and the stochastic gradient descent optimizer ADAM [17].

In this section, we briefly describe the ideology of machine learning and the stochastic gradient descent algorithm. For a rigorous description of the the deep neural networks construction we refer to [18] and [19].

The main goal of the machine learning algorithms is to construct a function (black box), performing well on the test data, to make predictions concerning the unseen data. For example, in the case of the recognition of hand-written digits, an input to this learning function is a matrix of pixels and the desired output is a digit. Machine learning tackles many different kind of tasks. Among them are classification problems (as object recognition), regression (given an input, predict the value of the output), transcription (optical character recognition), and machine translation. To evaluate the machine learning performance, we need to specify a performance measure. In many cases we are interested in the performance on the unseen data, so the algorithms are evaluated on the test data separated from the training data.

It is interesting to note that the success of machine learning algorithms is supported not only empirically but also theoretically. It was shown that for a given continuous function $f(v)$ with the input vector v in a cube in $\mathbf{R}^d$, there exists a net approximating it with any desired accuracy [20]. In [21] it has been proved that feedforward networks with as few as a single hidden layer and an appropriately smooth hidden layer activation function can approximate an arbitrary function and its derivatives with desired accuracy. Moreover, it is possible to approximate functions which are only weakly differentiable. In fact, a priori it is not obvious that there exists a set of weights that provides an approximation to both the function itself and its derivatives. It is proved in [21] that such a set of weights does indeed exist.

In our case in Paper III, the input to the neural network is the coordinates of five points defining the cylindrical domain, and the output is a scalar Ψ_{ml} giving the average pressure level in the given domain. Since the output is a real number, we have a regression type of problem. Having generated a data set containing values of the average pressure level Ψ for N polygonal cylinders, we train a learning function on a part of this set (minibatch). Assigning weights to the inputs, we create a function so that the mean-mean-square error in the approximation of Ψ is minimized. Then we evaluate the performance of our function Ψ_{ml} by applying it to the unseen data and measure the accuracy of the predicted average pressures.

The simplest learning function is affine $\Psi_{\mathrm{ml}} = Ax + b$ (x is the vector of inputs). In this case the entries of the matrix A are the weights to be learned, and b is called a bias vector. But it is usually too simple to give a good result. For example, if one tries to recognize Roman numbers, then II might be something between I and III [18].

The learning function has the form of a composition

$$\Psi_{\mathrm{ml}}(v) = L_M(R(L_{M-1}(R \cdots (L_1 v)))),$$

where $L_k v = A_k v + b_k$ are affine functions, and R is a nonlinear function, the activation function. The weights to be learned to get a reasonable approximation are the entries in A_k and b_k. In this way the output is a recursively nested composition function of inputs: input to the first hidden layer, input from the first to the second hidden layer, ..., input from the last $(M-1)$:th hidden layer to output layer. An schematic illustration of a deep neural network is given in Figure III.4.1 in Paper III, where each diagonal represents a weight. Each hidden layer in Figure III.4.1 contains both the linear L_k and the nonlinear activation function R. In a typical situation, more hidden layers will give a higher accuracy. In order to have a high accuracy on unseen data, one needs to stop the minimization process before one overfits. Typically, if the learning function performs poorly on the training set, one underfit, while if it does well on the training set and poorly on the test set, one overfit. In other words, when we overfit, we create a learning function that does not generalize (from the training set to the test set).

There are many options for the nonlinear function R. A widely used choice of nonlinearity is a so-called "sigmoidal" functions (having S-shaped graph). A smooth sigmoidal function like $\tanh x/2 = (e^x - 1)/(e^x + 1)$ has been a popular choice, but after that numerous numerical experiments indicated that this might not be an optimal. In many examples, it has turned out that a piecewise linear function $\mathrm{ReLU}(x) = \max\{0, x\}$ (the positive part x^+ of the linear function x, sometimes called a rectified linear unit) performs better [18].

The goal of the learning is to choose the weights to minimize the error over training sample, such that it generalize well to unseen data. This is a large-scale optimization problem, and the choice of the algorithm is crucial for the result.

By construction of the learning function, the input to RL_1 is v coming from the training set, the input to RL_{k+1} is $v_k = R(L_k v_{k-1})$. On each layer, this gives $v_k = R(A_k v_{k-1} + b_k)$, a vector of length N_k, where the weights are obtained by the optimization algorithm. Thus, the matrix A_k is $N_k \times N_{k-1}$, and the vector b_k has N_k components. The final composition in the case of ReLU nonlinearity is piesewise affine with respect to the input vector v. This creates a fully connected neural network.

Since the training phase of the machine learning assumes the penalization of the difference between the predicted and observed values of dependent variables, it obviously requires the use of optimization techniques. Most of the optimization problems are minimization problems, and the classical idea of the gradient descent method is a natural choice.

A key ingredient in the training of a deep neural network is the stochastic gradient descent (SGD) [22] allowing to minimize the loss function $L(x)$ for the test data. This is a method converging to the optimum in probability.

Recalling the classical gradient descent, in order to minimize a function $f(x)$, one needs to move in the direction opposite to its gradient, i.e. $-\nabla f(x)$, to approach

the minimum:

$$x_{k+1} = x_k - s_k \nabla f(x_k), \quad k = 1, 2, \dots.$$

Here s_k is called the stepsize of the learning rate.

The classical gradient descent becomes too expensive on large data sets. SGD does not use the whole test set, but only a part of it called mini-batch on each step, which essentially reduces the computational cost.

Among the parameters, the learning rate is probably one of the most difficult to choose. At the same time, since the choice of the learning rate affects the model performance, it is important to adapt it during the training. Among the mini batch-based methods, ADAM is one of the methods that adapt the learning rates of model parameters. ADAM was introduced by Kingma and Ba in [17]. The name comes from "adaptive moments".

The method of momentum aims to accelerate learning, in particular when the gradients have noisy component, or they are small with high curvature. The algorithm of momentum introduces a variable $\mathbf{v}$. This variable gives the direction and speed at which the parameters move through parameter space. This is the reason why $\mathbf{v}$ is called velocity.

Stochastic gradient descent with momentum requires learning rate ϵ and momentum parameter α. The update of the parameters $\boldsymbol{\theta}$ of a neural network is as follows $\boldsymbol{\theta} \leftarrow \boldsymbol{\theta} + \mathbf{v}$. In turn, the velocity $\mathbf{v}$ is updated by momentum parameter α. Moreover, $\mathbf{v}$ accumulates the elements of the gradient of the loss with respect to the parameters for that minibatch $\mathbf{g}$ given by

$$\mathbf{g} = \frac{1}{m} \nabla_{\boldsymbol{\theta}} \sum_i L(f(\mathbf{x}^{(i)}; \boldsymbol{\theta}), \mathbf{y}^{(i)}). \tag{2.4.1}$$

where a minibatch of m examples from the training set $\{\mathbf{x}^{(1)}, ..., \mathbf{x}^{(m)}\}$ with corresponding targets $\mathbf{y}^{(i)}$. The update of velocity $\mathbf{v}$ is carried out as follows

$$\mathbf{v} \leftarrow \alpha \mathbf{v} - \epsilon \mathbf{g}. \tag{2.4.2}$$

Formula (2.4.2) allows to treat the momentum algorithm as accumulation an exponentially decaying average of previous gradients and moving in their direction.

The idea behind the ADAM algorithm is as follows: to apply the method of momentum to the rescaled gradients. On practice it means that the algorithm includes both updates and correction of moments corresponding to gradient and squared one. The Adam algorithm requires step size ϵ, exponential decay rates for moment estimates ρ_1 and ρ_2, and small constant δ served for numerical stabilization [23]. The parameters $\boldsymbol{\theta}$, 1st and 2nd moment variables $\mathbf{s}$ and $\mathbf{r}$, and time step t must be initialized. During adaptive learning rate optimization, i.e. the following update: $\boldsymbol{\theta} \leftarrow \boldsymbol{\theta} + \Delta\boldsymbol{\theta}$, the next scheme is realized [23]

- sample a minibatch of m examples from the training set $\{\mathbf{x}^{(1)}, ..., \mathbf{x}^{(m)}\}$ with corresponding targets $\mathbf{y}^{(i)}$,

- compute the gradient $\mathbf{g}$ by (2.4.1) and update time step t,

- update $\mathbf{s}$ and $\mathbf{r}$ moments: $\mathbf{s} \leftarrow \rho_1 \mathbf{s} + (1 - \rho_1)\mathbf{g}$, $\mathbf{r} \leftarrow \rho_2 \mathbf{r} + (1 - \rho_2)\mathbf{g} \odot \mathbf{g}$ with element-wise (Hadamard) product denoted as $\odot$,

- correct bias in both moments: $\hat{\mathbf{s}} \leftarrow \frac{\mathbf{s}}{1 - \rho_1^t}$, $\hat{\mathbf{r}} \leftarrow \frac{\mathbf{r}}{1 - \rho_2^t}$,

- compute $\Delta\boldsymbol{\theta}$: $\Delta\boldsymbol{\theta} = -\epsilon \frac{\hat{\mathbf{s}}}{\sqrt{\hat{\mathbf{r}} + \delta}}$.

ADAM is usually considered as being pretty robust to the choice of hyperparameters. It should be noted, however, that sometimes there is a need to change the learning rate from the proposed default.

References

[1] ISO Central Secretary. *ISO 10140–2:2021, Acoustics — Laboratory measurement of sound insulation of building elements — Part 2: Measurement of airborne sound insulation*. en. Standard ISO 10140-2:2021. Geneva, C. H.: International Organization for Standardization, 2021. URL: `https://www.iso.org/standard/79487.html`.

[2] ASTM E90-09. *Standard Test Method for Laboratory Measurement of Airborne Sound Transmission Loss of Building Partitions and Elements*. West Conshohocken, Pa.: ASTM, 2016. URL: `www.astm.org`.

[3] ISO Central Secretary. *ISO 15186–1:2000, Acoustics – Measurement of Sound Insulation in Buildings and of Building Elements Using Sound Intensity – Part 1: Laboratory Measurements*. en. Standard ISO 15186-1:2000. Geneva, C. H.: International Organization for Standardization, 2000. URL: `https://www.iso.org/standard/26097.html`.

[4] ASTM E2249-02. *Standard Test Method for Laboratory Measurement of Airborne Sound Transmission Loss of Building Partitions and Elements Using Sound Intensity*. West Conshohocken, Pa.: ASTM, 2016. URL: `www.astm.org`.

[5] ISO Central Secretary. *Acoustics – Measurement of sound absorption in a reverberation room*. en. Standard ISO 354:2003. Geneva, C. H.: International Organization for Standardization, 2003.

[6] ISO Central Secretary. *Acoustics – Determination of sound absorption coefficient and impedance in impedance tubes – Part 2: Transfer-function method*. en. Standard ISO 10534-2:1998. Geneva, C. H.: International Organization for Standardization, 1998. URL: `https://www.iso.org/standard/22851.html`.

[7] *Transmission loss tube and impedance tube kit, type 4206*. `https://www.bksv.com/en/products/transducers/acoustic/Acoustic-material-testing-kits/transmission-loss-and-impedance-tube-kits-4206`. Accessed: 2023-04-21.

[8] A. Nilsson and B. Liu. *Vibro-Acoustics, Volume 2*. Springer Berlin Heidelberg, Jan. 2016, pp. 1–452. ISBN: 978-3-662-47933-9. DOI: `10.1007/978-3-662-47934-6`.

[9]   N. Atalla and F. Sgard. "Modeling of perforated plates and screens using rigid frame porous models". In: *Journal of Sound and Vibration* 303 (June 2007), pp. 195–208. DOI: `10.1016/j.jsv.2007.01.012`.

[10] Lawrence C Evans. *Partial differential equations*. Vol. 19. American Mathematical Society, 2022.

[11] H. Brezis. *Functional analysis, Sobolev spaces and partial differential equations*. Vol. 2. 3. Springer, 2011.

[12] G. Allaire. *Numerical analysis and optimization: an introduction to mathematical modelling and numerical simulation*. Oxford university press, 2007.

[13] W Rudin. *Functional analysis*. McGraw-Hill, New York, 1973.

[14] M. Struwe. *Variational methods*. Vol. 34. Springer, 2000.

[15] V. Komkov, K. K. Choi, and E. J. Haug. *Design sensitivity analysis of structural systems*. Vol. 177. Academic press, 1986.

[16] M. Abadi et al. *TensorFlow: Large-Scale Machine Learning on Heterogeneous Systems*. Software available from tensorflow.org. 2015. URL: `https://www.tensorflow.org`.

[17] D. P. Kingma and J. Ba. "Adam: A method for stochastic optimization". In: *arXiv preprint arXiv:1412.6980* (2014).

[18] G. Strang. *Linear algebra and learning from data*. Wellesley-Cambridge Press, 2019.

[19] G. Montavon, G. Orr, and K.-R. Müller. *Neural networks: tricks of the trade*. Vol. 7700. springer, 2012.

[20] G. Cybenko. "Approximation by superpositions of a sigmoidal function". In: *Mathematics of control, signals and systems* 2.4 (1989), pp. 303–314.

[21] K. Hornik, M. Stinchcombe, and H. White. "Universal approximation of an unknown mapping and its derivatives using multilayer feedforward networks". In: *Neural networks* 3.5 (1990), pp. 551–560.

[22] H. Robbins and S. Monro. "A stochastic approximation method". In: *The annals of mathematical statistics* (1951), pp. 400–407.

[23] I. Goodfellow, Y. Bengio, and A. Courville. *Deep Learning (Adaptive Computation and Machine Learning Series)*. 2016.

PAPER I

Insertion loss of macro-perforated plates with viscoelastic filling[1]

Andrei Karzhou[2]

UiT The Arctic University of Norway

Irina Pettersson

Chalmers University of Technology and Gothenburg University, Sweden

Klas Pettersson

UiT The Arctic University of Norway

Abstract

An experimental comparative study of sound insertion loss for macro-perforated plates filled with viscoelastic material is presented. The effect of viscosity is captured in cases of filling exposed to the acoustic field, and for isolated inclusions in a layered material setup. Steel and high density polyethylene are considered as plate materials, and polyurethane and an emulsified oil lubricant as filling materials. It is observed that the plates with exposed fillings show sound insertion loss levels similar to solid plates, and in line with the mass law within the frequency range 200–3150 Hz. The layered plates, with filling as inclusions, show sound insertion loss levels substantially lower than solid plates of the same mass for the mid-range 300–2000 Hz range, and higher for low frequencies.

Keywords: Sound insertion loss, macro-perforated plates, layered material, viscoelastic filling, pseudoplastic fluid inclusions.

I.1   Introduction

The design of soundproofing and sound absorbing materials attracts attention of both engineers and physicists. Structure and properties of such materials depend strongly on the frequency range and the area of applications. The use of perforation in acoustic panels is justified by the energy absorption due to the friction between the walls of the pores and the fluid, such as air or liquid. One can achieve a good damping of high frequencies using materials with very fine microstructure, such as porous materials [1]. One of the most appropriate descriptors of the acoustical characteristics of a structure is the sound insertion loss (IL). Since the IL is defined in terms of the sound pressure level, it does not require the knowledge of the source strength, and is often used for comparison of sound insulation properties of different materials and structures.

There are numerous works devoted to the study of acoustical characteristics of perforated screens. Depending on the size of the perforation, one distinguishes micro- and macro-perforated screens. In the present work we study the latter ones.

Classical models for absorption and transmission coefficients for perforated screens and porous materials with perforated facings, have been developed in [1, 2] (see also the references therein). Modelling the porous media as an equivalent fluid, acoustic characteristics are then written in terms of the effective density, bulk modulus, and acoustic impedance. In [3], perforated plates coupled with free air, air gap, or porous layer, are modelled as equivalent fluids in the context of the transfer matrix method. It is shown that the effect of the viscosity dominates over the thermal effects in the absorption of sound energy for macro-perforated plates, with radius of perforations between 1 mm and 1 cm, with a viscous filling. By increasing the total area between matrix material of the plate and viscoelastic one it is expected that the sound energy of incoming waves will be reduced.

A method for calculating the sound transmission loss of a perforated screen at frequencies below 4 kHz is presented in [4]. The authors use a two-dimensional plane wave theory, and compare the theoretical model with laboratory measurements for different materials, thicknesses and percentages of perforation.

In [5] the results of theoretical, numerical and experimental studies of multilayer partitions made up of macro- or micro- perforated rigid panels in linear regime are presented. The authors develop enhanced modal matching theory of the acoustic absorption, transmission and dissipation for unbacked multi-layer macro-perforated panels under oblique incidence of sound waves.

In [6], the authors consider macro-perforated samples with different pore sizes and porosities in the microporous medium. For the 3D printed samples, the measurements of sound absorption coefficient have been done in a impedance tube for both non-perforated and macro-perforated sample sets. An improved absorption performance is observed for the macro-perforated samples. One of the important conclusions of the work is that the application of the additive manufacturing allows to achieve a good sound absorption performance which ultimately avoids the using of complex microstructures.

The work [7] concerns the study of sound absorption of specific acoustics resonators and considers perforated panels with oblique perforations backed by an air

cavity. It turns out that such geometry of the resonator leads to the increase the effective thickness of the panel, severely improving the low-frequency performance of the sound absorber.

To achieve a higher damping, a viscoelastic material might be added to the open pores. The viscous absorption of sound energy is used in buildings acoustics. For example, by adding a layer of viscoelastic material to the sheet one can increase the damping of bending waves [8].

There are many studies investigating a possibility to increase the sound absorption by adding isolated masses in the poroelastic material. For example, [9] describes the effect of circular periodic inclusions on the sound absorption. In particular, this theoretical study shows that a structure with inclusions can possess a quasi-total absorption peak below the quarter-wavelength resonance frequency. It should be noted that the absorption increases at some frequencies but also reduce sound absorption at the rest of frequencies significantly as the size of inclusion increases. We observe this effect in the present study, when an inner layer with visco-elastic inclusions is added between two solid plates (see Section I.4.2).

The influence of the inclusion shape on the absorption properties of the porous material have been investigated in [10]. In this numerical study, it has been found that specific configurations might improve the broadband sound absorption compared with reference material with no inclusion.

An experimental study of the IL for a poroelastic material with randomly placed inclusions is performed in [11]. The mass inclusions act as resonant systems, and so increase the structure impedance, that leads to the increase in the IL. It should be noted that the authors observe some reduction in the IL at higher frequencies, but it is much less than the increases in the targeted bandwidth.

Solid–liquid composites have been extensively studied for the last decades, and there are now numerous examples where such structures show unexpected novel properties [12]. There is a great variation in form and dimension of the liquid inclusions, depending on the specific applications, including droplets, liquid networks, and isolated liquid inclusions. Solid-liquid composites find their applications in soft robotics, soft electronics, as well in chemical and biological systems. A review of solid-liquid composites, their morphology, fabrication methods, and applications are presented in [12]. In the present work we investigate the effect of incorporating a pseudoplastic fluid (grease) into a perforated plate and a layered structure on their acoustic properties. Note that filling the perforation creates isolated inclusions, in contrast with the classical case of fluid-saturated porous media, where both the matrix and the fluid components are connected [13].

There are several standards of measuring sound insulation, for example ASTME [14] and ISO [15, 16], as well as there are restrictions for sample dimensions according to the standardized methods. The ISO 354:2003 standard specifies a method of measuring the sound absorption coefficient of acoustical materials used in room acoustics [16], and requires the test specimen area between 10 and 12 m^2. Technological solutions also exist, such as the Brüel & Kjær Impedance Tube Kit type 4206 which allows to measure samples which are 29 and 100 mm in diameter [17] in the frequency range 50 Hz to 6.4 kHz. The Acoustic test cabin [18] developed by Mecanum offers a possibility to measure transmission loss and sound absorption

in the diffuse-field condition. According to Mecanum's technical data sheet [19], the cabin is suitable for test samples between 0.36 m² and 1.3 m². The exterior dimensions of the test cabin are $2.6 \times 1.6 \times 2.0$ m³, and the weight is 1200 kg.

In building acoustics there are two commonly used methods to measure the panels' transmission loss. Both methods are provided in connected reverberant-anechoic rooms. The first technique requires pressure-pressure calculations based on the measurements of reverberation time in receiving room and average sound pressure level in both anechoic and reverberant rooms [20, 21]. The second technique represents a pressure-intensity calculations rely on measurement of the sound pressure level in reverberant room with sound source and a measurement of sound intensity in a receiving anechoic room [22, 23]. There is still ongoing work to develop new approaches for sound transmission loss measurements. In [24] the authors present new approach for transmission loss estimation of panels in coupled reverberant-anechoic rooms. The idea is to use two succeeding each other sound intensity measurements which ultimately leads to a new intensity-intensity approach. The sound intensity measurements are made before and after a test sample is mounted between the anechoic and reverberant rooms.

The present work is motivated by the challenge to create composite sound-proof panels using perforated plates filled with some viscoelastic material. We present a comparative experimental study of the IL in the range 200–3150 Hz for macro-perforated plates with the perforation filled with polyurethane and grease for thoughout perforation as well as isolated filled inclusions in layered structures. We show that the IL for the throughout perforated plates with filling follows the mass law, and is close to the IL for solid plates. The IL of the layered structures with inclusions show, however, a different behaviour. Namely, the IL for these layered plates is substantially (up to 10 dB) lower than the IL for solid plates of approximately the same mass for middle frequencies 315–1600 Hz, while for the 250 Hz and 2000 Hz third octave bands the IL is about 10 dB greater than the one for the solid plates.

The rest of this paper is organized as follows. In Section I.2 we present the material properties and geometry of the studied samples. The experimental setup for small-scaled experiments is described in Section I.3. This bench installation has length of about 1.2 m and the internal diameter 0.26 m. The dimensions of the setup and the flexibility in the samples' dimension makes this setup attractive for those aiming to test samples of different thickness and dimensions greater than those used in impedance tubes, but at the same time smaller than those installations/test cabins used for room acoustics. The IL is measured for both plain and perforated plates of different thickness, with and without viscoelastic filling. The influence of the filling and the thickness of the plates on the IL is analyzed in Section I.4.1. In Section I.4.2 we consider layered plates with an inner layer containing viscoelastic inclusions. The IL for the latter is compared with the one for solid plates of approximately the same mass. Finally, in Section I.5 we compare our experimental results with classical theoretical models of the sound attenuation [25].

I.2 Samples

The studied samples are metal and plastic square plates of size 40×40 cm^2, and of various thicknesses. The plates are made from steel and from high density polyethylene. In what follows we will write ME for steel plates and PE for the polyethylene ones. The mass density and the linear isotropic elastic material parameters are given in Table I.1. The metal and plastic plates are perforated periodically with cylindri-

Table I.1: Material parameters.

Material	Young modulus E (GPa)	Poisson ratio ν	Density ρ_s (kg m^{-3})
Steel	200	0.3	7.86×10^3
Polyethylene	1	0.4	0.96×10^3

cal holes, and the size and position of the holes are chosen in such a way that the rigidity of the perforated samples is about 90% of the solid ones. Each perforated sample has 25×25 cells with dimensions $a \times a$, $a = 1.6$ cm, and a circular hole with radius $b = 0.3$ cm in each cell. The macro-porosity ϕ_p [2] is defined as the ratio between volume of all pores and the total volume of the plate, $\phi_p = \pi b^2/a^2 = 0.11$. A perforated plate is illustrated in Figure I.2.1a. The volume removed by perforation is then filled with a viscoelastic material, specifically polyurethane sealant (PU) [26], and a soap emulsified with oil grease lubricant (GR).

We perform the IL measurements for the following samples:

Set A: Perforated ME plates filled with PU, with thickness $d = 6$ and 10 mm.

Set B: Perforated PE plates filled with PU and GR, with thickness $d = 3, 6, 10$, and 20 mm.

Set C: Layered plates consisting of two solid PE plates with thickness $l = 3$ mm, and a perforated ME plate of thickness $d = 6$ and 10 mm, filled with GR placed in between the two solid ones.

Set D: Layered plates consisting of two solid PE plates with thickness $l = 3$ mm, and a perforated PE plate of thickness $d = 3, 10$, and 20 mm, filled with GR placed in between the two solid ones.

The layers in Set C, D are in contact, without air gap in between them, and not glued together. A periodicity cell for Sets A and B is illustrated in Figure I.2.1b (left), and for Sets C and D in Figure I.2.1b (right).

As a point of reference, we also consider solid plates:

Set E: Solid ME plates of thickness 6, 10 mm, and solid PE plates of thickness 3, 6, 10, and 20 mm.

The filled plates of Sets A–D will be referred to as ME-PU, PE-GR, ME-GR, and PE-GR, respectively, and the solid plates by ME and PE.
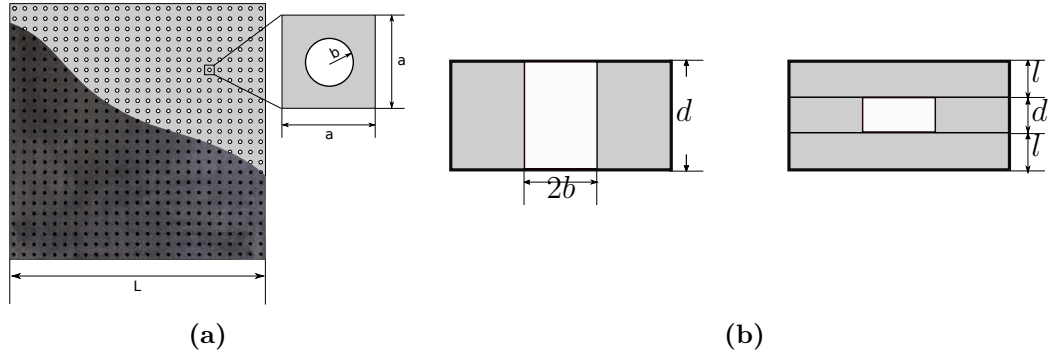
(a)   (b)

Figure I.2.1: Samples geometry: (a) Perforated plate with $L = 0.4$ m and radius of perforation $b = 0.3$ cm; Cross section of a periodicity cell for (b) perforated plates with filling (left) and layered plates with viscoelastic inclusions (right).

I.3   Experimental setup

The experimental setup is shown and illustrated in Figure I.3.1. After a signal is generated by Daqarta [27] (PC "1"), it passes through the power amplifier LV-103 "2", and is then reproduced by the loudspeaker "3". Sound waves from the loudspeaker are transmitted through the sample "4" and registered by the microphone "5". The signal from the microphone is registered by a MANOM-4 sound meter "6", and converted into the sound pressure levels without sample L^0 and with sample L^p. The measurements have been performed under normal ambient conditions.

We analyze the IL, that is the difference between sound pressure level L^0 measured without the plate sample, and the sound pressure level L^p when the sound passes through the sample.

$$\mathrm{IL} = L^0 - L^p. \tag{I.3.1}$$

The installation is a tube assembled from two acoustically isolated metal pipes with wall thickness 0.6 cm, internal diameter 26 cm, and length of the two parts 80 and 40 cm. A sample is placed between the two pipes and fixed by circular flanges with rubber gaskets using a lead screw. The short metal pipe can be moved by means of a worm-gear mechanism. This method of moving of the short pipe with the sound source allows to avoid centering, which, in its turn, makes the installation more convenient to use. In particular, it makes it possible to study structures made of materials with low values of hardness and brittleness.

To reduce the diffuse component of the sound field, the inner surfaces of both long and short tubes are covered with bitumen aluminum foil and, in addition, lined with a porous sound-absorbing material based on melamine foam.

The sound pressure level is given by a frequency sweep in the range 200–3150 Hz in steps of 10 Hz. Based on that, we compute the frequency sweep IL and the third octave band IL with geometric mean frequencies $200, 250, \ldots, 3150$ Hz. In Section I.4, the third octave band IL is presented for sample Sets A–E.

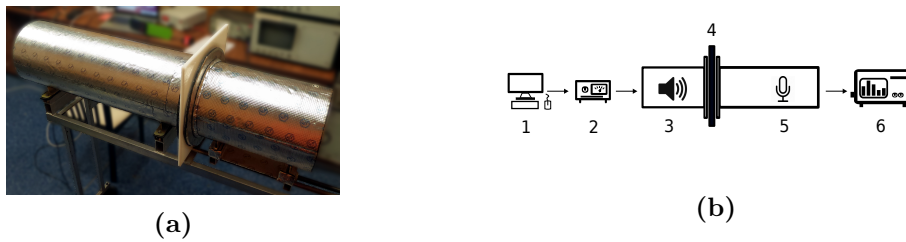**(a)**   **(b)**

Figure I.3.1: Experimental setup: (a) External view, and (b) schematic representation.

I.4 Experimental results

In Section I.4.1 we present the third octave IL for samples in Sets A and B, as described in Section I.2, that is perforated metal and plastic plates with PU and GR fillings. Section I.4.2 contains the measurement results for Sets C and D, that is layered metal and plastic plates with viscoelastic inclusions. We compare with these IL values with the ones for solid plates in Set E.

I.4.1 Macro-perforated plates with viscoelastic filling

For Sets A and B, we focus on analyzing the influence of the filling on the IL, for fixed thickness, as well as on comparing the plates of different thickness with the same filling.

Influence of filling for fixed thickness

Compared with the solid plates, for a fixed thickness, the filled perforated steel plates show in general slightly lower IL, as can be seen in Figure I.4.1, which is more pronounced in the case of 10 mm thick plates and reaches 10 dB at 315 Hz.

In Figure I.4.2 we compare plastic samples of the same thickness with different filling.

We observe, in particular, that there are several frequency ranges where the presence of PU and GR filling yields a higher IL than the IL for solid plates.

We look for third octave bands in which the filled polyethylene plates are showing greater IL than the solid plates, and in these selected regions we perform a linear sweep. The measured IL in the linear sweeps are shown in Figures I.4.3 and I.4.4. We observe that for 3 mm plates, the PU and GR filled plates both show greater IL than the solid plate in the regions 1200–1450 Hz, and in this interval the polyurethane filled plates show greatest IL, which is shown in Figure I.4.3a. For the 6 mm plate, in Figure I.4.3b and I.4.3c, we note that in the regions 400–550 Hz, the PU and GR filled plates show higher IL than the solid plate, and also here the PU filled plate shows the maximum IL, yet less distinct than in the case of 3 mm plates. In the same frequency range, the solid sample has the best sound insulation with the maximum of 35 dB at 630 Hz.

For the 10 mm filled polyethylene plates, in Figure I.4.4a, we observe that in the wide range 1100–1900, the IL of the PU filled plate is higher than the solid and higher or on par with the grease filled plate. As in the case of 6 mm thick metal

plates, one can see a well-marked drop at about 250 Hz. This can be explained by the coincidence of the sound signal frequency with eigenfrequency of the corresponding sample.

As shown in Figure I.4.4b and I.4.4c, the 20 mm filled polyethylene plates show greater IL than the solid plate in the ranges 400–700 Hz and 1400–1650 Hz. In particular, we observe an substantial peak in the IL of the PU filled plate close to 1500 Hz, as shown in Figure I.4.4c. Note that for low frequencies, the sample with GR filling yields the highest insertion loss of approximately 20 dB.
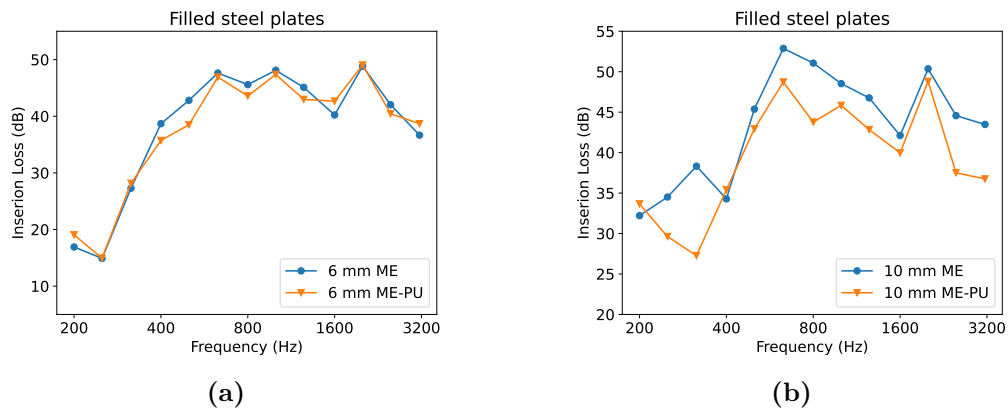

(a)   (b)

Figure I.4.1: Third octave band IL measurements for throughout perforated steel plates with polyurethane filling (Set A) and for solid plates of the same thickness (Set E) as reference: (a) 6 mm and (b) 10 mm.

Influence of plate thickness

In Figure I.4.5, the third octave IL for the PU-filled metal plates is presented. The 10 mm thick sample has substantially better sound insulation properties in the frequency range 200–315 Hz than the 6 mm sample. For frequencies in 400–3150 Hz interval the sound insulation of both samples varies between 38–48 dB.

The IL for plastic samples of different thicknesses with polyurethane filler are presented in Figure I.4.6a. For frequencies in the range 200–250 Hz, the 6 mm thick sample has the lowest sound insulation. The 3 mm thick sample has negative insertion loss near 315 Hz and a drop in third octave band. The 20 mm thick sample has the highest value of sound insulation in third octave band at about 1000 Hz.

The IL for samples of different thickness with GR filling are presented in Figure I.4.6b. Qualitative behaviour of the IL for these samples is similar to the one with PU filling. In 200–250 Hz frequency range the 3 mm thick sample introduces a greater IL than 6 and 10 mm samples. The 20 mm thick sample has the highest value of sound insulation in the whole studied range of frequencies except the region 1470–1520 Hz. In this region 10 mm thick sample is the most effective in the sense of sound insulation.
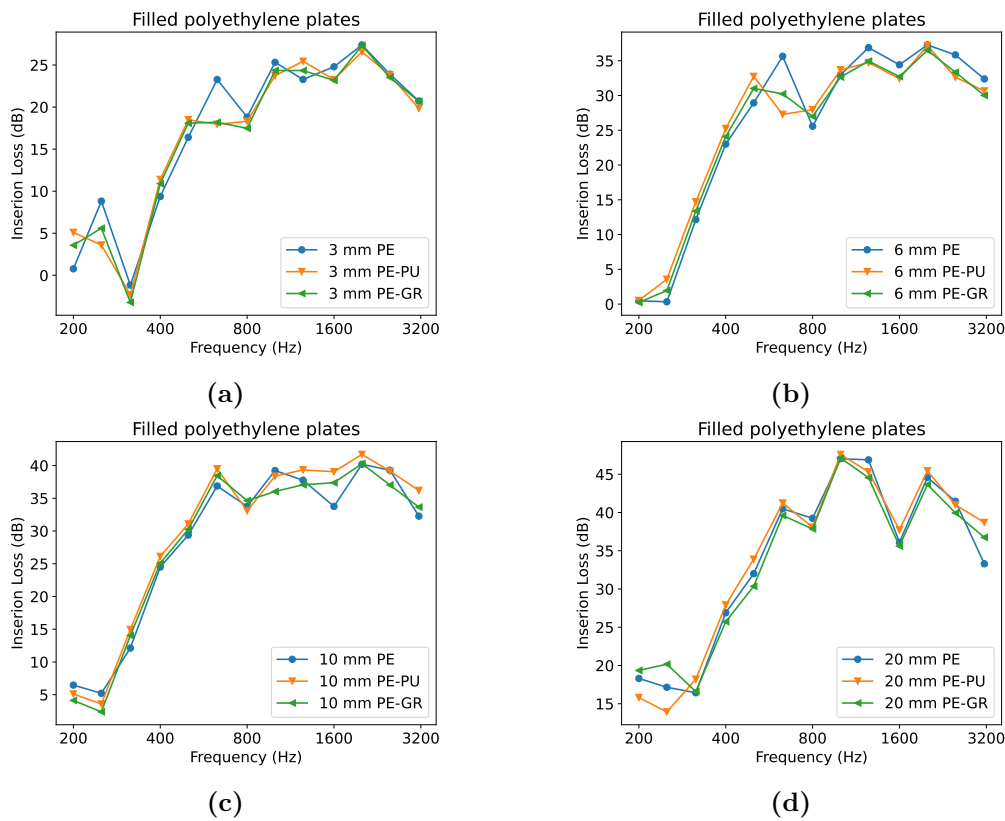
Figure I.4.2: Third octave band IL measurements for throughout perforated polyethylene plates with polyurethane (PU) and grease (GR) filling (Set B) and for solid polyethylene plates of the same thickness (Set E) as reference: (a) 3 mm, (b) 6 mm, (c) 10 mm, and (d) 20 mm.
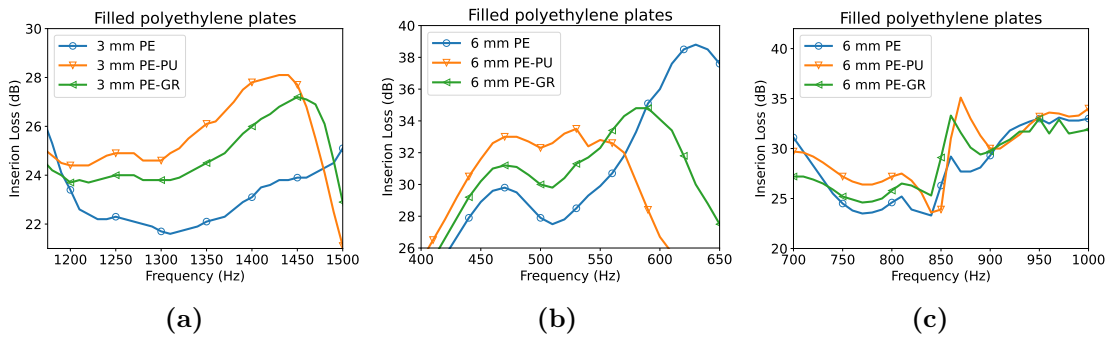
Figure I.4.3: Linear sweep of narrow ranges for Set B: (a) 3 mm, and (b)–(c) 6 mm filled polyethylene plates.

I.4.2 Layered macro-perforated plates with viscoelastic filling

The measured IL for layered metal and plastic plates with cylindrical grease inclusions are shown in Figure I.4.7. The mass of the layered metal plates of thickness 12 mm and 16 mm are 95% and 93% of the corresponding solid plates, respectively. As a point of reference, we use the solid metal plate of thickness 10 mm. We observe
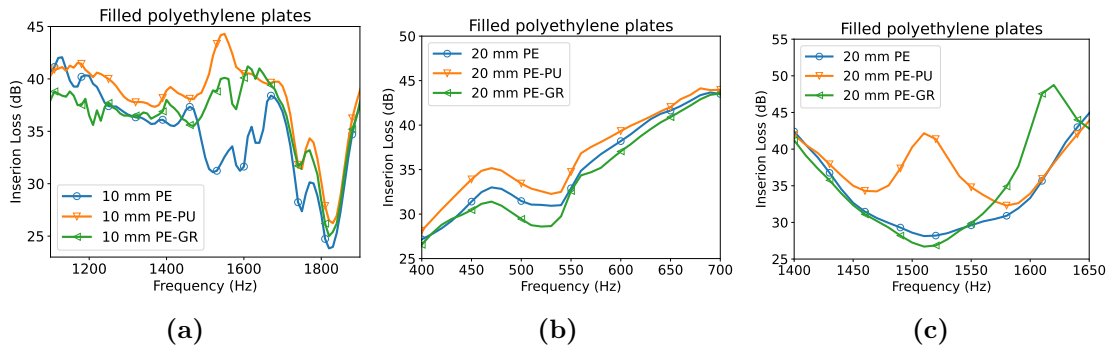
Figure I.4.4: Linear sweep of narrow ranges for Set B: (a) 10 mm, and (b)–(c) 20 mm filled polyethylene plates.
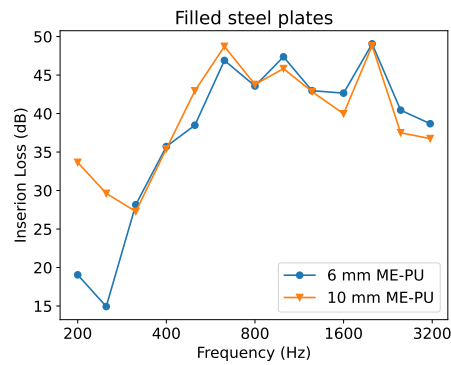
Figure I.4.5: Third octave band IL for Set A of filled steel plates.
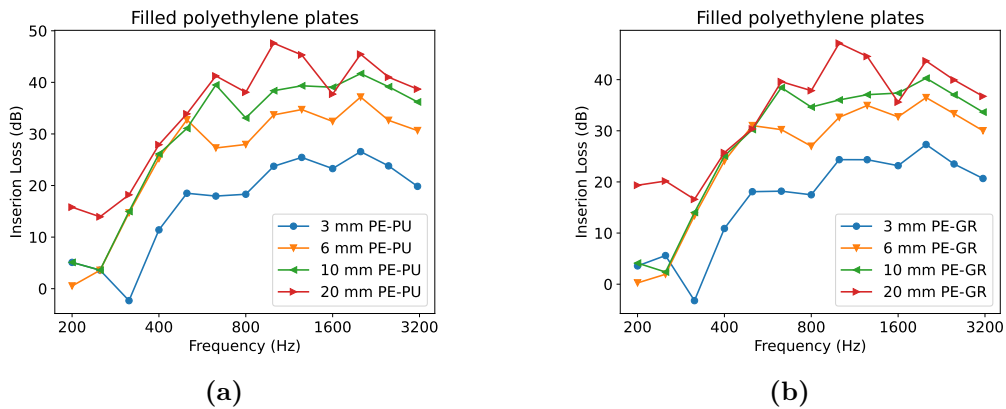
Figure I.4.6: Third octave band IL for filled polyethylene plates in Set B: (a) polyurethane and (b) grease.

that both the layered 12 mm and 16 mm plates show lower IL than the solid 10 mm plate. This corresponds to at least 6 dB of lower IL for the same mass for the metal plates.

The layered plastic plates show a similar deviation form the mass law. The layered plate of thickness 9 mm shows a significantly lower IL than the solid PE plate of thickness 10 mm, and we observe over 6 dB difference in IL for frequencies 630–3150 Hz, for essentially the same mass.

The layered 16 mm plastic plate with grease inclusions in the inner layer shows the IL close to the one of the solid 10 mm plate for frequencies 315–1600 Hz. However, below the 315 Hz third octave band and above the 1250 Hz third octave band, the layered 16 mm PE plate filled with grease, has in average about 10 dB lower IL than the 10 mm solid PE plate. The difference reaches almost 20 dB in the 2000 Hz third octave band.
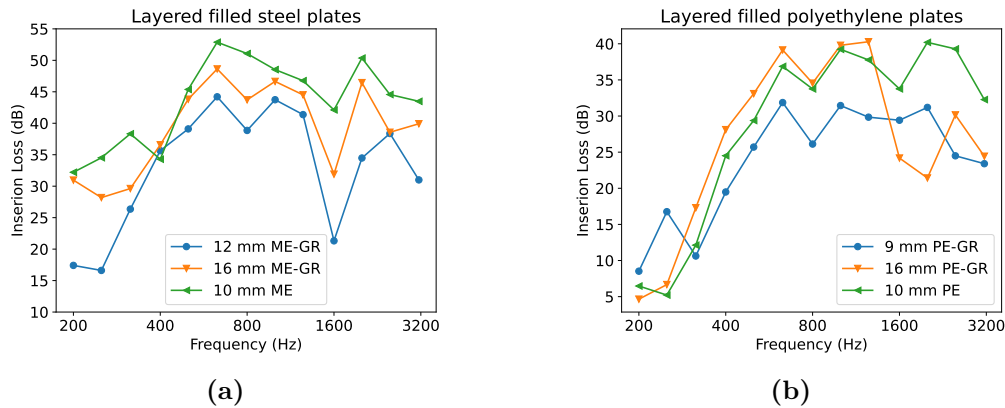
Figure I.4.7: Third octave band IL for plates in Sets C and D: (a) Layered composite plates with grease (GR) inclusions in the inner steel layer, and (b) layered plastic plates with GR inclusions in the inner layer.

I.5 Comparison with existing models

In this section we compare the measured IL with the theoretical one. For non-perforated plates one can use the corrected mass law [25].

The mass law states that a doubling of the mass of a plate yields approximately 6 dB reduction in the level of sound transmitted through it. Sound attenuation results from an interplay between mass, stiffness and damping. The mass law is affected by resonance at lower frequencies, and by coincidence for high frequencies. Namely, since coincidence between airborne and structure borne waves might occur in the frequency range of interest, and the mass law should be modified to include the change in transmission at the critical frequency and above [28, 25].

We consider the IL of the solid plates, and compare with the mass law in the frequency ranges where stiffness effects and radiation losses may be negligible. Denoting by f_c the critical frequency, the mass law assumes the scaling of an increase in transmission loss of about 6 dB when the mass per unit area of the plate is doubled. We get the following approximation to the IL for $f \ll f_c$, ignoring other absorbing effects,

$$\text{IL} = 20 \log_{10}(\mu f) - 48, \tag{I.5.1}$$

where μ denotes the plate mass density per unit area in $\text{kg}\,\text{m}^{-2}$, and f the frequency in Hz. For thin plates made from isotropic material, one considers the following

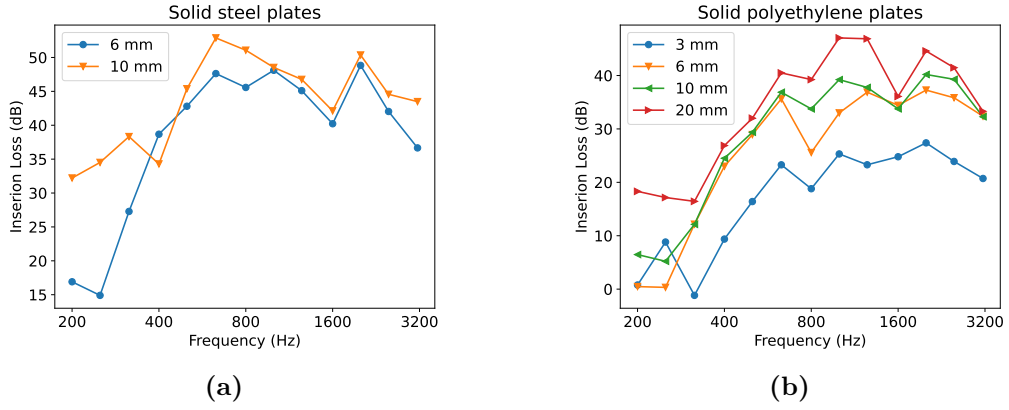**Figure I.5.1:** Third octave band IL for the solid plates of Set E: (a) steel and (b) polyethylene.

approximation [25] of the critical frequency f_c in Hz:

$$f_c = \frac{c^2}{\pi h}\sqrt{\frac{3\rho(1-\nu^2)}{E}}, \tag{I.5.2}$$

where c denotes the speed of sound in the air in $\mathrm{m\,s^{-1}}$, h the thickness of the plate in m, ν the Poisson ratio, and E the Young modulus in GPa. To take into account radiation losses for frequencies above the critical frequency f_c, we follow [25] and approximate the IL for $f > f_c$ by

$$\mathrm{IL} = 20\log_{10}(\mu f) + 10\log_{10}\frac{f}{f_c} + 10\log_{10}\eta + 5\log_{10}\left(1 - \frac{f_c}{f}\right) - 47, \tag{I.5.3}$$

where the radiation losses are for $f > f_c$ are given by

$$\eta = \frac{\rho_0 c}{\omega\mu\sqrt{1 - f_c/f}},$$

with ρ_0 being the mass density of the air in $\mathrm{kg\,m^{-3}}$, and $\omega = 2\pi f$ the angular frequency.

For the steel and polyethylene plates we record the rounded frequencies according to formula (I.5.2) in Table I.2. We note that for steel the critical frequencies f_c are in the center of our measurement range, while for the polyethylene plates only the 20 mm plate has a critical frequency in the range and it is close to the upper bound. In Figure I.5.2, we show the measured IL in the third octave bands, for (a) steel plates of thickness 6 mm and 10 mm, and (b) polyethylene plates of thickness 3–20 mm. In Figure I.5.2a, we combine the IL approximations (I.5.1) and (I.5.3). In Figure I.5.2b, we only show the mass law approximation (I.5.1), neglecting the radiation losses. We observe that for the steel and polyethylene plates, the measured IL agree quite well with the mass law (I.5.1) the in frequency ranges below the critical frequencies f_c. For the steel plates, in the frequency regions above the critical frequencies, we observe that the measured IL is significantly lower than what is indicated by the mass law (I.5.1), and that the radiation loss approximation (I.5.3) captures the

level of sound reduction in the sense that the predicted IL is reduced below the mass law. Also for the polyethylene plates, we observe that the measured IL stays significantly below the mass law well before the critical frequencies. A reason for this might be bigger radiation losses than predicted by our chosen model, as well as some significant viscous losses due to shear forces for the polyethylene plates.

For the ME and PE plates, drops in the IL are observed well below the critical frequencies f_c, which is visible in Figures I.5.1, as compared with half of the critical frequency $f_c/2$ according to Table I.2. This might be caused by stiffness controlled resonances of the plates or some part of the experimental setup.
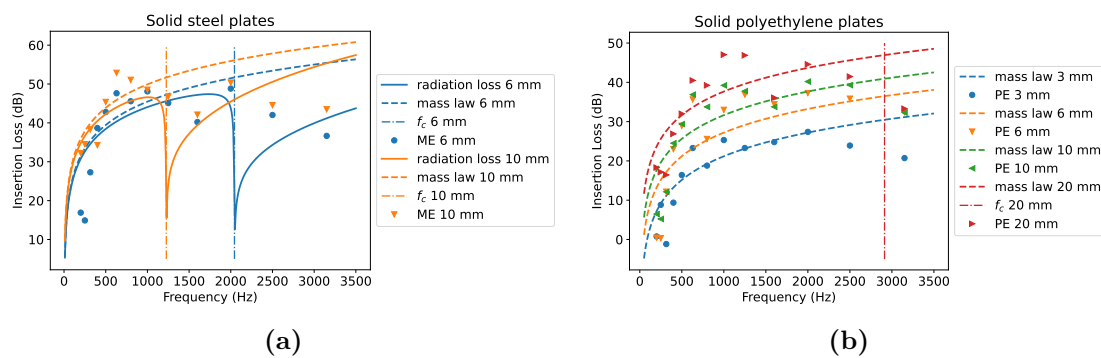
Figure I.5.2: Third octave band measured IL for the solid plates of Set E and the mass law approximation for (a) steel and (b) polyethylene plates.

Table I.2: Critical frequencies f_c for the solid plates.

Plate	Thickness (mm)	f_c (kHz)
ME	6	2.0
ME	10	1.2
PE	3	19
PE	6	9.7
PE	10	5.8
PE	20	2.9

Conclusions

In the present work a comparative experimental study of sound insertion loss (IL) for perforated plates with viscoelastic filling is performed. Since the diameter of the perforation is 6 mm, it is the case of so-called macro-perforation. We compare the IL for perforated plates filled with polyurethane and grease, with the IL for solid plates.

In the first part of the experiment, we investigate the effect of the filling on the sound absorption properties for throughout filled perforation, and compare the IL with the one for solid plates. We conclude that the IL for both solid and perforated

plates follows the mass law for most of the frequencies. However, for some narrow frequency ranges, we observe a considerable difference in the IL. For example, for 20 mm thick plastic plates, the PU filling gives up to 17 dB IL difference in the frequency range 1450–1600 Hz, compared with the solid plate.

The second part of the experiment concerns layered plates with viscoelastic inclusions. We have found that inserting a perforated layer with pseudoplastic (grease) filling between two solid plates without considerable changes in mass, leads to the effective decrease of the IL for most of the frequencies. Namely, the mass of a 10 mm solid metal sample and of a layered sample with 10 mm filled perforated plate between the two solid plastic ones differ by about 2%, while the difference in the sound IL reaches 10 dB for frequencies in the range 800–1600 Hz. Similarly, considering a solid 10 mm plastic sample and a layered 9 mm plastic sample with grease inclusions, we observe more than 10 dB difference in IL for frequencies 630–3150 Hz, for essentially the same mass. It would be of large interest to compare both theoretically and experimentally the plates with throughout filled perforation and isolated inclusions for several types of filling, as well as investigate the influence of the perforation size and shape.

References

[1]   J.F. Allard and N. Atalla. *Propagation of Sound in Porous Media: Modelling Sound Absorbing Materials, Second Edition.* Dec. 2009, p. 358. ISBN: 9780470746615. DOI: 10.1002/9780470747339.

[2]   N. Atalla, R. Panneton, F. C. Sgard, and X. Olny. "Acoustic absorption of macro-perforated porous materials". In: *Journal of sound and vibration* 243.4 (2001), pp. 659–678.

[3]   N. Atalla and F. Sgard. "Modeling of perforated plates and screens using rigid frame porous models". In: *Journal of Sound and Vibration* 303 (June 2007), pp. 195–208. DOI: 10.1016/j.jsv.2007.01.012.

[4]   K.-T. Chen. "Study on the acoustic transmission loss of a rigid perforated screen". In: *Applied Acoustics* 47.4 (1996), pp. 303–318.

[5]   C. Maury and T. Bravo. "Enhanced modal matching method for macro- and micro-perforated plates". In: *Journal of Sound and Vibration* 500 (2021), p. 116042. ISSN: 0022-460X. DOI: 10.1016/j.jsv.2021.116042.

[6]   J. Carbajo, J.M. Molina-Jordá, L.P. Maiorano, and N.X. Fang. "Sound absorption of macro-perforated additively manufactured media". In: *Applied Acoustics* 182 (2021), p. 108204. DOI: 10.1016/j.apacoust.2021.108204.

[7]   J. Carbajo, S. Ghaffari Mosanenzadeh, S. Kim, and N. X. Fang. "Sound absorption of acoustic resonators with oblique perforations". In: *Applied Physics Letters* 116.5 (2020), p. 054101. DOI: 10.1063/1.5132886.

[8]   M. Kleiner. *Acoustics and Audio Technology.* Oct. 2011. ISBN: 978-1604270525.

[9] J.-P. Groby, O. Dazel, A. Duclos, L. Boeckx, and L. Kelders. "Enhancing the absorption coefficient of a backed rigid frame porous layer by embedding circular periodic inclusions". In: *The Journal of the Acoustical Society of America* 130.6 (2011), pp. 3771–3780.

[10] H. Hong and S.-K. Lau. "Effects of inclusion shapes within rigid porous materials on acoustic performance". In: *Proceedings of Meetings on Acoustics 164ASA*. Vol. 18, 1. Acoustical Society of America. 2012, p. 040010.

[11] M. R. F. Kidner, C. R. Fuller, and B. Gardner. "Increase in transmission loss of single panels by addition of mass inclusions to a poro-elastic layer: Experimental investigation". In: *Journal of Sound and Vibration* 294.3 (2006), pp. 466–472.

[12] R. W. Style, R. Tutika, J. Young Kim, and M. D. Bartlett. "Solid–liquid composites for soft multifunctional materials". In: *Advanced Functional Materials* 31.1 (2021), p. 2005804.

[13] M. A. Biot. "Theory of propagation of elastic waves in a fluid-saturated porous solid. II. Higher frequency range". In: *The Journal of the acoustical Society of america* 28.2 (1956), pp. 179–191.

[14] ASTM E2611-09. *Standard Test Method for Measurement of Normal Incidence Sound Transmission of Acoustical Materials Based on the Transfer Matrix Method*. West Conshohocken, Pa.: ASTM, 2009. URL: www.astm.org.

[15] ISO Central Secretary. *Acoustics – Determination of sound absorption coefficient and impedance in impedance tubes – Part 2: Transfer-function method*. en. Standard ISO 10534-2:1998. Geneva, C. H.: International Organization for Standardization, 1998. URL: https://www.iso.org/standard/22851.html.

[16] ISO Central Secretary. *Acoustics – Measurement of sound absorption in a reverberation room*. en. Standard ISO 354:2003. Geneva, C. H.: International Organization for Standardization, 2003.

[17] *Transmission loss tube and impedance tube kit, type 4206*. https://www.bksv.com/en/products/transducers/acoustic/Acoustic-material-testing-kits/transmission-loss-and-impedance-tube-kits-4206. Accessed: 2023-04-21.

[18] *MATC — Acoustic Test Cabin*. https://mecanum.com/measuring-instruments/acoustic-test-cabin/. Accessed: 2023-04-21.

[19] *Mecanum Acoustic Test Cabin Technical Data Sheet*. https://mecanum.com/wp-content/uploads/2022/12/MATC-Mecanum-Acoustic-Test-Cabin.pdf. Accessed: 2023-04-21.

[20] ISO Central Secretary. *ISO 10140–2:2021, Acoustics — Laboratory measurement of sound insulation of building elements — Part 2: Measurement of airborne sound insulation*. en. Standard ISO 10140-2:2021. Geneva, C. H.: International Organization for Standardization, 2021. URL: https://www.iso.org/standard/79487.html.

[21] ASTM E90-09. *Standard Test Method for Laboratory Measurement of Airborne Sound Transmission Loss of Building Partitions and Elements.* West Conshohocken, Pa.: ASTM, 2016. URL: `www.astm.org`.

[22] ISO Central Secretary. *ISO 15186–1:2000, Acoustics – Measurement of Sound Insulation in Buildings and of Building Elements Using Sound Intensity – Part 1: Laboratory Measurements.* en. Standard ISO 15186-1:2000. Geneva, C. H.: International Organization for Standardization, 2000. URL: `https://www.iso.org/standard/26097.html`.

[23] ASTM E2249-02. *Standard Test Method for Laboratory Measurement of Airborne Sound Transmission Loss of Building Partitions and Elements Using Sound Intensity.* West Conshohocken, Pa.: ASTM, 2016. URL: `www.astm.org`.

[24] O. Robin, N. Atalla, and A. Berry. "Estimating transmission loss in coupled reverberant-anechoic rooms by measuring sound intensity with and without a test specimen". In: *The Journal of the Acoustical Society of America* 141 (Mar. 2017), pp. 1896–1899. DOI: `10.1121/1.4978039`.

[25] A. Nilsson and B. Liu. *Vibro-Acoustics, Volume 2.* Springer Berlin Heidelberg, Jan. 2016, pp. 1–452. ISBN: 978-3-662-47933-9. DOI: `10.1007/978-3-662-47934-6`.

[26] *Soudal International.* `https://www.soudal.com/`. Accessed: 2022-03-22.

[27] Interstellar Research. *Data AcQuisition And Real-Time Analysis.* Version 11.5.3. Mar. 28, 2022. URL: `https://www.daqarta.com/`.

[28] K. O. Ballagh. "Accuracy of prediction methods for sound transmission loss". In: *INTER-NOISE and NOISE-CON congress and conference proceedings.* Vol. 2004, 4. Institute of Noise Control Engineering. 2004, pp. 3095–3102.

PAPER II

Iterative FEM-Scheme for a Solid-Fluid Acoustic Problem[1]

Andrei Karzhou[2]

UiT The Arctic University of Norway

Abstract

We propose an iterative method for solution of a coupled acoustic fluid-solid interaction model. Assuming harmonic excitation in time, we use the pressure-displacement formulation of the acousto-elastic problem. The fluid is assumed to be ideal inviscid compressible medium governed by a wave equation for the acoustic pressure. The linear isotropic elastic structure is described by elasto-dynamic equations for the displacement field. We impose kinematic and dynamic conditions at the interface: The fluid particles velocity matches the velocity of the solid, and the balance of normal stresses holds. In the proposed iterative method, the fluid and solid subproblems are solved alternatingly, taking into account the interface conditions. The convergence of the iterative algorithm is demonstrated numerically for fluid-solid structures with different periodic, as well as random interfaces. The algorithm is applied for comparison of acoustic properties of fluid-solid structures depending on the geometry of the rough interface.

Keywords: Solid-fluid interaction, pressure-displacement formulation, iterative method, sound attenuation.

---

[2]Corresponding author. E-mail andrei.karzhou@uit.no.

II.1 Introduction

The present work concerns the numerical simulation of an incompressible fluid interacting with a thin elastic structure through an interface with periodic geometry. The target application is the description of the acoustic properties of plates with rough surfaces, although the method presented here applies to other fluid–structure interaction problems.

Fluid-structure interactions arise in many engineering problems dealing with noise vibrations, structural-acoustic problems, wind-turbine aerodynamics, as well as in bio-medical problems like cardiovascular fluid-structure interactions (see e.g. [1], [2]). A coupled fluid-solid acoustic problem shows an interplay between structural deformations in the solid and the pressure load in the acoustic medium. In other words, acoustic waves in the fluid give rise to structural vibrations and vice versa. It is the interface interactions that determine the intensity of sound propagation in the structure. In [3] the authors show acoustic insulation of a hollow core periodic sandwich panel with incorporated resonant structures. These host structures with resonant cells are acoustic metamaterials. One of the main features of such materials is the presence of certain frequency ranges (acoustic stop bands) wherein the transmission of sound through the structure is significantly reduced compared to bulk materials without microstructure. The main advantage of using metamaterials in acoustics is that "waves can be affected by incorporating structural resonant elements of sub-wavelength sizes, i.e. features that are actually smaller than the wavelength of the waves to be affected" [3]. The geometry of the interface might also cause mode localization. In [4] the authors consider closed resonators with absorbing properties and irregular geometry. It is shown that the geometrical irregularity of the absorbent material leads to a special "astride" mode localization. These localized modes play significant role in the dissipation of the acoustic energy in the non-absorbing regions. In the noise abatement walls production, the geometry of the interface is an important factor, together with the speed of sound and the material-air density ratio [5]. One of the tasks in engineering design is to find an optimal shape for a structure susceptible to imposed constraints, as for example shape optimization in fluid-structure interaction problems (see e.g. [6, 7, 8]).

There are several reviews of numerical methods to compute fluid-solid interaction in acoustics [9, 10, 11]. Numerical methods for solving fluid-structure interaction problems can be divided into monolithic and partitioned. In a monolithic approach the whole system, that is the solid domain, the fluid one, and their coupling at the interface, is solved simultaneously. As noted in [9], this approach might be more accurate for some multidisciplinary problems, but is often very computationally expensive and heavy. A common tool to solve such coupled problems is the Finite Element Method (FEM) [12, 13, 14, 15, 16, 17]. That is why the partitioned approach is often used. In such case, the solid and fluid domains are considered as two computational domains with the interface conditions used explicitly as a coupling between the two domains. The partitioned approach is specially advantageous when the interface between the solid and fluid domains has a complicated structure, as in the examples we consider in Section "Numerical results". In the present work we

use the partitioned approach: We split the fluid-structure problem into fluid and structural subproblems and use separate solvers for these subproblems [18]. We verify the convergence of a suitable energy to confirm the convergence of the iteration scheme. The numerical computations are done in the partial differential equations solver FreeFEM++ [19].

In this paper we propose an iterative method for coupled acoustic fluid-solid interaction models for an interface with periodic microstructure. Assuming harmonic excitation in time, we use the pressure-displacement formulation for the acousto-elastic problem [20, 21]. The fluid is assumed to be ideal inviscid compressible medium governed by the wave equation for acoustic pressure. The linear isotropic elastic structure is described by elasto-dynamic equations for the displacement field. We impose kinematic and dynamic conditions at the interface: the fluid particles velocity matches the velocity of the solid, and the balance of normal stresses holds. The method is applied to the sound damping problem for interfaces with different geometries. Namely, we compare the displacement on the side of the plate opposed to the fluid for five different geometries: flat, squared, toothed, circles, and random. We derive strong and weak formulation of a coupled solid-fluid interaction problem in Section "Model problem". The computational process of solving the problem is described in Section "Iterative algorithm". Then we demonstrate the solution of the problem for various materials and interfaces, and numerical convergence of the iterative scheme in Section "Numerical results". Finally we summarize our work in Section "Conclusion".

II.2 Model problem

In this section we formulate a mathematical model which is used in the sequel for the numerical computations (see, e.g. [20]). Let the solid (elastic strip) and the fluid (air) occupy rectangular domains such that $\Omega_f = (0, L) \times (0, L)$ be the fluid domain, and let the solid domain Ω_s have thickness $W > 0$, as shown in Figure II.2.1. The interface between the two domains is denoted by Γ. The rest of the boundary of the solid part is $\Gamma_{Ns} \cup \Gamma_{D_s} = \partial\Omega_s \setminus \Gamma$. The boundary of the fluid part consists of three parts $\partial\Omega_f = \Gamma_{Nf} \cup \Gamma \cup \Gamma_{D_f}$, as shown in Figure II.2.1.

We emphasize that the problem formulation and the proposed iterative algorithm for solution of the fluid-structure interaction problem is valid in three dimensions. We choose, however, to present a model problem and numerical examples in two dimensions.

We consider several interface geometries shown in Figure II.2.2. There is a geometrical constraint for the solid samples of different interface shape, namely, the area of the domain Ω_s is preserved. In the case of squared and triangular interfaces shown in Figure II.2.2 (b), (c) respectively, the width of the tooth forming corresponding interface is equal to half the width of the sample with a straight interface. The height of each tooth is chosen from the condition of dividing the height L of the sample with a flat interface into N equal parts ($N = 37$ for the squared interface, $N = 38$ for the triangular one). The diameter of each circle forming the rounded interface presented in Figure II.2.2 (d) is chosen based on splitting the
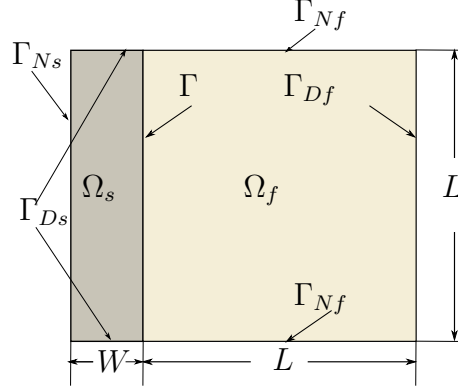
Figure II.2.1: Geometry in the solid-fluid interaction model problem.
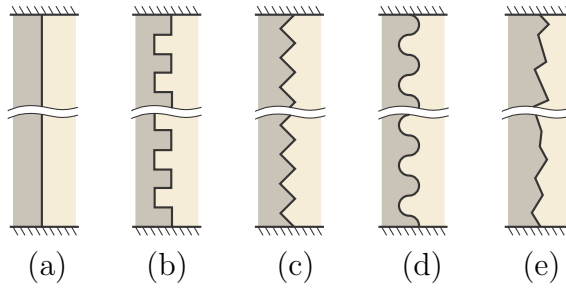
Figure II.2.2: Interface geometries: (a) flat, (b) squared, (c) triangular, (d) rounded, (e) random.

height of the sample with a flat interface into $N = 37$ elements. Random interface shown in Figure II.2.2 (e), is built up from $N = 37$ straight elements. The length of each element is randomly chosen.

II.2.1   Strong and weak formulation of a coupled solid-fluid interaction problem

In this section we present strong and weak formulation of the problem. We use the equations of elastodynamics on solid domain Ω_s with boundaries Γ_{Ns}, Γ_{Ds} and Γ and wave equation on the domain Ω_f with boundaries Γ_{Nf}, Γ_{Df} and Γ as shown in Figure II.2.1. Denoting by U the displacement in the elastic material, and by σ the stress matrix, we obtain the following wave (balance) equation on the domain Ω_s

$$\operatorname{div} \sigma = \rho_s \frac{\partial^2 U}{\partial t^2} \quad \text{in } \Omega_s,$$

where ρ_s is density of the elastic material. By Hooke's law, the stress is $\sigma = A\varepsilon(U)$, and the balance equation reads

$$\operatorname{div}(A\varepsilon(U)) = \rho_s \frac{\partial^2 U}{\partial t^2} \quad \text{in } \Omega_s,$$

where A is the material matrix, and ε is symmetrical part of gradient, that is $\varepsilon = (\nabla + \nabla^T)/2$.

Considering a harmonic excitation with a certain frequency ω, and denoting $U(x,t) = \tilde{u}(x)e^{-i\omega t}$, we obtain the following balance equation for $\tilde{u}(x)$

$$\operatorname{div} \sigma(\tilde{u}) = -\omega^2 \rho_s \tilde{u} \quad \text{in } \Omega_s. \tag{II.2.1}$$

Two of the four sides of the rectangle Ω_s are fixed, where we impose homogeneous Dirichlet conditions for the displacement $\tilde{u}$

$$\tilde{u} = 0 \quad \text{on } \Gamma_{Ds}, \tag{II.2.2}$$

while Γ is subjected to an external (from the fluid side) excitation.

We set traction-free boundary condition on Γ_{Ns}

$$\sigma(\tilde{u})\, n_s = 0 \quad \text{on } \Gamma_{Ns},$$

where n_s is the external unit normal vector to Ω_s.

In the air part Ω_f, the harmonically varying in time sound pressure is $P(x,t) = \tilde{p}^*(x)e^{-i\omega t}$. The acoustic wave equation for the sound pressure P is

$$\Delta P = \frac{1}{c_a^2}\frac{\partial^2 P}{\partial t^2} \quad \text{in } \Omega_f, \tag{II.2.3}$$

where $c_a = 344\ m/s$ is speed of sound in the air at normal ambient conditions. For $\tilde{p}^*(x)$ the acoustic wave equation (II.2.3) is transformed into Helmholtz equation

$$\Delta \tilde{p}^* + \frac{\omega^2}{c_a^2}\tilde{p}^* = 0 \quad \text{in } \Omega_f.$$

The boundary $\partial\Omega_f$ consists of the interface Γ between the solid and the air, the free part Γ_{Nf} where we impose Neumann boundary conditions, and Γ_{Df} where we have nonhomogeneous Dirichlet boundary conditions

$$\nabla \tilde{p}^* \cdot n_f\big|_{\Gamma_{Nf}} = 0, \quad \tilde{p}^*\big|_{\Gamma_{Df}} = p_e.$$

Here p_e is the pressure acting on the right side of Ω_f as illustrated in Figure II.2.1, and n_f is an exterior unit normal to Ω_f.

As mentioned above, on the interface Γ we impose the continuity of pressure condition

$$\sigma(\tilde{u})\, n_s = -\tilde{p}^*\, n_s,$$

Note that $n_f = -n_s$ on the interface Γ.

Recalling the linearized Euler equation in the fluid part Ω_f, we obtain

$$\nabla P \cdot n_f = -\rho_f \frac{\partial^2 U_f}{\partial t^2} \cdot n_f \quad \text{on } \Gamma,$$

where U_f is the displacement in the fluid. Using the harmonic time dependence, and using the continuity of the displacement on the interface Γ, we get

$$\nabla \tilde{p}^* \cdot n_f\big|_\Gamma = \omega^2 \rho_f \tilde{u} \cdot n_f\big|_\Gamma.$$

To deal with the non-homogeneous Dirichlet boundary condition on Γ_{Df}, we introduce $\tilde{p}$ by setting

$$\tilde{p} = \tilde{p}^* - p_e.$$

Then $\tilde{p}$ satisfies the homogeneous Dirichlet boundary condition on Γ_{Df} and Neumann boundary conditions on Γ_{Nf}

$$\tilde{p}\big|_{\Gamma_{Df}} = 0, \quad \nabla\tilde{p} \cdot n_f\big|_{\Gamma_{Nf}} = 0. \tag{II.2.4}$$

Continuity of pressure condition reads

$$\sigma(u)n_s = -(\tilde{p} + p_e)\,n_s, \tag{II.2.5}$$

and the equation for $\tilde{p}$ is

$$\Delta\tilde{p} + \frac{\omega^2}{c_a^2}\tilde{p} = -\frac{\omega^2}{c_a^2}p_e \quad \text{in } \Omega_f. \tag{II.2.6}$$

Finally, the coupled system for u and p^* takes the form

$$
\begin{aligned}
\operatorname{div}\sigma(\tilde{u}) &= -\omega^2\rho_s\tilde{u} & &\text{in } \Omega_s, \\
\sigma(\tilde{u}) &= A\varepsilon(\tilde{u}) & &\text{in } \Omega_s, \\
\tilde{u} &= 0 & &\text{on } \Gamma_{Ds}, \\
\sigma(\tilde{u})n_s &= 0 & &\text{on } \Gamma_{Ns}, \\
\sigma(\tilde{u})n_s &= -(\tilde{p} + p_e), & &\text{on } \Gamma, \\
\nabla\tilde{p} \cdot n_f &= \omega^2\rho_f\tilde{u} \cdot n_f & &\text{on } \Gamma, \\
\Delta\tilde{p} + \frac{\omega^2}{c_a^2}\tilde{p} &= -\frac{\omega^2}{c_a^2}p_e & &\text{in } \Omega_f, \\
\nabla\tilde{p} \cdot n_f &= 0 & &\text{on } \Gamma_{Nf}, \\
\tilde{p} &= 0 & &\text{on } \Gamma_{Df}.
\end{aligned}
\tag{II.2.7}
$$

Equations (II.2.7) present a strong formulation of our problem. To derive a weak formulation of (II.2.7), which is used for the computations in FreeFEM++, we i) multiply both governing equations (II.2.1), (II.2.6) for $\tilde{u}$ and $\tilde{p}$ by smooth test functions, and ii) integrate by parts over the corresponding domains Ω_s and Ω_f. The weak formulation for balance equation (II.2.1) with the homogeneous Dirichlet boundary condition (II.2.2) and the interface condition (II.2.5) is: Find $\tilde{u} \in H^1(\Omega_s)$ such that $\tilde{u} = 0$ on Γ_{Ds} and satisfying the following integral identity:

$$\int_{\Omega_s} \epsilon(\tilde{u}) \cdot A\,\epsilon(v)\,dx - \omega^2\rho_s\int_{\Omega_s}\tilde{u} \cdot v\,dx = -\int_{\Gamma}\tilde{p}\,n_s \cdot v\,dS - \int_{\Gamma}p_e\,(n_s \cdot v)\,dS, \tag{II.2.8}$$

for any test function $v \in H^1(\Omega_s)$ such that $v = 0$ on Γ_{Ds}.

The weak formulation for the acoustic wave equation (II.2.6) with the homogeneous boundary condition (II.2.4) is: Find $\tilde{p} \in H^1(\Omega_f)$ such that $\tilde{p} = 0$ on Γ_{Df} and satisfying the following integral identity:

$$\int_{\Omega_f}\nabla\tilde{p} \cdot \nabla q\,dx - \frac{\omega^2}{c_a^2}\int_{\Omega_f}\tilde{p}q\,dx = \frac{\omega^2}{c_a^2}\int_{\Omega_f}p_e q\,dx + \omega^2\rho_f\int_{\Gamma}(\tilde{u} \cdot n_f)q\,dS, \tag{II.2.9}$$

for any test function $q \in H^1(\Omega_f)$ such that $v = 0$ on Γ_{Df}.

Equations (II.2.8) and (II.2.9) constitute a coupled system in a weak form. For verification of existence of solutions to this system, it is convenient to write it as follows: Find $(\tilde{u}, \tilde{p}) \in H^1(\Omega_s) \times H^1(\Omega_f)$ such that $\tilde{u} = 0$ on Γ_{Ds} and $\tilde{p} = 0$ on Γ_{Df}, and

$$\int_{\Omega_s} \epsilon(\tilde{u}) \cdot A\,\epsilon(v)\,dx + \int_{\Omega_f} \nabla\tilde{p} \cdot \nabla q\,dx - \omega^2 \rho_s \int_{\Omega_s} \tilde{u} \cdot v\,dx - \frac{\omega^2}{c_a^2} \int_{\Omega_f} \tilde{p}q\,dx$$

$$- \omega^2 \rho_f \int_{\Gamma} (\tilde{u} \cdot n_f)q\,dS + \int_{\Gamma} \tilde{p}\,n_s \cdot v\,dS$$

$$= \frac{\omega^2}{c_a^2} \int_{\Omega_f} p_e q\,dx - \int_{\Gamma} p_e\,(n_s \cdot v)\,dS, \tag{II.2.10}$$

for all $(v, q) \in H^1(\Omega_s) \times H^1(\Omega_f)$, such that $v = 0$ on Γ_{Ds} and $q = 0$ on Γ_{Df}.

By the Fredholm alternative, as long as ω is not on the spectrum of the problem

$$\int_{\Omega_s} \epsilon(u) \cdot A\,\epsilon(v)\,dx + \int_{\Omega_f} \nabla p \cdot \nabla q\,dx - \omega^2 \rho_s \int_{\Omega_s} u \cdot v\,dx - \frac{\omega^2}{c_a^2} \int_{\Omega_f} pq\,dx$$

$$- \omega^2 \rho_f \int_{\Gamma} (u \cdot n_f)q\,dS + \int_{\Gamma} p\,n_s \cdot v\,dS = 0, \tag{II.2.11}$$

for any $p_e \in H^1(\Omega_f)$, there exists a unique solution $(\tilde{u}, \tilde{p}) \in H^1(\Omega_s) \times H^1(\Omega_f)$, such that $\tilde{u} = 0$ on Γ_{Ds} and $\tilde{p} = 0$ on Γ_{Df}, of (II.2.10). Also under suitable orthogonality condition on the data p_e, uniqueness may be guaranteed. Some eigenvalues to (II.2.11) appear as peaks in the frequency response graphs, and this is illustrated in the numerical examples below.

In the next section we develop an iterative procedure for numerical solution of (II.2.8)–(II.2.9). To this end, we pass to the dimensionless variables.

II.2.2 Nondimensionalization

In this subsection we pass to the dimensionless variables. Namely, let us introduce the following dimensionless quantities

$$x = \frac{\tilde{x}}{d}, \quad A = \frac{\tilde{A}}{E}, \quad p = \frac{\tilde{p}}{p_0}, \quad p^* = \frac{\tilde{p}^*}{p_0} = \frac{\tilde{p} - p_e}{p_0} \quad u_i = \frac{\tilde{u}_i}{d}, \tag{II.2.12}$$

where p_0 is some reference pressure value, p_e is the pressure acting on the right side of Ω_f, and E is the Young modulus. Under the change of variables (II.2.12) we have

$$d\tilde{x} = d^2 dx, \quad d\tilde{S} = d\,dS, \quad \nabla_{\tilde{x}} = \frac{1}{d}\nabla_x.$$

Making the change of variables in (II.2.8) and (II.2.9), and keeping the same notations for the rescaled domains Ω_s, Ω_f (that are now rectangles of size $1 \times (L/d)$ and

$(L/d) \times (L/d))$ and their boundaries, we get

$$
\begin{cases}
\dfrac{E}{p_0} \displaystyle\int_{\Omega_s} \epsilon(u) \cdot A\, \epsilon(v)\, dx + \int_{\Gamma} p\, n_s \cdot v\, dS + \dfrac{p_e}{p_0} \int_{\Gamma} n_s \cdot v\, dS = \omega^2 d^2 \dfrac{\rho_s}{p_0} \int_{\Omega_s} u \cdot v\, dx, \\[4mm]
\displaystyle\int_{\Omega_f} \nabla p \cdot \nabla q\, dx - \dfrac{\omega^2 d^2}{c_a^2} \int_{\Omega_f} pq\, dx - \omega^2 d^2 \dfrac{\rho_f}{p_0} \int_{\Gamma} (u \cdot n_f) q\, dS = \dfrac{\omega^2 d^2}{c_a^2} \dfrac{p_e}{p_0} \int_{\Omega_f} q\, dx. \\[4mm]
u = 0 \quad \text{on } \Gamma_{Ds}, \qquad p = 0 \quad \text{on } \Gamma_{Df}.
\end{cases}
$$

$$
(\text{II}.2.13)
$$

System (II.2.13) is solved using an iterative procedure presented in the next section.

II.3 Iterative algorithm

The solution of the task is provided by iterative approach. On each iteration two weak formulations, one for fluid part and another one for solid part, are solved separately. Both weak formulations have a cross-term coming from the interface condition. The latter plays the main role in the iterations between the fluid and solid parts.

Iterative algorithm

Step 0: Set $u_0 = 0$ on Γ.

Step 1: On the ith iteration $(i = 1, \dots, N)$,

1) Solve for the pressure in the fluid part p_i given the displacement u_{i-1} on the interface from the previous iteration:

$$
\int_{\Omega_f} \nabla p_i \cdot \nabla q\, dx - \frac{\omega^2 d^2}{c_a^2} \int_{\Omega_f} p_i q\, dx = \omega^2 d^2 \frac{\rho_f}{p_0} \int_{\Gamma} (u_{i-1} \cdot n_f) q\, dS + \frac{\omega^2 d^2}{c_a^2} \frac{1}{p_0} \int_{\Omega_f} p_e\, q\, dx.
$$

For $i = 1$ use $u = u_0$.

2) Solve for the displacement u_i in the solid, given the calculated pressure on interface:

$$
\frac{E}{p_0} \int_{\Omega_s} \epsilon(u_i) \cdot A\, \epsilon(v)\, dx + \omega^2 d^2 \frac{\rho_s}{p_0} \int_{\Omega_s} u_i \cdot v\, dx = - \int_{\Gamma} p_i\, n_s \cdot v\, dS - \frac{1}{p_0} \int_{\Gamma} p_e\, n_s \cdot v\, dS.
$$

To establish the convergence of the iterative procedure, we rewrite (II.2.13) moving the interface terms to the right-hand side and summing up the two equations:

$$\frac{E}{p_0} \int_{\Omega_s} \epsilon(u)^T A \, \epsilon(v) \, dx - \omega^2 d^2 \frac{\rho_s}{p_0} \int_{\Omega_s} u \cdot v \, dx + \int_{\Omega_f} \nabla p \cdot \nabla q \, dx \tag{II.3.1}$$

$$- \frac{\omega^2 d^2}{c_a^2} \int_{\Omega_f} pq \, dx - \frac{\omega^2 d^2}{c_a^2} \frac{p_e}{p_0} \int_{\Omega_f} q \, dx$$

$$= - \int_{\Gamma} p \, n_s \cdot v \, dS - \frac{p_e}{p_0} \int_{\Gamma} n_s \cdot v \, dS + \omega^2 d^2 \frac{\rho_f}{p_0} \int_{\Gamma} (u \cdot n_f) q \, dS. \tag{II.3.2}$$

Similarly, summing up the weak forms on the ith iteration for u and the $(i + 1)^{\text{th}}$ iteration for p, and then subtracting (II.3.1) we obtain:

$$\frac{E}{p_0} \int_{\Omega_s} \epsilon(u_i - u)^T A \, \epsilon(v) \, dx - \omega^2 d^2 \frac{\rho_s}{p_0} \int_{\Omega_s} (u_i - u) \cdot v \, dx + \int_{\Omega_f} \nabla(p_{i+1} - p) \cdot \nabla q \, dx$$

$$- \frac{\omega^2 d^2}{c_a^2} \int_{\Omega_f} (p_{i+1} - p)q \, dx = - \int_{\Gamma} (p_i - p) \, n_s \cdot v \, dS - \omega^2 d^2 \frac{\rho_f}{p_0} \int_{\Gamma} (u_i - u) \cdot n_s q \, dS.$$

$$\tag{II.3.3}$$

Here we have taken into account that $n_f = -n_s$. We write a similar equation for the jth iteration, and subtract the latter from (II.3.3) to get

$$\frac{E}{p_0} \int_{\Omega_s} \epsilon(u_j - u_i)^T A \, \epsilon(v) \, dx - \omega^2 d^2 \frac{\rho_s}{p_0} \int_{\Omega_s} (u_j - u_i) \cdot v \, dx + \int_{\Omega_f} \nabla(p_{j+1} - p_{i+1}) \cdot \nabla q \, dx$$

$$- \frac{\omega^2 d^2}{c_a^2} \int_{\Omega_f} (p_{j+1} - p_{i+1})q \, dx + \omega^2 d^2 \frac{\rho_f}{p_0} \int_{\Gamma} (u_j - u_i) \cdot n_s q \, dS + \int_{\Gamma} (p_j - p_i) \, n_s \cdot v \, dS = 0.$$

$$\tag{II.3.4}$$

We introduce the cross term $E_{j,i}$ built up from two last terms in (II.3.4):

$$E_{j,i} = \omega^2 d^2 \frac{\rho_f}{p_0} \int_{\Gamma} (u_j - u_i) \cdot n_s(p_j - p_i) \, dS + \int_{\Gamma} (p_j - p_i) \, n_s \cdot (u_j - u_i) \, dS,$$

as equation (II.3.4) hold for any admissible q and v. To investigate the convergence of the iterative process, we study numerically how $E_{j,i}$ decays when the number of iterations grows. We consider two cases

a) $E_{i+1,i} = E_i \, (u_{i+1}, u_i, p_{i+1}, p_i) = \left(1 + \omega^2 d^2 \frac{\rho_f}{p_0}\right) \int_{\Gamma} (u_{i+1} - u_i) \cdot n_s(p_{i+1} - p_i) \, dS,$

b) $E_{N,i} = E_i \, (u_N, u_i, p_{i+1}, p_i) = \left(1 + \omega^2 d^2 \frac{\rho_f}{p_0}\right) \int_{\Gamma} (u_N - u_i) \cdot n_s(p_N - p_i) \, dS.$

Table II.1: Material parameters.

Material	Young's modulus E, GPa	Poisson's ratio ν	Density $\rho_s, t/m^3$
Steel	200.00	0.30	7.86
Glass	50.00	0.20	2.60
Concrete	17.00	0.15	1.50
Lead	13.80	0.43	11.35
HDPE	1.00	0.40	0.96
Rubber	0.05	0.49	0.92

In the next section we compute the energies $I_{i+1,i}$ and $I_{N,i}$

$$I_{i+1,i} = \int_{\Gamma} (u_{i+1} - u_i) \cdot n_s (p_{i+1} - p_i)\, dS, \qquad \text{(II.3.5)}$$

$$I_{N,i} = \int_{\Gamma} (u_N - u_i) \cdot n_s (p_N - p_i)\, dS, \qquad \text{(II.3.6)}$$

and show that the iterative algorithm converges numerically in selected cases.

II.4   Numerical results

To illustrate the proposed iterative scheme, we compute (u, p) for different geometries of the interface (see Figure II.2.2) and different materials (see Table II.1). Geometric parameters are as follows: $L = 0.4$ m, $W = 0.02$ m, $d = 0.01$ m. Reference pressure p_0 is chosen to be equal to 1 Pa.

The computations are performed in FreeFEM++ software [19] in two dimensions. Let the domains and the boundaries be denoted as shown in Figure II.2.1. The parts of the boundary Γ_{Ns}, Γ_{Ds}, Γ_{Nf}, and Γ_{Df} are discretized by the number of elements proportional to the length of the corresponding boundary part with five elements per unit length, i.e. the size of each element is $h = 0.2$. In the case of straight interface we take $N_{\Gamma} = 1078$ elements distributed uniformly with 16 elements per unit length on the boundary Γ. In the computational domains Ω_s and Ω_f the mesh has been generated by FreeFEM++. The mesh in Ω_s contains $n_v^s = 8327$ vertices, $n_t^s = 15671$ triangles, and $n_s^s = 981$ edges on the boundary. The mesh in Ω_f contains $n_v^f = 97046$ vertices, $n_t^f = 192629$ triangles, and $n_s^f = 1461$ edges on the boundary. We use piecewise affine finite elements P_1.

Figure II.4.1 presents the result of applying an iterative algorithm to the case of squared interface between rubber and air for the excitation with frequency $f = 500$ Hz. In Figure II.4.1(a) we present the original not deformed solid domain. As the result of the excitation of the solid-fluid structure, the solid domain is deformed as illustrated in Figure II.4.1(b). Figure II.4.1(c) demonstrates the distribution of von Mises stress in the solid body.
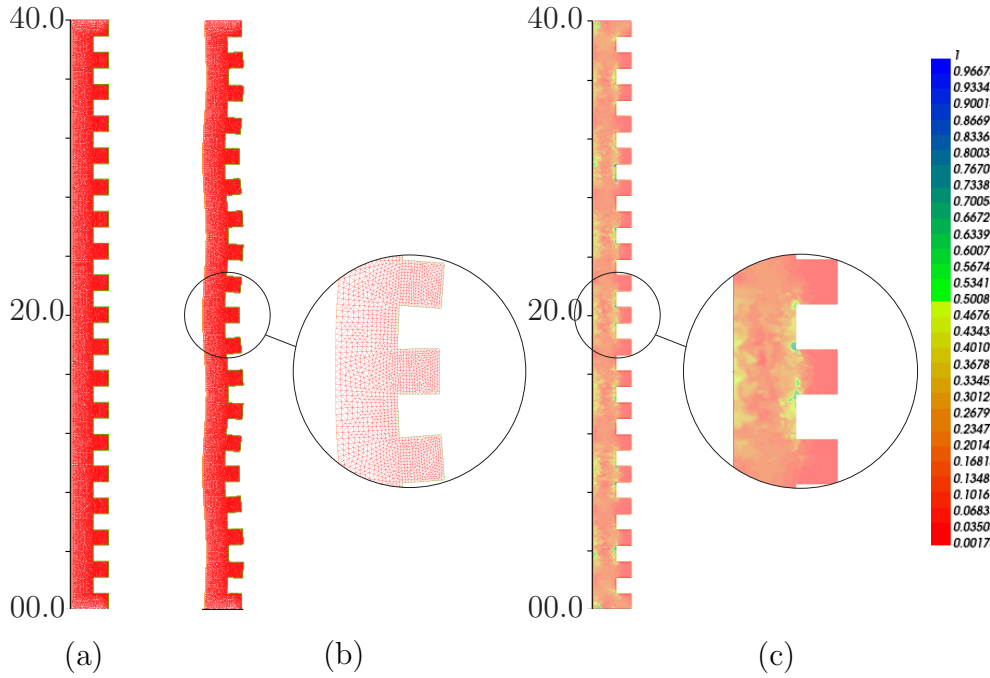
Figure II.4.1: Solid domain: (a) non-deformed, (b) deformed after excitation with $f = 500$ Hz and magnified by 200, (c) normalized von Mises stress with $\sigma_{max} = 0.000469408$ Pa.

II.4.1 Sound damping properties for different interface geometries

In order to compare the sound damping properties for different interface geometries, we calculate the L^2-norm of the displacement u on the backside boundary part Γ_{Ns} for frequencies in the range $[0, \dots, 1500]$ Hz. For brevity, we write $L^2(u)$ for the norm $\|u\|_{L^2(\Gamma_{Ns})}$. Figures II.4.2–II.4.7 show the result of the frequency sweep for all the studied materials and different interfaces between solid and fluid domains. There is one common feature in which we observe for all solid materials, namely, the presence of a peak at the frequency $f_a = 860$ Hz. This peak is due to the resonance in the fluid domain. The shape of the interface plays a significant role in the interaction between fluid and solid for frequencies in the range $[170, \dots, 860]$ Hz for the solids made of steel Figure II.4.2, concrete Figure II.4.3 and glass Figure II.4.4. In the case of HDPE Figure II.4.5 and lead Figure II.4.6, the influence of the different interfaces on the displacement is most pronounced for the frequency ranges $[140, \dots, 190]$ Hz, $[500, \dots, 860]$ Hz, and $[1200, \dots, 1500]$ Hz. For the solid made of rubber Figure II.4.7, the plot of the L^2-norm of the displacement for different shapes of the interface has peaks for the whole frequency range.

II.4.2 Numerical convergence of the iterative method

To validate the convergence of the proposed iterative method, we provide numerical computations of the energies $I_{i+1,i}$ (II.3.5) and $I_{N,i}$ (II.3.6) for different interface shapes. The numerical computations confirm that both $I_{i+1,i}$ and $I_{N,i}$ decrease
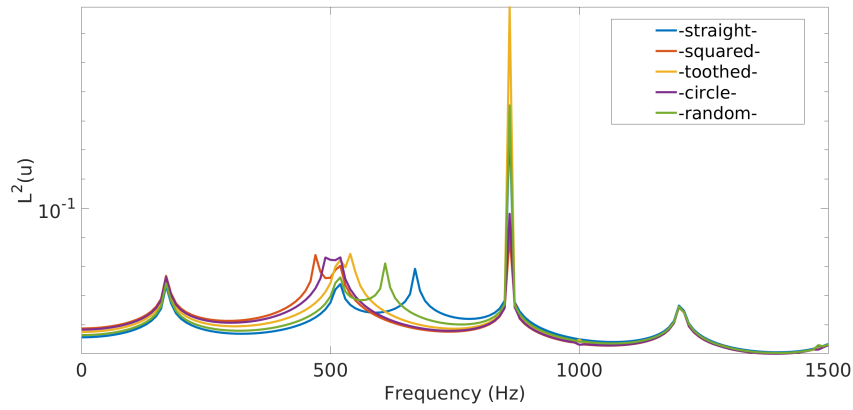
Figure II.4.2: Frequency sweep for the different geometries of the steel solid interface.

Figure II.4.3: Frequency sweep for the different geometries of the concrete solid interface.

Figure II.4.4: Frequency sweep for the different geometries of the glass solid interface.

monotonously for all interface geometries and for all the materials under consideration. Both interface energies stabilize after a certain amount of iterations.

Figure II.4.8 shows the dependence of the absolute values of $I_{i+1,i}$ and $I_{N,i}$ on the number of iterations for solids made of concrete with straight, squared, and random shapes of the interface. Similarly, Figure II.4.9 shows $I_{i+1,i}$ and $I_{N,i}$ vs. the iteration
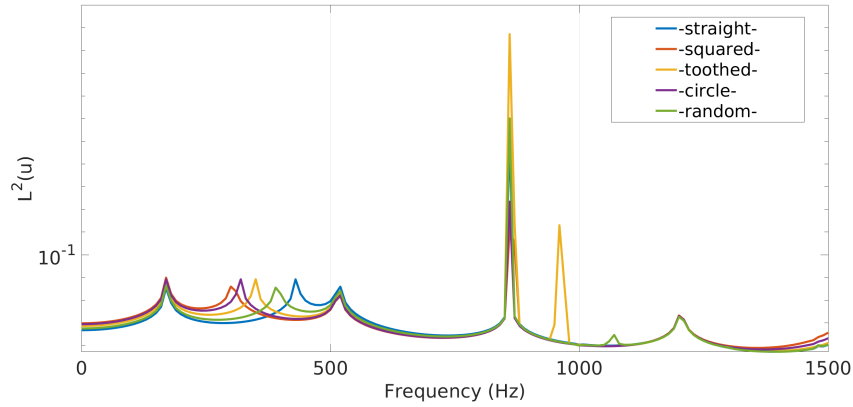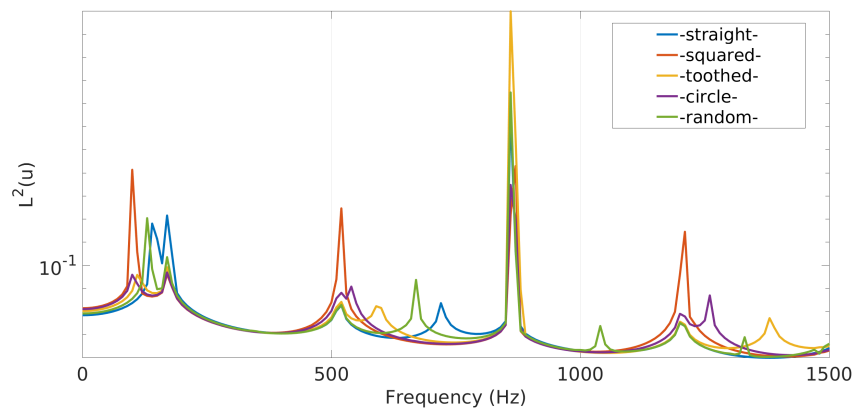
Figure II.4.5: Frequency sweep for the different geometries of the HDPE solid interface.

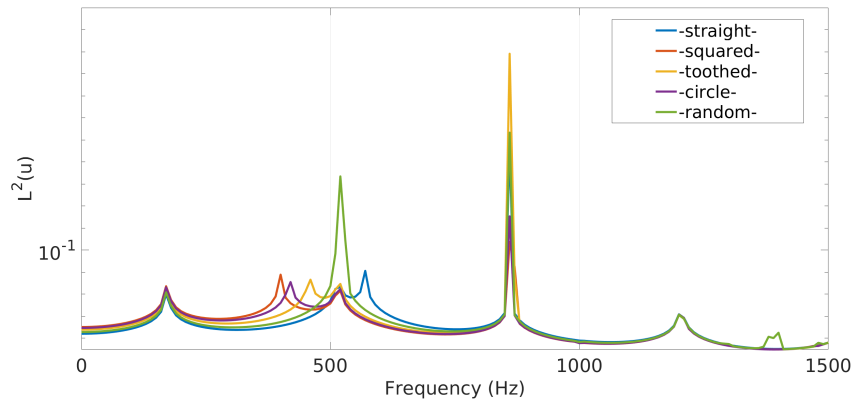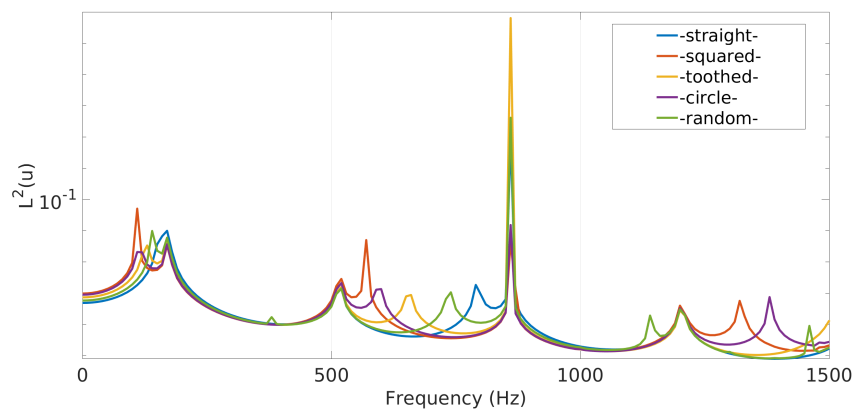**Figure II.4.6:** Frequency sweep for the different geometries of the lead solid interface.
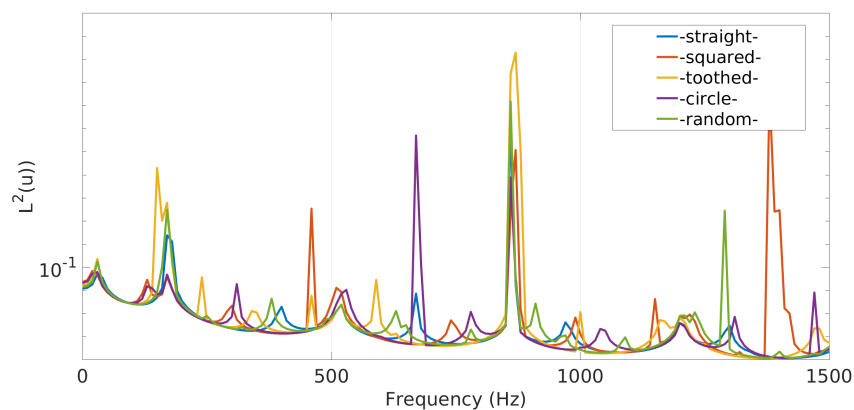
Figure II.4.7: Frequency sweep for the different geometries of the rubber solid interface.

number for the rubber elastic part with straight, squared, and random shapes of the interface.

In addition to the cross energies on the interface, we illustrate the convergence of the iterative process by evaluating the H^1 norm of the difference between neighbor iterations of displacement u and sound pressure p for the case of concrete (Figure
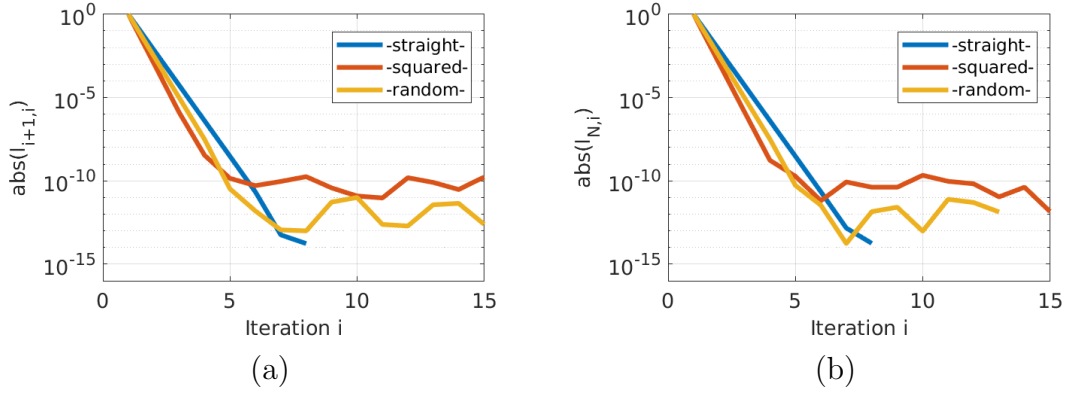
Figure II.4.8: Absolute value of (a) $I_{i+1,i}$ and (b) $I_{N,i}$ for concrete-air interface at $f = 500$ Hz.
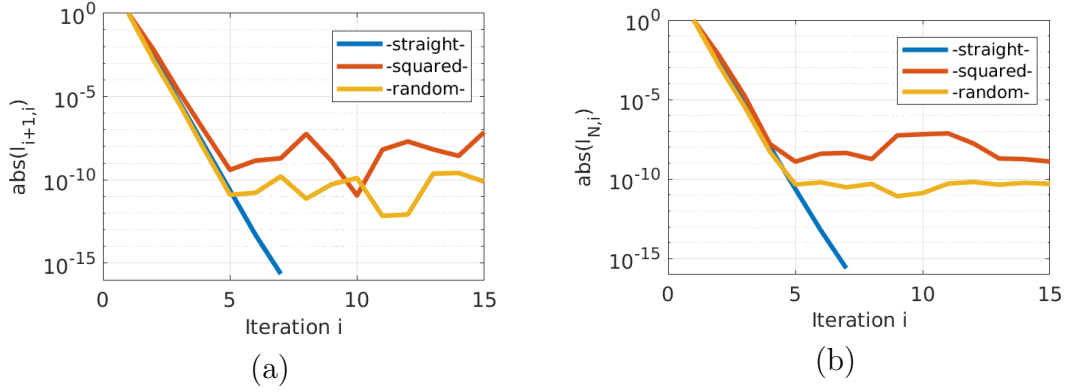
Figure II.4.9: Absolute value of (a) $I_{i+1,i}$ and (b) $I_{N,i}$ for rubber-air interface at $f = 500$ Hz.

II.4.10) and rubber (Figure II.4.11). Formulas for H^1 norms are as follows

$$H^1_{\Omega_s}(u_{i+1} - u_i) := \|u_{i+1} - u_i\|_{H^1(\Omega_s)} = \left(\int_{\Omega_s} \left(|u_{i+1} - u_i|^2 + |\nabla(u_{i+1} - u_i)|^2 \right) dx \right)^{1/2},$$

$$H^1_{\Omega_f}(p_{i+1} - p_i) := \|p_{i+1} - p_i\|_{H^1(\Omega_f)} = \left(\int_{\Omega_f} \left(|p_{i+1} - p_i|^2 + |\nabla(p_{i+1} - p_i)|^2 \right) dx \right)^{1/2}.$$

The value of the discrepancy becomes small and stabilizes already after about ten iterations.

Conclusion

In this work we have presented an iterative algorithm for solving a fluid-structure interaction problem under a harmonic excitation. The target problem is the description of acoustic properties, and in particular the insertion loss, for elastic plates with rough interface. We investigate the convergence of the iterative scheme numerically, and illustrate the proposed algorithm by applying it to a fluid-structure interaction
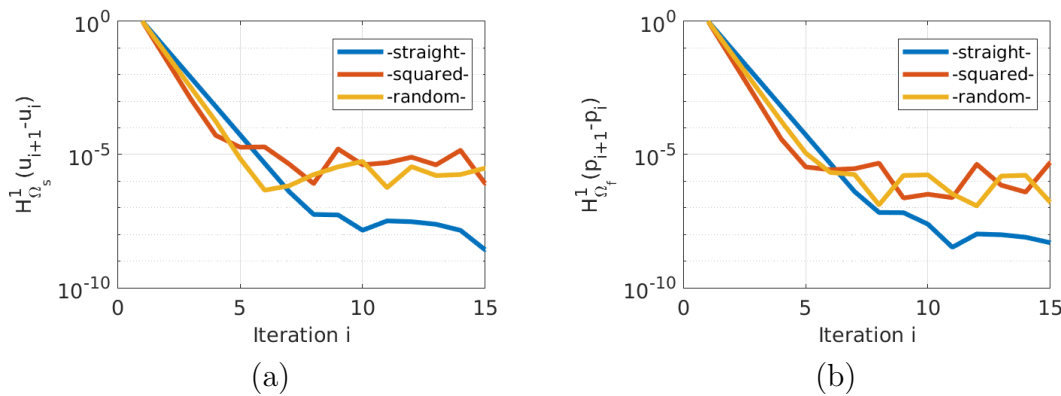
Figure II.4.10: H^1-norm of the difference between neighbor iterations for (a) displacement in concrete and (b) sound pressure in air for $f = 500$ Hz.
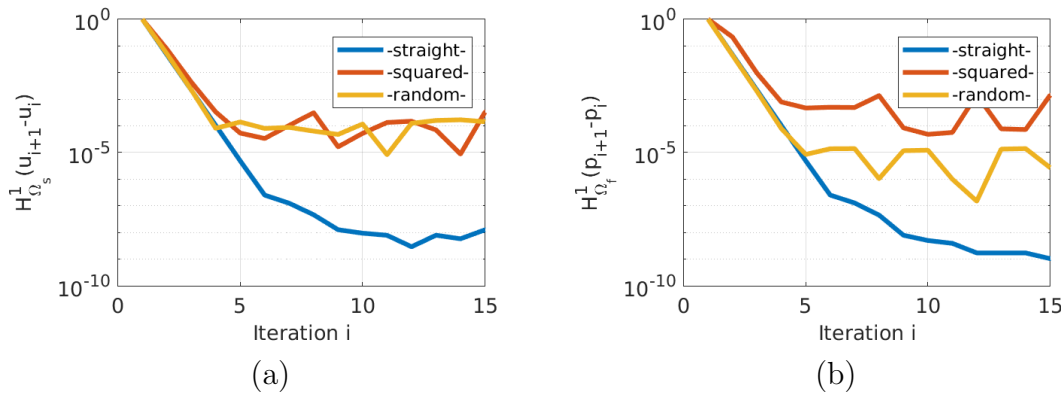
Figure II.4.11: H^1-norm of the difference between neighbor iterations for (a) displacement in rubber and (b) sound pressure in air for $f = 500$ Hz.

problem with a rough interface. Several different periodic geometries of the interface are considered, as well as a random one. We have compared the L^2-norm of the displacement on the back side of the plate, looking for an optimal geometry for sound damping. All these structures show similar trend and similar values of the L^2-norm of the displacement in the solid part, except for a few frequencies where the norm of the displacement for the random geometry is larger compared to periodic interface. Moreover, because of the resonance in the fluid domain, at the frequency $f_a = 860$ Hz we observe a peak in the displacement plot for all materials and interfaces. The convergence of the iterative scheme is shown numerically by computing the cross energy on the interface, as well as the H^1-norms of the displacements and sound pressure in solid and fluid domains, respectively. In all cases we observe good convergence already after ten iterations.

References

[1] Y. Bazilevs, K. Takizawa, and T. E. Tezduyar. *Computational fluid-structure interaction: methods and applications.* John Wiley & Sons, 2013.

PAPER II. FEM FOR SOLID-FLUID INTERACTION

[2] Jing T. X. "Chapter 1 - Introduction". In: *Fluid-Solid Interaction Dynamics.* Ed. by T. X. Jing. Academic Press, 2019, pp. 1–42. DOI: `10.1016/B978-0-12-819352-5.00001-X`.

[3] C. Claeys, E. Deckers, B. Pluymers, and W. Desmet. "A lightweight vibro-acoustic metamaterial demonstrator: Numerical and experimental investigation". In: *Mechanical Systems and Signal Processing* 70-71 (2016), pp. 853–880. ISSN: 0888-3270. DOI: `10.1016/j.ymssp.2015.08.029`.

[4] S. Félix, B. Sapoval, M. Filoche, and M. Asch. "Enhanced wave absorption through irregular interfaces". In: *Europhysics Letters* 85.1 (Jan. 2009), p. 14003. DOI: `10.1209/0295-5075/85/14003`.

[5] V. Kubytskyi, M. Filoche, and B. Sapoval. "Increased absorption due to localized resonances". In: *41st International Congress and Exposition on Noise Control Engineering 2012, INTER-NOISE 2012* 10 (Jan. 2012), pp. 8196–8203.

[6] N. Aghajari and M. Schäfer. "Efficient shape optimization for fluid–structure interaction problems". In: *Journal of Fluids and Structures* 57 (2015), pp. 298–313. ISSN: 0889-9746. DOI: `10.1016/j.jfluidstructs.2015.06.011`.

[7] L. L. Chen, H. Lian, Z. Liu, H. B. Chen, E. Atroshchenko, and S. P. A. Bordas. "Structural shape optimization of three dimensional acoustic problems with isogeometric boundary element methods". In: *Computer Methods in Applied Mechanics and Engineering* 355 (2019), pp. 926–951. ISSN: 0045-7825. DOI: `10.1016/j.cma.2019.06.012`.

[8] P. Kliewe, A. Laurain, and K. Schmidt. "Shape optimization in acoustic–structure interaction". In: *Engineering Computations* 39.1 (Jan. 2022), pp. 172–200. ISSN: 0264-4401. DOI: `10.1108/EC-07-2021-0379`.

[9] Gene Hou, Jin Wang, and Anita Layton. "Numerical Methods for Fluid-Structure Interaction — A Review". In: *Communications in Computational Physics* 12.2 (2012), pp. 337–377. DOI: `10.4208/cicp.291210.290411s`.

[10] G. Sandberg, P.-A. Wernberg, and P. Davidsson. "Fundamentals of Fluid-Structure Interaction". In: June 2009, pp. 23–101. ISBN: 978-3-211-89650-1. DOI: `10.1007/978-3-211-89651-8_2`.

[11] H. J. Bungartz and M. Schäfer. *Fluid-Structure Interaction: Modelling, Simulation, Optimisation.* Lecture Notes in Computational Science and Engineering. Springer Berlin Heidelberg, 2007. ISBN: 9783540345961. URL: `https://books.google.com.gi/books?id=-6NSKaCcGXkC`.

[12] S. Marburg and B. Nolte. *Computational Acoustics of Noise Propagation in Fluids - Finite and Boundary Element Methods.* Mar. 2008. ISBN: 978-3-540-77447-1. DOI: `10.1007/978-3-540-77448-8_18`.

[13] T. Richter. *Fluid-structure Interactions: Models, Analysis and Finite Elements.* Lecture Notes in Computational Science and Engineering. Springer International Publishing, 2017.

[14] G. Sandberg and R. Ohayon. *Computational Aspects of Structural Acoustics and Vibration*. Vol. 505. Jan. 2009. ISBN: 978-3-211-89650-1. DOI: `10.1007/978-3-211-89651-8`.

[15] W. Zhao, L. Chen, H. Chen, and S. Marburg. "Topology optimization of exterior acoustic-structure interaction systems using the coupled FEM-BEM method". In: *International Journal for Numerical Methods in Engineering* 119.5 (2019), pp. 404–431. DOI: `10.1002/nme.6055`.

[16] G. H. Yoon. "Unified Analysis with Mixed Finite Element Formulation for Acoustic-Porous-Structure Multiphysics System". In: *Journal of Computational Acoustics* 23.01 (2015), p. 1550002. DOI: `10.1142/S0218396X15500022`.

[17] S. Zörner and M. Kaltenbacher. "Fluid–structure–acoustic interaction, Algorithms and implementation using the finite element method". In: *V European Conference on Computational Fluid Dynamics, ECCOMAS CFD 2010*. Lisbon, Portugal, 2010, pp. 879–888.

[18] M. R. Dörfel and B." Simeon. "Analysis and Acceleration of a Fluid-Structure Interaction Coupling Scheme". In: *Numerical Mathematics and Advanced Applications 2009*. Ed. by P. Kreiss G. and Lötstedt, A. Målqvist, and M. Neytcheva. Berlin, Heidelberg: Springer Berlin Heidelberg, 2010, pp. 307–315. ISBN: 978-3-642-11795-4.

[19] F. Hecht. "New development in FreeFem++". In: *J. Numer. Math.* 20.3-4 (2012), pp. 251–265. ISSN: 1570-2820. URL: `https://freefem.org`.

[20] A. Bermúdez, P. Gamallo, L. Hervella–Nieto, R. Rodríguez, and D. Santamarina. "Fluid–Structure Acoustic Interaction". In: *Computational Acoustics of Noise Propagation in Fluids - Finite and Boundary Element Methods*. Ed. by S. Marburg and B. Nolte. Berlin, Heidelberg: Springer Berlin Heidelberg, 2008, pp. 253–286. DOI: `10.1007/978-3-540-77448-8_10`.

[21] H. J. P. Morand and R. Ohayon. *Fluid-Structure Interaction: Applied Numerical Methods*. Wiley-Masson Series Research in Applied Mathematics. Wiley, 1995.

PAPER III

Feedforward Neural Network for Frequency Response[1]

Klas Pettersson

Chalmers University of Technology, Sweden

Andrei Karzhou

UiT The Arctic University of Norway

Irina Pettersson

Chalmers University of Technology and Gothenburg University, Sweden

Abstract

The Helmholtz equation has been used for modeling the sound pressure field under a harmonic load. Computing harmonic sound pressure fields by means of solving Helmholtz equation can quickly become unfeasible if one wants to study many different geometries for ranges of frequencies. We propose a machine learning approach, namely a feedforward dense neural network, for computing the average sound pressure over a frequency range. The data is generated with finite elements, by numerically computing the response of the average sound pressure, by an eigenmode decomposition of the pressure. We analyze the accuracy of the approximation and determine how much training data is needed in order to reach a certain accuracy in the predictions of the average pressure response.

Keywords: Frequency response, sound pressure, Helmholtz equation, machine learning, feedforward dense neural network.

III.1   Introduction

Modeling such acoustics problems as building acoustics, vehicle interior noise problems, noise reduction, insertion and transmission loss, often requires computing average sound pressure, which in its turn is based on the computation of natural frequencies and the response to a dynamic excitation. There are two main approaches to modeling of acoustic systems under small frequency excitation: To model acoustics in the time domain or in the frequency domain. Sound waves, as vibrations, are described by a time dependent wave equation, which can be reduced to a time independent Helmholtz equation by assuming harmonic dependence on time [1]. If the geometry of the domain is complex, it is decomposed into subdomains, in each subdomain the analysis is performed. Given an acoustic system, one needs to solve the Helmholtz equation repeatedly for given frequency, which might be very costly. In addition, the most important and costly part in a FEM-analysis is the computation of eigenfrequencies and eigenfunctions in each subdomain. We propose a feedforward dense neural network (multi-layer perceptron) for computing the average sound pressure in cylindrical cavities with polygonal boundary.

Some motivation for studying the average pressure response over a range of frequencies can be found in engineering applications. For example, standardized frequency ranges can be found in the ISO standard [2].

For an overview of deep learning in neural networks, we refer to [3] and for overview of basic mathematical principles to [4, 5] and literature therein. Application of machine learning methods in acoustics has made significant progress in recent years. A comprehensive overview of the recent advances is given in [6]. The frequency response problem, being the basis in modeling of acoustic problems, is not specifically addressed in [6], as any other combination of machine learning techniques and modeling with partial differential equations (PDEs).

There are many work devoted to solving PDEs, forward as well as inverse problems, by means of machine learning techniques. We mention just some of them. The work [7] propose an algorithm to solve initial and boundary value problems using artificial neural networks. The gradient descent is used for optimization. In [8] the authors propose an algorithm to solve an inverse problem associated with the calculation of the Dirichlet eigenvalues of the anisotropic Laplace operator. The finite elements are used to generate the training data. The main goal is to characterize the material properties (coefficient matrix) through the eigenvalues.

In [9] the authors approximate solutions to high-dimensional PDEs with a deep neural network which is trained to satisfy the differential operator, initial condition, and boundary conditions. The convergence of the neural network to the solution of a PDE is proved. In contrast to [7], the algorithm in [9] is mesh-free.

In [10] a partially learned approach is employed for the solution of ill-posed inverse problems. The paper contains also a good literature overview for inverse problems. In [11] the authors propose deep feedforward artificial neural networks (mesh-free) to approximate solutions to partial differential equations in complex geometries. The paper [12] focuses on the nonlinear partial differential equations. Some other network inspired approaches in the study of PDEs are [13, 14, 15, 16].

In [17] the authors propose an iterative solver for the Helmholtz equation which combines traditional Krylov-based solvers with machine learning. The result is a reduced computational complexity.

In the present paper we use feedforward fully connected neural networks with the ReLU activation function in hidden layers in order to approximate the average pressure function originated in frequency response problems. We choose to use three hidden layers, 128 nodes in each, and ADAM optimizer. The step size in the gradient descent is scheduled to have polynomial decay. A more detail description of the neural network is provided in Section III.4.

The feedforward neural network is designed to directly learn the average pressure, in contrast to the works cited above, where the neural networks are tailored to predict the coefficients of the inverse problem or solutions to PDEs.

It is known that a neural network can approximate any continuous function to an arbitrary accuracy [18]. We focus on the frequency response problem (low frequencies) in two-dimensional polygonal cylinders. Assuming harmonic load on a part on the boundary, we arrive at a time independent Helmholtz equation for the sound pressure. The mean-value of the average pressure over a given frequency range is an important quantity for characterizing the sound attenuation, insertion and transmission losses. The numerical solution of this problems implies solving the Helmholtz equation for many different values of the spectral parameter, which is a costly problem. Besides, the pressure function is singular near the eigenvalues of the Laplace equation, and the standard quadrature schemes cannot be applied in order to compute the average Ψ over a frequency range (see Section III.2.3 and Figure III.2.3(b) for the explanation). Instead, we represent the average pressure Ψ (objective function) in terms of a Hilbert basis, the eigenmodes of the Laplace operator. We generate data sets containing around 700 000 randomly generated points which define polygonal cylinders and the corresponding objective functions Ψ computed using finite elements. A feedforward neural network with five input nodes (coordinates defining cylinders), three hidden layers and one output node (scalar objective function Ψ_{ml}) is then constructed to approximate the objective function.

We analyze the performance of the model, and show the dependency of the mean squared error (MSE) on the training set size. Moreover, we analyze how many samples is needed to reach a desired approximation accuracy. For example, for polygonal cylinders defined by five randomly generated points, on average over 95% are predicted with mean absolute error less than 0.01 when the training set contains 200 000 data points. The data used for machine learning in this paper is available at [19].

The sound pressure as a function of frequency is nonlinear, and thus the linear regression methods perform poorly. In Section III.6, we show the results of the approximation of the objective function by means of linear regression vs. feedforward fully connected neural network with ReLU nonlinearity. The proposed method performs much better, as expected.

For machine learning we have used Tensorflow [20], and the stochastic gradient descent optimizer ADAM [21]. For the numerical computation of the average

PAPER III. ML FOR FREQUENCY RESPONSE

pressure we used primarily the SLEPc [22], with user interfaces and numerical PDE tools FreeFem [23] and FEniCS [24] to the standard numerical packages.

Our method can be applied for analyzing frequency response in elastic bodies and fluid-structure interaction problems. In three-dimensional case the frequency response problems become computationally heavy, and the effectiveness of the stochastic gradient descent gives some hope for significant reduction of data needed for training.

The rest of this paper is organized as follows. In Section III.2, the numerical method for computing the average sound pressure response is described. Using the numerical method, the data sets for polygonal cylinders are generated and the data sets are described in Section III.3. In Section III.4, we specify the feedforward dense neural network and the choices of for the training procedure. The model obtained after training is evaluated in Section III.5, and compared to a linear model in Section III.6.

III.2   Frequency response problem and average pressure

Assume that a domain Ω is occupied by a inviscid, homogeneous, compressible fluid (liquid or gas). There are several options for choosing a primary variable for small amplitude vibrations: fluid displacement, acoustic pressure or fluid velocity potential. We are going to use a description in terms of the scalar pressure function P. Let c be the speed of sound in the fluid, and ρ be the mass density of the fluid, both assumed not to depend on the pressure P. The equation of motion without taking in account the damping is the wave equation for the acoustic pressure [1]:

$$\rho\frac{\partial^2 P(t,x)}{\partial t^2} - c^2 \Delta P(t,x) = F(t,x). \tag{III.2.1}$$

Here F is the applied load. The solution of the last equation is by linearity a sum of a particular solution to a non-homogeneous equation (forced motion) and the general solution of the homogeneous equation (natural motion). If the excitation is harmonic $F(t,x) = f(x)\cos(\omega t) = f(x)\Re e^{i\omega t}$, the forced motion is called the steady-state response. The real-valued pressure together with the phase angle is then called the dynamic frequency response of the system [25]. To eliminate the time dependency in the wave equation, we substitute $P(t,x) = \Re(p(x)e^{i\omega t})$ into it and obtain a time independent Helmholtz equation for the amplitude p:

$$-\Delta p(x) - \frac{\omega^2 \rho}{c^2}p(x) = f(x).$$

If the acoustic medium is contained in a bounded domain Ω, we will need to impose boundary conditions on the boundary $\partial\Omega$. We will impose a harmonic load $\cos(\omega t)$ on the part of the boundary Γ_D, which results in the non-homogeneous Dirichlet boundary condition $p = 1$. On the rest of the boundary $\Gamma_N = \partial\Omega \setminus \Gamma_D$ is assumed to be sound hard (zero-flux condition). The problem in the frequency domain takes

the form

$$-\Delta p - \frac{\omega^2 \rho}{c^2} p = 0 \quad \text{in } \Omega,$$
$$p = 1 \quad \text{on } \Gamma_D, \tag{III.2.2}$$
$$\nabla p \cdot \nu = 0 \quad \text{on } \Gamma_N,$$

where ν is the exterior unit normal.

We are going to solve (III.2.2) analytically for cylinders Ω with constant and non-constant cross-section. We will obtain expressions for the mean-value of the solution to (III.2.2) with respect to the spatial variable $\langle p \rangle = |\Omega|^{-1} \int_\Omega p \, dx$, and its average with respect to the spectral parameter

$$\lambda = \frac{\omega^2 \rho}{c^2}.$$

The domain may be an open set in Euclidean space $\mathbf{R}^n$. In what follows, we will work with Ω a bounded Lipschitz domain in $\mathbf{R}^2$, that is a bounded open connected subset of $\mathbf{R}^2$ with Lipschitz continuous boundary. Specifically, Ω will be a finite cylinder with polygonal boundary.

We will in the sequel assume the quantities and variables to be scaled in such a way they are nondimensionalized, and thereby also suppress units from both manipulations and figures.

III.2.1   Uniform cylinders

We start with cylinders with constant cross-section, where one can find explicit formulas for eigenfunctions and eigenvalues for the Laplace operator and therefore solve the frequency response problem analytically.

Let us denote $\Omega = (0, 1) \times (-a, a)$ for $r_{\min} \leq a \leq r_{\max}$ a uniform cylinder. The boundary of Ω consists of two parts, and we denote $\Gamma_D = \{(x_1, x_2) : x_1 = 0\}$ (the part where a Dirichlet boundary condition will be imposed) and $\Gamma_N = \partial\Omega \setminus \Gamma_D$ (with a Neumann boundary condition). Consider the frequency response problem (III.2.2) in Ω. By the Fredholm alternative, there exists a unique solution $p_\lambda \in H^1(\Omega)$ to (III.2.2) if and only if λ is not an eigenvalue of the Laplace operator in the cylinder:

$$-\Delta\psi = \lambda\psi \quad \text{in } \Omega,$$
$$\psi = 0 \quad \text{on } \Gamma_D, \tag{III.2.3}$$
$$\nabla\psi \cdot \nu = 0 \quad \text{on } \Gamma_N.$$

By the Hilbert-Schmidt and the Riesz-Schauder theorems, the spectrum of (III.2.3) is positive, discrete, countably infinite, and each eigenvalue of finite multiplicity,

$$0 < \lambda_1 < \lambda_2 \leq \lambda_3 \leq \cdots \leq \lambda_n \to \infty, \quad n \to \infty.$$

Moreover, the eigenfunctions ψ_i form an orthonormal basis under a proper normalization. By separation of variables, choosing a convenient enumeration, the eigenvalues $\lambda_{i,k,l}$ to (III.2.3) are given by

$$\lambda_{i,k,l} = \mu_k + \eta_{i,l}, \quad i = 1, 2, \quad k, l = 0, 1, \ldots, \tag{III.2.4}$$

where

$$\mu_k = \frac{(2k+1)^2 \pi^2}{4}, \quad k = 0, 1, \ldots, \tag{III.2.5}$$

$$\eta_{1,l} = \frac{l^2 \pi^2}{a^2}, \quad \eta_{2,l} = \frac{(2l+1)^2 \pi^2}{4a^2}, \quad l = 0, 1, \ldots. \tag{III.2.6}$$

The sequences $\mu_k > 0$ and $\eta_{i,l} \geq 0$ are the Dirichlet-Neumann eigenvalues of the Laplace operator on $(0, 1)$, and the Neumann eigenvalues of the Laplace operator on $(-a, a)$, respectively. The eigenfunctions $\psi_{i,k,l}$ to (III.2.3) corresponding to the eigenvalues $\lambda_{i,k,l}$ are

$$\psi_{1,k,l} = a_{1,k,l} \sin(\sqrt{\mu_k} x_1) \cos(\sqrt{\eta_{1,l}} x_2), \tag{III.2.7}$$
$$\psi_{2,k,l} = a_{2,k,l} \sin(\sqrt{\mu_k} x_1) \sin(\sqrt{\eta_{2,l}} x_2),$$

where $a_{i,k,l}$ are $L^2(\Omega)$ normalization factors defined by

$$\int_\Omega \psi_{i,k,l} \psi_{j,p,q} \, dx = \begin{cases} 1 & \text{if } (i, k, l) = (j, p, q), \\ 0 & \text{otherwise.} \end{cases}$$

Explicitly, $a_{1,k,0} = \sqrt{1/a}$, and otherwise $a_{i,k,l} = \sqrt{2/a}$.

Let $\lambda \in \mathbf{R}$ not be an eigenvalue to (III.2.3). Then the method of separation of variables gives a solution p_λ to (III.2.2) in the case of uniform cylinder:

$$p_\lambda = 1 + \sum_{k=0}^\infty \frac{\lambda}{\mu_k - \lambda} \frac{2}{\sqrt{\mu_k}} \sin(\sqrt{\mu_k} x_1)$$
$$= \cos(\sqrt{\lambda} x_1) + \tan(\sqrt{\lambda}) \sin(\sqrt{\lambda} x_1). \tag{III.2.8}$$

Remark that p_λ is constant in the x_2-direction for this particular choice of harmonic load $p(0, x_2) = 1$.

When analyzing the acoustic response, one could be interested in the average pressure defined for a frequency sweep, namely the average of p_λ with respect to x and λ. Let us first compute the average pressure $\langle p_\lambda \rangle$ with respect to x:

$$\langle p_\lambda \rangle = \frac{1}{|\Omega|} \int_\Omega p_\lambda \, dx = \begin{cases} \dfrac{\tan(\sqrt{\lambda})}{\sqrt{\lambda}} & \text{if } \lambda > 0, \\ 1 & \text{if } \lambda = 0. \end{cases} \tag{III.2.9}$$

The pressure p_λ and its mean-value with respect to the space variable as a function of λ is shown in Figure III.2.1.

The form of the response $\langle p_\lambda \rangle$ in (III.2.9) indicates that it could be challenging to numerically evaluate an integral of $\langle p_\lambda \rangle$ in λ over an interval $(\lambda_{\min}, \lambda_{\max})$ that contains a pole, because the computation of the Cauchy principal value of the integral

requires both the location of the poles and their orders. For the uniform cylinder we obtain the following explicit formula for the objective function:

$$
\begin{aligned}
\Psi &= \frac{1}{\lambda_{\max} - \lambda_{\min}} \, \text{p.v.} \int_{\lambda_{\min}}^{\lambda_{\max}} \langle p_\lambda \rangle \, d\lambda \\
&= \frac{1}{\lambda_{\max} - \lambda_{\min}} \, \text{p.v.} \int_{\lambda_{\min}}^{\lambda_{\max}} \frac{\tan(\sqrt{\lambda})}{\sqrt{\lambda}} \, d\lambda \\
&= \frac{2}{\lambda_{\max} - \lambda_{\min}} \log \left| \frac{\cos(\sqrt{\lambda_{\min}})}{\cos(\sqrt{\lambda_{\max}})} \right|,
\end{aligned}
\tag{III.2.10}
$$

which is defined as long as both $\lambda_{\min}, \lambda_{\max}$ are not eigenvalues of (III.2.3). More precisely, if $\lambda = \lambda_{i,k,l}$ is an eigenvalue to (III.2.3), the response p_λ exists if and only if $\int_\Omega \psi_{i,k,l} \, dx = 0$ for all eigenfunctions corresponding to $\lambda_{i,k,l}$, by the Fredholm alternative. One notes that $\int_\Omega \psi_{1,k,l} \, dx = 0$ for $l \geq 1$, and $\int_\Omega \psi_{2,k,l} \, dx = 0$ for $l \geq 0$. Thus for $\lambda = \lambda_{1,k,l}$ with $l \geq 1$, and for $\lambda = \lambda_{2,k,l}$ with $l \geq 0$, the solution p_λ is unique modulo a linear combination of the corresponding eigenfunctions. Such eigenfunctions do not contribute to the mean-value $\langle p_\lambda \rangle$ and therefore also not to Ψ. It follows that (III.2.9) holds for $\lambda \neq \mu_k$, and (III.2.10) holds for $\lambda_{\min}, \lambda_{\max} \neq \mu_k$.
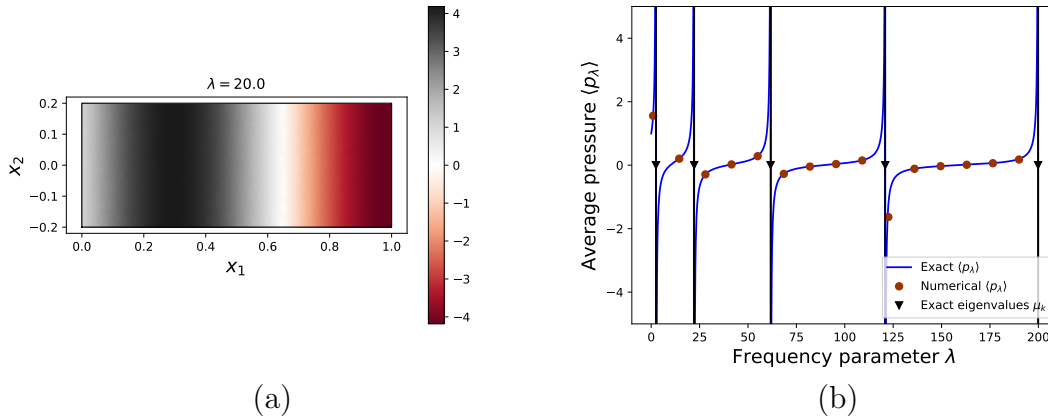
Figure III.2.1: The response p_λ for $\lambda = 20$ (a), and the average pressure $\langle p_\lambda \rangle$ (b) for a uniform cylinder.

III.2.2 Cylinders with varying cross-section

In this section we will show how a Hilbert basis can be used to compute the average in λ of $\langle p_\lambda \rangle$ (the objective function) in the case when cylinders have varying cross-section. The explicit formulas for the eigenvalues and eigenfunctions like (III.2.4)–(III.2.7) are not available any more, and we will use the finite elements to compute the eigenpairs of the Laplace operator.

Let p, as before, for a given λ solve the frequency response problem

$$\begin{aligned}
-\Delta p - \lambda p &= 0 && \text{in } \Omega, \\
p &= 1 && \text{on } \Gamma_D, \\
\nabla p \cdot \nu &= 0 && \text{on } \Gamma_N.
\end{aligned} \tag{III.2.11}$$

The cylinder Ω is not uniform any more, and can be described by $\Omega = \{x = (x_1, x_2) : x_1 \in (0,1), x_2 \in I(x_1)\}$, where $I(x_1) = (-a(x_1), a(x_1))$ is an interval such that $r_{\min} \le a(x_1) \le r_{\max}$.

We will represent the solution p_λ of (III.2.11) in terms of the eigenpairs of the Laplace operator

$$\begin{aligned}
-\Delta \psi &= \kappa \psi && \text{in } \Omega, \\
\psi &= 0 && \text{on } \Gamma_D, \\
\nabla \psi \cdot \nu &= 0 && \text{on } \Gamma_N.
\end{aligned} \tag{III.2.12}$$

As before, the spectrum $0 < \kappa_1 < \kappa_2 \le \cdots \le \kappa_j \to \infty$ is discrete, and the eigenfunctions ψ_i form a Hilbert basis in $L^2(\Omega)$, and we assume that they are orthonormalized by $\int_\Omega \psi_i \psi_j \, dx = \delta_{ij}$. Writing $p_\lambda = 1 + \sum_{i=1}^\infty \beta_i \psi_i$ and substituting into (III.2.11) one gets

$$p_\lambda(x) = 1 + |\Omega| \sum_{i=1}^\infty \frac{\lambda}{\kappa_i - \lambda} \langle \psi_i \rangle \psi_i(x), \quad \langle \psi_i \rangle = \frac{1}{|\Omega|} \int_\Omega \psi_i \, dx. \tag{III.2.13}$$

The mean value of p_λ in Ω is

$$\begin{aligned}
\langle p_\lambda \rangle &= \frac{1}{|\Omega|} \int_\Omega p_\lambda \, dx = 1 + |\Omega| \sum_{i=1}^\infty \frac{\lambda}{\kappa_i - \lambda} \langle \psi_i \rangle^2 \\
&= 1 - |\Omega| \sum_{i=1}^\infty \langle \psi_i \rangle^2 + |\Omega| \sum_{i=1}^\infty \frac{\lambda}{\kappa_i - \lambda} \langle \psi_i \rangle^2.
\end{aligned} \tag{III.2.14}$$

The pressure p_λ in a polygonal cylinder, and its mean-value $\langle p_\lambda \rangle$ with respect to the space variable as a function of λ is shown in Figure III.2.2.

Let us now average (III.2.14) over $(\lambda_{\min}, \lambda_{\max})$ to get the objective function:

$$\begin{aligned}
\Psi &= \frac{1}{\lambda_{\max} - \lambda_{\min}} \text{p.v.} \int_{\lambda_{\min}}^{\lambda_{\max}} \langle p_\lambda \rangle \, d\lambda \\
&= 1 + |\Omega| \sum_{i=1}^\infty \left[\frac{\kappa_i}{\lambda_{\max} - \lambda_{\min}} \log \left| \frac{\kappa_i - \lambda_{\min}}{\lambda_{\max} - \kappa_i} \right| - 1 \right] \langle \psi_i \rangle^2. \tag{III.2.15}
\end{aligned}$$

As we have seen above, for the case of a uniform cylinder, the right hand side of (III.2.15) sums up to (III.2.10).

III.2.3   Numerical computation of the average pressure response

In order to compute the objective function Ψ (III.2.15) in the case of a non-uniform cylinder, we compute the eigenpairs (κ_j, ψ_j) of (III.2.12) using the first order Lagrange finite elements.

The variational formulation for (III.2.12) reads: Find $\kappa \in \mathbf{R}$ and $\psi \in H^1(\Omega)\backslash\{0\}$, $\psi = 0$ on Γ_D, such that

$$\int_\Omega \nabla\psi \cdot \nabla v \, dx = \kappa \int_\Omega \psi \, v \, dx, \qquad \text{(III.2.16)}$$

for any $v \in H^1(\Omega)$, $v = 0$ on Γ_D. For a triangulation mesh $\mathcal{T}_h$ of Ω, we consider Lagrange triangular finite elements of order 1 as a basis for the finite-dimensional subspace

$$V_{0h} = \left\{ v \in C(\overline{\Omega}) : v\big|_K \in \mathbb{P}_1 \text{ for all } K \in \mathcal{T}_h, \; v = 0 \text{ on } \Gamma_D \right\}. \qquad \text{(III.2.17)}$$

The internal approximation for the variational formulation (III.2.16) is

$$\int_\Omega \nabla\psi_h \cdot \nabla v_h \, dx = \kappa_h \int_\Omega \psi_h \, v_h \, dx, \qquad \text{(III.2.18)}$$

for all $v_h \in V_{0h}$. The eigenvalues of (III.2.18) form a finite increasing sequence

$$0 < \kappa_{h,1} \leq \kappa_{h,2} \leq \cdots \leq \kappa_{h,n_{dl}}, \quad \text{with } n_{dl} = \dim V_{0h},$$

and there exists a basis in V_{0h} consisting of corresponding eigenfunctions which is orthonormal in $L^2(\Omega)$. A proof of this statement can be found in [26, Ch. 7.4].

We look for a solution of (III.2.18) in the form $\psi_h(x) = \sum_{i=1}^{n_{dl}} U_i^h \phi_i(x)$, where $(\phi_i)_{1 \leq i \leq n_{dl}}$ is the basis in V_{0h}. Introducing the mass matrix $\mathcal{M}_h$ and the stiffness matrix $\mathcal{K}_h$,

$$(\mathcal{M}_h)_{ij} = \int_\Omega \phi_i \, \phi_j \, dx, \quad (\mathcal{K}_h)_{ij} = \int_\Omega \nabla\phi_i \cdot \nabla\phi_j \, dx, \quad 1 \leq i, j \leq n_{dl}, \qquad \text{(III.2.19)}$$
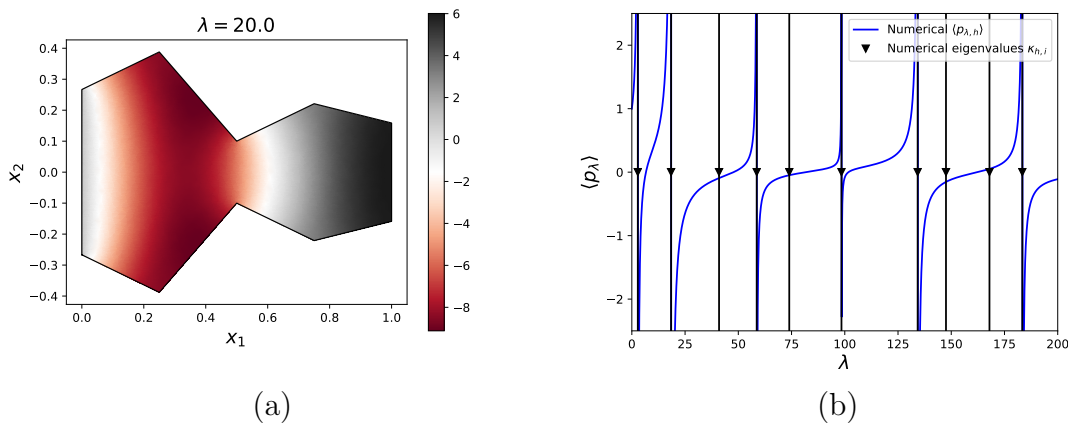

(a)   (b)

Figure III.2.2: The response p_λ for $\lambda = 20$ (a), and the average pressure $\langle p_\lambda \rangle$ (b) for the polygonal cylinder shown in Figure III.3.1(b). The vertical lines in (b) indicate the poles.

we get the following discrete finite-dimensional spectral matrix problem:

$$\mathcal{K}_h\psi_h = \kappa_h\mathcal{M}_h\psi_h. \tag{III.2.20}$$

The matrices $\mathcal{M}_h$ and $\mathcal{K}_h$ are symmetric and positive definite.

The error estimate for the eigenvalues corresponding to eigenfunctions in $H^2(\Omega)$, which is for instance the case if Ω is convex in $\mathbf{R}^2$, is

$$|\kappa_i - \kappa_{h,i}| \leq C_i h^2,$$

where C_i does not depend on $h = \max\{\text{diam}(K) : K \in \mathcal{T}_h\}$, but does depend on the number of the eigenvalue, that is why is it important to take a sufficiently fine mesh to get a good approximation for κ_i with large i (see e.g. [26]). More precisely, if κ_i is an eigenvalue with eigenfunctions in $H^{k+1}(\Omega)$, $\Omega \subset \mathbf{R}^n$, and $2(k+1) > n$, then $|\kappa_i - \kappa_{h,i}| \leq C_i h^{2k}$.

In the numerical method, we truncate the series in (III.2.15) at $i = N$,

$$\Psi_h = 1 + |\Omega| \sum_{i=1}^{N} \left[\frac{\kappa_{h,i}}{\lambda_{\max} - \lambda_{\min}} \log \left| \frac{\kappa_{h,i} - \lambda_{\min}}{\lambda_{\max} - \kappa_{h,i}} \right| - 1 \right] \langle \psi_{h,i} \rangle^2, \tag{III.2.21}$$

where N is chosen such that the sum ranges over the eigenvalues up to at least $10\lambda_{\max}$, and the number of degrees of freedom $\dim V_{0h}$ is at least 10 times greater than the greatest eigenvalue $\kappa_{h,N}$ used in the computation. This ensures that the eigenvalues $\kappa_{h,i}$ and the eigenfunctions $\psi_{h,i}$ of the discrete eigenvalue problem (III.2.20) are correct approximations to the exact eigenvalues $\kappa_{h,i}$ and exact eigenfunctions $\psi_{h,i}$ of (III.2.16).

In order to evaluate the accuracy of the method, in the case of uniform cylinders, we can compare the exact objective function (III.2.10) (the blue curve) with its numerical approximation (III.2.21) (the dots). The result is presented in Figure III.2.3(a). The peaks of the objective function are located at the eigenvalues μ_k since p_λ has poles at these points. The graph is valid for a uniform cylinder of arbitrary radius, because the pressure does not depend on the transverse variable. It is important to note that numerical integration by means of the trapezoidal rule of the exact response $\langle p_\lambda \rangle$ given by (III.2.9) with respect to λ does not give a good approximation for Ψ. In Figure III.2.3(b) one can see that the numerical integration fails after the first eigenvalue. The reason for this is the singular behavior of p_λ near the eigenvalues μ_k.

In the case of non-uniform cylinders we do not have any explicit formulas any more, so we investigate numerically the rate of convergence for the approximation of Ψ by Ψ_h. For the sake of completeness, we present the convergence rate for both uniform and non-uniform cylinders.

In Figure III.2.5(a), one can see a clear quadratic decay of $|\Psi - \Psi_h|$ with respect to mesh size h for uniform cylinders (convex). The objective function Ψ_h (III.2.21) is computed as the average over $(0, \lambda_{\max})$ for several $\lambda_{\max}$ and for uniform mesh refinements. The quadratic decay of the error with respect to the mesh size h is expected for first order polynomial approximations of a smooth function in $L^2(\Omega)$. In $\mathbf{R}^2$, the number of degrees of freedom $\dim V_{0h}$ grows as h^{-2} for uniform mesh
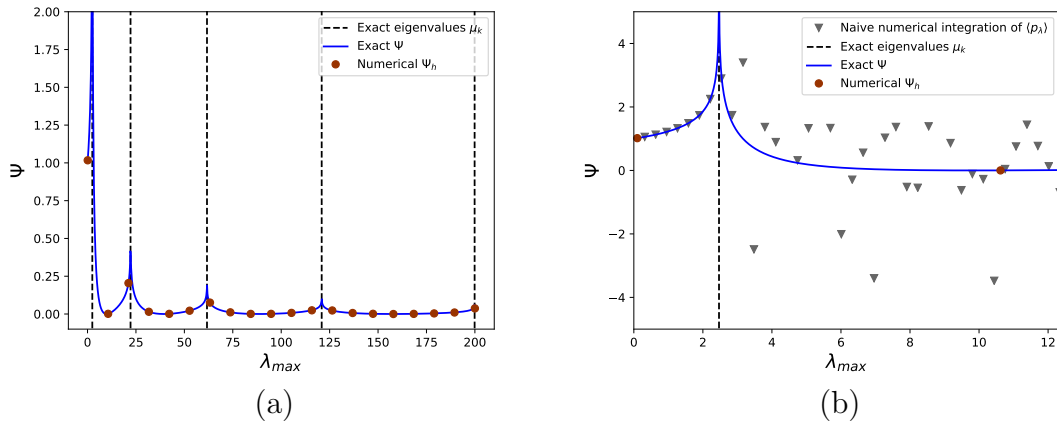
Figure III.2.3: Objective function in a uniform cylinder for intervals $(0, \lambda_{\max})$ with $\lambda_{\max}$ on the horizontal axis.
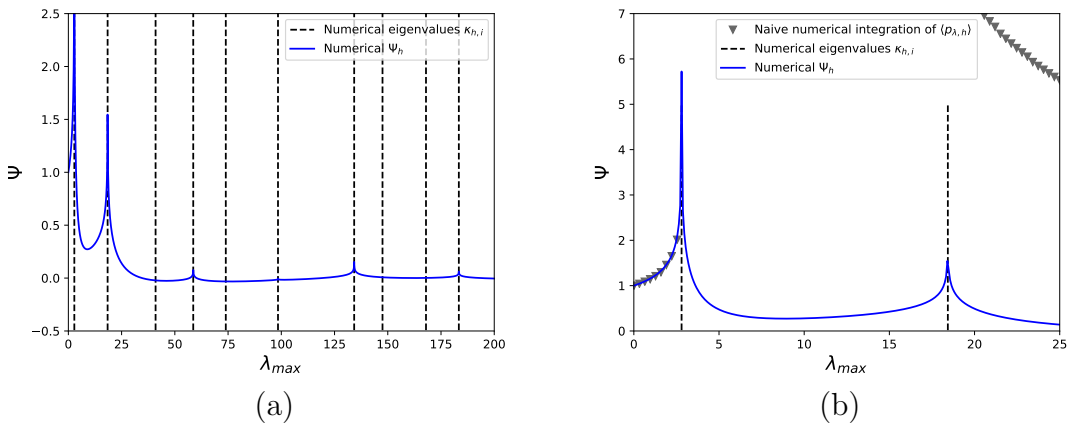

Figure III.2.4: The objective function in a non-uniform cylinder in Figure III.3.1(b) for intervals $(0, \lambda_{\max})$ with $\lambda_{\max}$ on the horizontal axis.

refinement, which suggests an expected rate of decay $(\dim V_{0h})^{-1}$ for non-degenerate uniform mesh refinement.

In Figure III.2.5(b), we present the rate of convergence while refining the mesh for several cylinders with polygonal boundary. We observe a subquadratic convergence rate with respect to the mesh size.
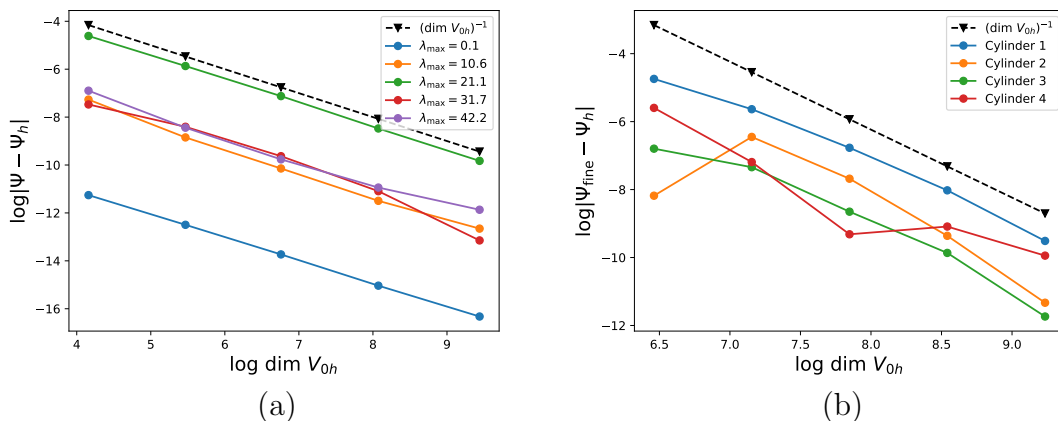
(a)   (b)

Figure III.2.5: Rate of convergence of the finite element approximation of the objective function Ψ. (a) The absolute error for a uniform cylinder. (b) The estimated rate of convergence for four samples of non-uniform cylinders, and fixed $\lambda_{\max} = 60$.

III.2.4 Shape derivative of the average pressure response

In this section we compute the derivative Ψ' of the objective function

$$\Psi = \frac{1}{\lambda_{\max} - \lambda_{\min}} \int_{\lambda_{\min}}^{\lambda_{\max}} \langle p_\lambda \rangle \, d\lambda, \tag{III.2.22}$$

with respect to certain variations of the convex cylindrical domains Ω in $\mathbf{R}^2$. The purpose of this is twofold. One, it ascertains that the accuracy of our trained model on Lipschitz domains that are close in a precise sense to certain polygonal domains in our evaluation sets. Two, it enables for some boosting of the training sets that are otherwise somewhat costly to generate by the method we have chosen.

For a vector field V and a parameter t, we introduce the bi-Lipschitz transformation $T(x) = x + tV(x)$. We denote by Ω_t the image of Ω under T. Let Ψ_t be the value of (III.2.22) for the domain Ω_t, $\Psi = \Psi_0$. With Ψ'_0, the derivative of Ψ at $t = 0$, Ψ is linearized as

$$\Psi_t = \Psi_0 + t\Psi'_0 + o(t),$$

as t tends to zero.

In this section we employ standard techniques of domain variations in the theory of elliptic equations. We refer to [27], [28], and [29] for expositions.

Lemma III.2.1. *Let $V \in W^{1,\infty}(\Omega)$ be a solenoidal vector field on convex Ω. Suppose that the interval $[\lambda_{\min}, \lambda_{\max}]$ does not contain any eigenvalue κ_i for which $\langle \psi_i \rangle \neq 0$. Then the shape derivative of the objective function (III.2.22) is given by*

$$\Psi' = \lim_{t \to 0} \frac{\Psi_t - \Psi_0}{t} = \sum_{i,j=1}^{\infty} c_{i,j} \langle \nabla V \nabla \psi_i \cdot \nabla \psi_j \rangle \langle \psi_i \rangle \langle \psi_j \rangle,$$

where for $\kappa_i = \kappa_j$,

$$c_{i,j} = \frac{2|\Omega|^2}{\lambda_{\max} - \lambda_{\min}} \left[\log \left| \frac{\lambda_{\max} - \kappa_i}{\kappa_i - \lambda_{\min}} \right| - \frac{\kappa_i}{\lambda_{\max} - \kappa_i} - \frac{\kappa_i}{\kappa_i - \lambda_{\min}} \right],$$

and for $\kappa_i \neq \kappa_j$,

$$c_{i,j} = \frac{2|\Omega|^2}{\lambda_{\max} - \lambda_{\min}} \left[\frac{\kappa_i}{\kappa_i - \kappa_j} \log \left| \frac{\lambda_{\max} - \kappa_i}{\kappa_i - \lambda_{\min}} \right| - \frac{\kappa_j}{\kappa_i - \kappa_j} \log \left| \frac{\lambda_{\max} - \kappa_j}{\kappa_j - \lambda_{\min}} \right| \right].$$

Proof. One notes that by elliptic regularity $p_\lambda \in H^2(\Omega)$. Denote by $\dot{p}_\lambda \in H^1(\Omega, \Gamma_D)$ the material derivative of p_λ: $\dot{p}_\lambda = p'_\lambda + \nabla p_\lambda \cdot V$, where $p'_\lambda \in H^1(\Omega)$ denotes the shape derivative of the response with respect to V. By the regularity of V, there exist a Sobolev extension, and thereby the shape derivatives with respect to V of the response and the associated linear and bilinear forms exist in the sense of Fréchet with respect to the parameter t.

A direct computation of the Gateaux derivative gives

$$\Psi' = \frac{1}{\lambda_{\max} - \lambda_{\min}} \int_{\lambda_{\min}}^{\lambda_{\max}} \langle p_\lambda \rangle' \, d\lambda$$

$$= \frac{1}{\lambda_{\max} - \lambda_{\min}} \int_{\lambda_{\min}}^{\lambda_{\max}} \left(\langle \dot{p}_\lambda \rangle + \langle p_\lambda \mathrm{div} V \rangle - \langle p_\lambda \rangle \langle \mathrm{div} V \rangle \right) d\lambda.$$

To compute $\langle \dot{p}_\lambda \rangle$, we note that $\dot{p}_\lambda$ is an admissible test function in the variational form of the equation for p_λ:

$$\int_\Omega \nabla(p_\lambda - 1) \cdot \nabla v \, dx - \lambda \int_\Omega (p_\lambda - 1) v \, dx = \lambda \int_\Omega v \, dx.$$

Therefore,

$$\lambda \int_\Omega \dot{p}_\lambda \, dx = \int_\Omega \nabla(p_\lambda - 1) \cdot \nabla \dot{p}_\lambda \, dx - \lambda \int_\Omega (p_\lambda - 1) \dot{p}_\lambda \, dx$$

$$= 2 \int_\Omega \nabla(\nabla p_\lambda \cdot V) \cdot p_\lambda \, dx - \int_\Omega \mathrm{div}(|\nabla p_\lambda|^2 V) \, dx$$

$$- 2\lambda \int_\Omega (\nabla p_\lambda \cdot V) p_\lambda + \lambda \int_\Omega \nabla p_\lambda \cdot V \, dx + \lambda \int_\Omega \mathrm{div}(p_\lambda(p_\lambda - 1) V) \, dx,$$

where one in the second step has differentiated the variational form of the equation for p_λ and in that way eliminated $\dot{p}_\lambda$ by using $p_\lambda - 1$ as a test function. Indeed,

$$
\int_\Omega \nabla \dot{p}_\lambda \cdot \nabla v \, dx - \lambda \int_\Omega \dot{p}_\lambda v \, dx
$$
$$
= - \int_\Omega \nabla(\nabla p_\lambda \cdot V) \cdot \nabla v \, dx - \int_\Omega \nabla p_\lambda \cdot (\nabla v \cdot V) \, dx + \int_\Omega \mathrm{div}((\nabla p_\lambda \cdot \nabla v)V) \, dx
$$
$$
+ \lambda \int_\Omega (\nabla p_\lambda \cdot V) v \, dx + \lambda \int_\Omega p_\lambda (\nabla v \cdot V) \, dx - \lambda \int_\Omega \mathrm{div}(p_\lambda v V) \, dx,
$$

for any $v \in H^2(\Omega) \cap H^1(\Omega, \Gamma_D)$. After some manipulation of terms, one concludes that

$$
\langle p_\lambda \rangle' = \langle \dot{p}_\lambda \rangle + \langle p_\lambda \mathrm{div}V \rangle - \langle p_\lambda \rangle \langle \mathrm{div}V \rangle
$$
$$
= - \langle p_\lambda \rangle \langle \mathrm{div}V \rangle + \langle p_\lambda^2 \mathrm{div}V \rangle - \frac{1}{\lambda} \langle |\nabla p_\lambda|^2 \mathrm{div}V \rangle + \frac{2}{\lambda} \langle \nabla V \nabla p_\lambda \cdot \nabla p_\lambda \rangle,
$$

which for solenoidal V reduces to

$$
\langle p_\lambda \rangle' = \frac{2}{\lambda} \langle \nabla V \nabla p_\lambda \cdot \nabla p_\lambda \rangle.
$$

By substituting the expansion

$$
p_\lambda = 1 + \sum_{i=1}^\infty \beta_i \psi_i, \qquad \beta_i = |\Omega| \frac{\lambda}{\kappa_i - \lambda} \langle \psi_i \rangle,
$$

and integrating in λ the desired formula is obtained, by the Fubini theorem. $\qquad\square$

For instance, in the case of a uniform cylinder,

$$
p_\lambda = \cos(\sqrt{\lambda}x_1) + \tan(\sqrt{\lambda}) \sin(\sqrt{\lambda}x_1).
$$

For solenoidal $V \in W^{1,\infty}(\Omega)$, the shape derivative of the averaged pressure response is

$$
\langle p_\lambda \rangle' = \frac{2}{\lambda} \langle (\partial_1 p_\lambda)^2 \partial_1 V_1 \rangle
$$
$$
= 2 \langle (\sin(\sqrt{\lambda}x_1) - \tan(\sqrt{\lambda}) \cos(\sqrt{\lambda}x_1))^2 \partial_1 V_1 \rangle,
$$

and

$$
\Psi' = \frac{1}{\lambda_{\max} - \lambda_{\min}} \left\langle \left[\frac{2\sin(\sqrt{\lambda})\cos(\sqrt{\lambda}x_1)^2}{\sqrt{\lambda}\cos(\sqrt{\lambda})} - \frac{2\sin(\sqrt{\lambda}x_1)\cos(\sqrt{\lambda}x_1)}{\sqrt{\lambda}} \right]_{\lambda_{\min}}^{\lambda_{\max}} \frac{\partial V_1}{\partial x_1} \right\rangle
$$
$$
+ \frac{1}{\lambda_{\max} - \lambda_{\min}} \left\langle \left[\frac{\sin(\sqrt{\lambda}x_1)\cos(\sqrt{\lambda}x_1)}{\sqrt{\lambda}\cos(\sqrt{\lambda})^2} + \frac{x_1}{\cos(\sqrt{\lambda})^2} \right]_{\lambda_{\min}}^{\lambda_{\max}} \frac{\partial V_1}{\partial x_1} \right\rangle.
$$

A somewhat more direct proof of Lemma III.2.1 goes as follows.

A second proof of Lemma III.2.1. Let $\tilde{p}_\lambda^t$ be such that $\tilde{p}_\lambda^t - 1 \in H^1(\Omega_t, T(\Gamma_D))$ and

$$\int_{\Omega_t} \nabla \tilde{p}_\lambda^t \cdot \nabla v \, dx - \lambda \int_{\Omega_t} \tilde{p}_\lambda^t v \, dx = 0,$$

for all $v \in H^1(\Omega_t, T(\Gamma_D))$, supposing that t is small enough. Then by the Lipschitz transform of the Sobolev space, using that T and T^{-1} are Lipschitz,

$$p_\lambda^t = \tilde{p}_\lambda^t \circ T$$

is such that $p_\lambda^t - 1 \in H^1(\Omega, \Gamma_D)$ and it is the solution to

$$\int_\Omega (\nabla T^{-T} \nabla p_\lambda^t \cdot \nabla T^{-T} \nabla v) |\det \nabla T| \, dx - \lambda \int_\Omega p_\lambda^t v |\det \nabla T| \, dx = 0, \qquad \text{(III.2.23)}$$

for all $v \in H^1(\Omega, \Gamma_D)$. Here, ∇T^{-T} denotes the transpose of the inverse of the gradient of T. Using that ψ_i form a Hilbert basis, let

$$p_\lambda^t = \sum_i \gamma_i(t) \psi_i.$$

Recall that

$$p_\lambda = \sum_i \beta_i \psi_i.$$

Using that

$$\nabla T^{-T} = 1 - t \nabla V + o(t),$$
$$|\det \nabla T| = 1 + t \text{div} V + o(t),$$

as t tends to zero, and expanding the coefficients $\gamma_i(t)$ as

$$p_\lambda^t = \sum_i (\gamma_i^0 + \gamma_i^1 t) \psi_i + o(t),$$

give by equation (III.2.23) that $\gamma_i^0 = \beta_i$ and

$$p_\lambda^t = p_\lambda + t \sum_i \gamma_i^1 \psi_i + o(t),$$

where

$$\gamma_i^1 = \sum_j \frac{\beta_j}{\kappa_i - \lambda} \left[\int_\Omega \nabla V \nabla \psi_i \cdot \nabla \psi_j \, dx + \int_\Omega \nabla \psi_i \cdot \nabla V \nabla \psi_j \, dx \right.$$
$$\left. - \int_\Omega (\nabla \psi_i \cdot \nabla \psi_j) \text{div} V \, dx + \lambda \int_\Omega \psi_i \psi_j \text{div} V \, dx \right]$$
$$+ \frac{\lambda}{\kappa_i - \lambda} \int_\Omega \psi_i \text{div} V \, dx.$$

The shape derivative may then be computed as follows:

$$
\begin{aligned}
\Psi' &= \frac{1}{\lambda_{\max} - \lambda_{\min}} \left(\lim_{t \to 0} \frac{\int_{\lambda_{\min}}^{\lambda_{\max}} \langle p_\lambda^t - p_\lambda \rangle \, d\lambda}{t} - \int_{\lambda_{\min}}^{\lambda_{\max}} \langle p_\lambda \rangle \langle \mathrm{div} V \rangle \, d\lambda \right) \\
&= \frac{1}{\lambda_{\max} - \lambda_{\min}} \lim_{t \to 0} \frac{\int_{\lambda_{\min}}^{\lambda_{\max}} \langle p_\lambda^t - p_\lambda \rangle \, d\lambda}{t} - \langle \mathrm{div} V \rangle \Psi \\
&= \frac{1}{\lambda_{\max} - \lambda_{\min}} \int_{\lambda_{\min}}^{\lambda_{\max}} \sum_i \gamma_i^1 \langle \psi_i \rangle \, d\lambda - \langle \mathrm{div} V \rangle \Psi.
\end{aligned}
$$

For solenoidal V, the computation results in

$$
\Psi' = \frac{2|\Omega|^2}{\lambda_{\max} - \lambda_{\min}} \sum_{i,j} \int_{\lambda_{\min}}^{\lambda_{\max}} \frac{\lambda}{(\kappa_i - \lambda)(\kappa_j - \lambda)} \, d\lambda \langle \nabla V \nabla \psi_i \cdot \nabla \psi_j \rangle \langle \psi_i \rangle \langle \psi_j \rangle.
$$

After evaluation of the integrals the desired formula is again obtained. $\qquad \square$

The condition that V is solenoidal in Lemma III.2.1 is only for presentation purpose. The case of non-solenoidal $V \in W^{1,\infty}(\Omega)$ is covered by both of the above proofs, except for the last step of integration in λ, which then results in lengthier formulas.

III.3 Data sets

The data sets consist of the randomly generated coordinates defining polygonal cylinders and the corresponding objective function Ψ. The coordinates are generated in such a way that the radius of a cylinder varies between 0.1 and 0.5. The coordinates were sampled as independent and identically uniformly distributed random variables, using a pseudo-random number generator. The number of points defining the polygonal boundary might be 1 (uniform cylinder, as in Figure III.3.1(a)), 2 (cone segment), 3, 4, and 5 (as shown in Figure III.3.1(b)). The objective function is computed, as described in the previous section, with finite elements. In total, we have about 700 000 data points in the main data set, which we call Random 5. We have also generated some smaller data sets for evaluation purpose, as well as a set of 100 000 data points for uniform cylinders. The uniform cylinder set is important because it is a set for which we have very high accuracy in the numerical value of the objective function.

For the non-uniform cylinders we have no guarantee that the error is small, as we are doing non-rigorous numerics with finite elements and floating point arithmetic without tracing or bounding the round off errors. In the choice of mesh sizes we have employed standard indicators such as numerically observing what happens to the solution and the objective function under mesh refinement. By means of Lemma III.2.1, we can guarantee for certain intervals and modulo round off errors that the error stays below a threshold τ for small enough domain perturbations of the convex cylinders if the error on the reference is bounded by 2τ. This can be exemplified with perturbations of uniform cylinders under bi-Lipschitz mappings

close to the unit. For the method of validated numerics, bounding the round off errors, we refer to [30].

In Table III.1, an overview of the data sets is provided, where we have indicated the size of different data subsets used for training and evaluation (test), as well as the statistics of mean, variance, minimum, and maximum of the objective function Ψ_h.

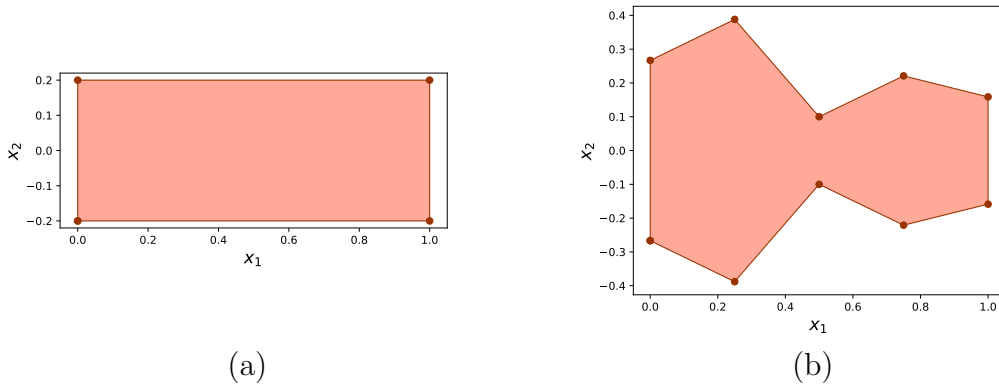The data and the code for data generation is available on the GitHub [19].

Figure III.3.1: A uniform cylinder (a) and a non-uniform polygonal cylinder (b).

Data Set	Size	Category	Mean	Variance	Min	Max
Random 5	200 000	Training	0.0638	0.00860	-0.0918	0.882
Random 5	500 000	Test	0.0636	0.00864	-0.0909	0.991
Random 5 (fine)	20 000	Test	0.0632	0.00869	-0.0876	0.734
Random 3	10 000	Test	0.0833	0.00494	-0.0508	0.631
Random 2	10 000	Test	0.0769	0.00137	-0.0267	0.186
Uniform	100 000	Test	0.0742	0	0.0742	0.0742

Table III.1: Data sets split into training and test categories. The statistics mean, variance, min, and max of Ψ_h are truncated.

III.4   Feedforward dense neural network for approximation of average pressure

As a base model for the average pressure we will use a feedforward fully connected neural network, with the radii of the cylinder at a discrete set of points (1, 2, 3 or 5) as input. The base model is nonlinear, it consists of three hidden layers, each with ReLU activation. We will compare this with a linear model as a point of reference.

III.4.1   Structure of the neural network

The main goal of the paper is to construct a learned algorithm which for a given polygonal cylinder outputs the corresponding average pressure. In this section we describe the main ideas and principles underlying the dense neural network which is used for the prediction of the average pressure level Ψ over a given frequency range. For a rigorous and at the same time concise description of the the deep neural networks construction we refer to [5] and [31].

Let us call Ψ_{ml} the function that for given cylinders outputs the objective function Ψ_h. Inputs to this function are the radial coordinates of the points defining the boundary, 5 along a uniform segmentation of the interval $[0,1]$. The output is one real number Ψ_{ml}, that is we have a regression type of problem. Assume that we have a data set containing values of Ψ for N polygonal cylinders. We will train a learning function on a part of this set. Assigning weights to the inputs, we create a function so that the error in the approximation of Ψ is minimized. Then we evaluate the performance of our function Ψ_{ml} by applying it to the unseen data and measure the accuracy of the predicted average pressures.

The simplest learning function is affine, but it is usually too simple to give a good result. In Section III.6, for the sake of illustration, we compare the results for linear regression and the proposed algorithm, and show that linear regression gives a poor result for nonuniform cylinders. A widely used choice of nonlinearity is a composition of linear functions with so-called "sigmoidal" functions (having S-shaped graph). A smooth sigmoidal function has been a popular choice, but after that numerous numerical experiments indicated that this might not be an optimal choice. In many examples, it has turned out that a piecewise linear function $\mathrm{ReLU}(x) = \max\{0, x\}$ (the positive part x^+ of the linear function x, sometimes called a rectified linear unit) performs better [5]. Specifically, we consider a learning function Ψ_{ml} in the form of a composition

$$\Psi_{\mathrm{ml}}(v) = L_M(R(L_{M-1}(R \cdots (L_1 v)))), \qquad \text{(III.4.1)}$$

where $L_k v = A_k v + b_k$ are affine functions, and $Rx = \mathrm{ReLU}(x)$ is the nonlinear ramp function (rectifies linear unit), the activation function. In this way the output is a recursively nested composition function of inputs: input to the first hidden layer, input from the first to the second hidden layer, ..., input from the last hidden layer to output layer. Each hidden layer in Figure III.4.1 contains both the linear L_k and the nonlinear activation function R. For our purpose seems sensible to have three hidden layers with 128 nodes in each layer. In this sense, we use a what could be called a deep neural network. The elements of the matrices A_k and the bias vectors b_k are weights in our learning function. Note that to have 128 nodes in the first hidden layer, the first matrix A_1 should have 128 rows and 5 columns. The goal of the learning is to choose the weights to minimize the error over training sample, such that it generalize well to unseen data.
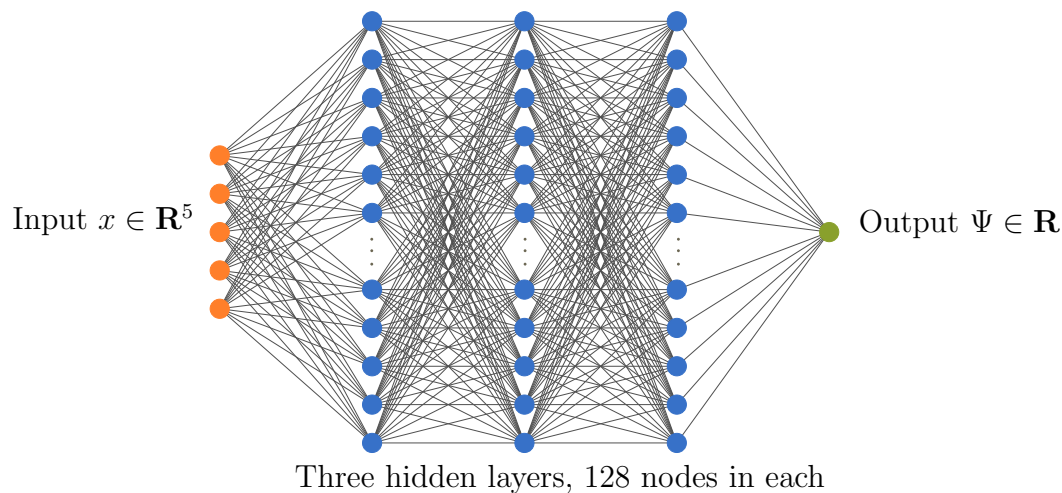
Three hidden layers, 128 nodes in each

Figure III.4.1: A feedforward network with three hidden layers.

III.4.2 Hyperparameters and training

The choice of hyperparameters is important for the learning of the model. We choose the following:

- **Nonlinearity:** ReLU.

- **Hidden layers:** Three hidden layers, 128 nodes in each.

- **Optimizer:** ADAM.

- **Learning rate:** The step size s_k in the gradient descent is scheduled to have polynomial decay from $s_0 = 0.001$ to 0.0001 according to $s_k = s_0/\sqrt{k}$ in $10\,000$ steps.

- **Loss function:** Mean squared error (MSE).

- **Validation split:** 20% of the training set.

- **Early stopping:** In order to avoid overtraining, the change of the MSE for the validation set 10^{-5} counts as an improvement. If we have 25 iterations without improvement, we stop and use the weights that give the minimum MSE up to this point.

- **Initializer:** GlorotUniform.

In the last section, we provide a hyperparameter grid that indicates together with the results of Section III.5, that the performance of the model is not that sensitive to the values of the parameters around the chosen ones.

III.5 Performance of the feedforward network model

Our aim is to construct a ML algorithm to approximate Ψ based on the data for Ψ_h (computed with finite elements) with the same accuracy on the unseen data as the numerical error $\Psi - \Psi_h$. Here, we present the measured performance on our data sets.

In Figure III.5.1, we present the dependence of the error on the size of the training set. For each training set, we train the model ten times and take the mean of the mean squared error (mean MSE). The purple curve in Figure III.5.1(a) shows the MSE for polygonal cylinders with five random points defining the boundary. The objective function Ψ_h is computed on a mesh with density approximately three times higher than regular (referred to as "fine"). In Figure III.5.1(b), we present the percentage of the unseen data used for the test that gives the mean absolute error less than 0.01. Again, here we take the mean value of the percentage after ten training sessions, the reason being the stochastic gradient descent algorithms used which results in some nonzero variance.

The choice of the threshold 0.01 is based on numerical indication of what is a bound on the error for almost all data points. We do not guarantee this bound on the error in the numerical data. In in spite of that, we believe it serves as an illustrative example in that similar behavior in the accuracy of the machine learning model on unseen data is expected if this threshold is increased, or if the error in the data had been zero.

Numerical values for the best model are presented in Tables III.2 and III.3 in Section III.6. For example, for polygonal cylinders defined by five randomly generated points, over 95% are predicted with mean absolute error 0.01 (the accuracy of the numerical data) if the training set contains $200\,000$ data points. The MSE for our model trained on $200\,000$ data points is $2.31\cdot10^{-5}$ for uniform cylinders and $5.5\cdot10^{-5}$ for polygonal cylinders. Clearly, the MSE is much smaller than the variance in the data for the test set Random 5 (Table III.1).

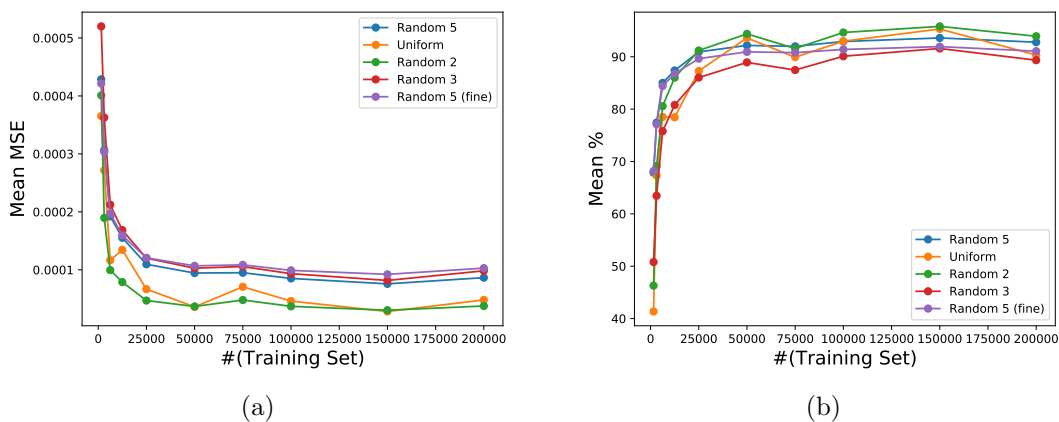
(a)   (b)

Figure III.5.1: (a) Dependence of the MSE on the training set size. (b) Percentage of the unseen data with absolute error less than 0.01 as a function of the training set size.

Since we present the mean-value of the MSE, we need to analyze the standard deviation. In Figure III.5.2, we present the MSE error and the percentage of unseen data with absolute error below threshold (red curve) together with the standard deviation for polygonal cylinders with five random points (shadowed region). Figure III.5.3 illustrates the MSE for different epoch numbers for training and validation sets. We observe that the error on the training set, on the validation set, and on the test set are close.
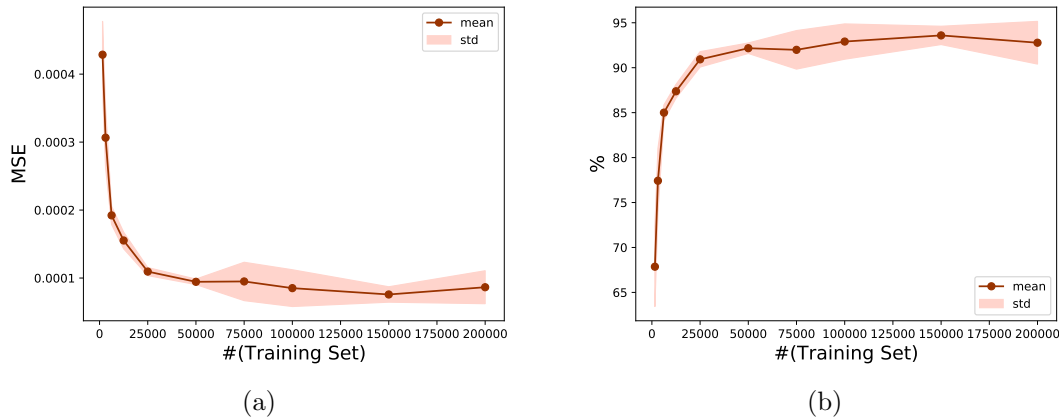

(a)	(b)

Figure III.5.2: (a) MSE and the standard deviation for polygonal cylinders with 5 random points. (b) Percentage of the unseen data and the standard deviation with absolute error less than 0.01 as a function of the training set size.

When it comes to the choice of hyperparameters, the numerical experiments have shown that reducing number of layers to two shows poor result, while increasing the number of layers and number of nodes in each layer does not improve much the result. We have also tested YOGI [32], but we did not manage to tune it to perform any better than ADAM. The decaying learning rate gives better accuracy than a constant one.

III.5.1 Performance on an out of sample set

To complement the evaluation of the trained models on the unseen data, we here include an out of sample set. Specifically, we choose a one-parameter family of convex symmetric cylinders defined as follows, and illustrated in Figure III.5.4. For the model parameters of minimal and maximal radii 0.1 and 0.5, respectively, and center axis between 0 and 1, we let the midpoint radius $r(1/2)$ be a parameter varying between 0.1 and 0.5. For each midpoint radius $r(1/2)$, we let $r(0) = r(1) = 0.1$ and construct a circular arc connecting the points $(0, 0.1), (1/2, r(1/2)), (1, 0.1)$. In this way, by mirroring the arc, a symmetric convex cylinder is constructed.

As justified by Lemma III.2.1, we may compute approximations of the averaged response Ψ, using piecewise linear interpolations of the cylinder boundary in local charts. We do this with 19 uniform grid points on each arc, as well as the down sampled 5 point uniform grid arcs. The squared error between 19 and 5 points numerically computed values of Ψ, and the variation of the error over the parameter
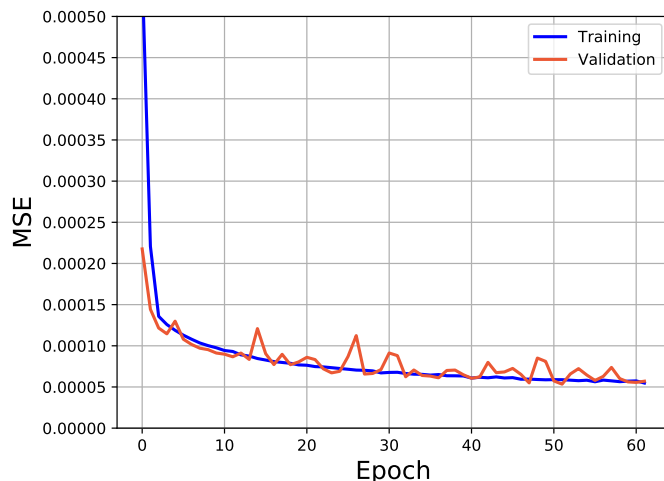
Figure III.5.3: The training history for Ψ_{ml} with the mean squared error for the total training set split into training and validation parts. The history shown is for one trained model using a training set with $200\,000$ points from the set Random 5.

interval $[0.1, 0.5]$ is shown in Figure III.5.5 with label FEM. The frequency range is again the interval $(\lambda_{\mathrm{min}}, \lambda_{\mathrm{max}}) = (0, 60)$.

  We compute the predictions in Ψ of the models trained with $200\,000$ points from the set Random 5, as evaluated in Figure III.5.1. In order to do so, we let the radius parameter $r(1/2)$ vary on a uniform grid of 100 points, and down sample the cylinder radius to 5 points on each arc. The mean squared error computed against the 19 points arc sets is shown in Figure III.5.5 with label ML.

  Numerically, the mean squared error in Ψ between 19 points and the down sampled 5 points cylinder is truncated to $7.55 \cdot 10^{-5}$, while the mean error of the predictions is truncated to $6.10 \cdot 10^{-5}$. For comparison, we recall that the best DNN model evaluated to a mean squared error on the set Random 5 truncated to $5.50 \cdot 10^{-5}$, according to Table III.2. This verifies that indeed the performance of the trained models of the objective function Ψ on sets of convex cylinders is indicated by the performance on our test sets when the domains are close, as described in Section III.2.4.

III.6   Comparison with a linear model

One can ask why the linear regression would not be perform well in this case. To understand the nature of the nonlinearity in our problem, we look at cylinders with radius $r(x_1)$ affine in x_1. For radius $0.1 \leq r \leq 0.5$, and $x_1 \in (0, 1)$, the set of cylinders may be parametrized by $r(0)$ and $r(1)$. For the interval $(\lambda_{\mathrm{min}}, \lambda_{\mathrm{max}}) = (0, 60)$, we compute a numerical approximation Ψ_h of the objective function Ψ. In Figure III.6.1(a), Ψ_h is shown. Of course Ψ is linear for uniform cylinders, as it is constant. On the diagonal $r(0) = r(1)$ in the Figure III.6.1(a), we see the value of this constant. Off the diagonal, we see that Ψ_h is clearly not the graph of a linear function. A more careful inspection shows that Ψ_h is smooth and seems to be linear everywhere except in the upper left corner of the figure, where it shows rapid growth
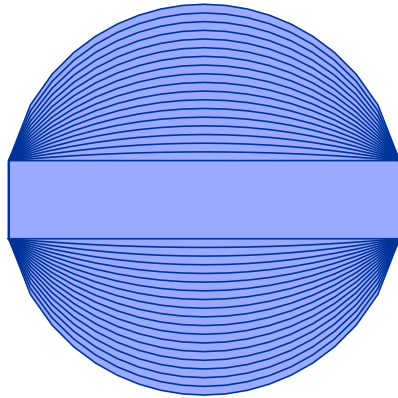
Figure III.5.4: The one-parameter out of sample family of convex cylinders.
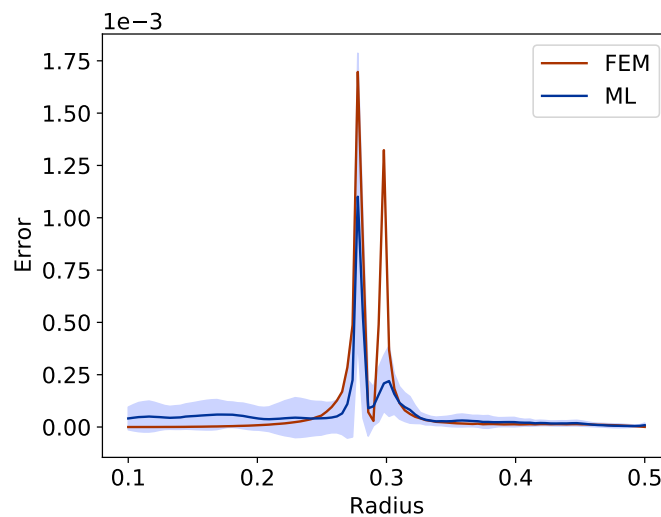
Figure III.5.5: The squared error between the 19 and 5 points FEM for radius $r(1/2)$, and the mean squared error (shadowed area is standard deviation) in the predictions of the trained models ML. The models used here are the 10 obtained by training on sets with $200\,000$ points from the set Random 5. The two peaks come from that the 19 points cylinder and the 5 point cylinder, both hit the spectrum for exactly one value of $r(1/2)$ in the interval $[0.1, 0.5]$, nonorthogonal to the data in L^2.

in a narrow region. We know that Ψ and Ψ_h are defined for intervals $(0, \lambda_{\max})$ for almost every $\lambda_{\max} > 0$, but not for all. Namely, Ψ_h might show singular behavior in the vicinity of a set of positive one-dimensional measure, where p_λ is singular. The approximation Ψ_{ml} we get with the ML algorithm gives largest error exactly in this singularity region, as seen in Figure III.6.1(b). This verifies the need for a nonlinear activation function in our problem even if restricted to the cylinders with affine radii as functions of x_1.
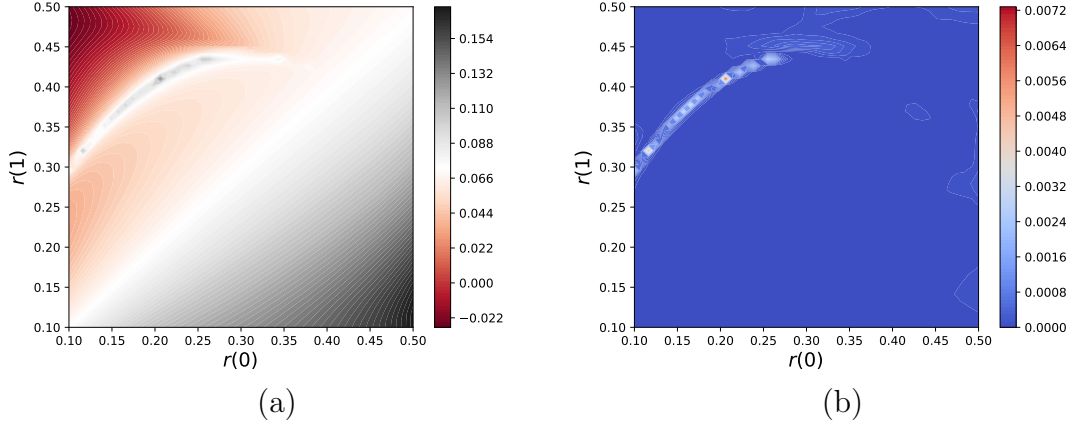

(a)   (b)

Figure III.6.1: The value of Ψ_h for cylinders with affine radii and $\lambda_{\max} = 60$ (a). The squared error between Ψ_{ml} and Ψ_h (b).

In Tables III.2 and III.3, the errors of the approximations on the Uniform and Random 5 test sets of unseen data are provided. The floating point numbers have been truncated. For comparison, we include both a linear model and the proposed nonlinear model DNN. We train the models for polygonal cylinders with five random points. One can see that the proposed DNN model performs much better than the linear one, both on uniform and non-uniform cylinders.

	TS = Training Set		Mean Squared Error	
Model	**TS**	**#(TS)**	**Uniform**	**Random 5**
Linear	Random 5	200 000	2.56e-3	1.91e-3
DNN	Random 5	200 000	2.31e-5	5.50e-5

Table III.2: The performance on unseen data of the converged linear and nonlinear models. The mean squared error on unseen data. For the dense neural network model (DNN), the performance is for the best of the sampled models in the sense of minimum mean squared error. The floating point numbers are truncated.

Conclusions

We have proposed a feedforward dense neural network for predicting the average sound pressure response over a frequency range. We have shown for polygonal

	TS = Training Set		**% Abs Err < 0.01**	
Model	**TS**	**#(TS)**	**Uniform**	**Random 5**
Linear	Random 5	200 000	46.9	22.1
DNN	Random 5	200 000	98.3	95.7

Table III.3: The performance on unseen data of the converged linear and nonlinear models. The percentage of unseen data with an absolute error $|\Psi_{\mathrm{ml}} - \Psi_h|$ less than 0.01). For the dense neural network model (DNN), the performance is for the best of the sampled models in the sense of minimum mean squared error. The floating point numbers are truncated.

cylinders that the obtained results are sufficiently accurate in that they reach the estimated accuracy of the numerical data. Although the amount of data needed in order to reach the desired accuracy could be considered as big, it is expected that the results would serve as a point of reference for more advanced machine learning models. The performance of the feedforward dense neural network has been evaluated. The dependence of the percentage accurately predicted samples and the mean squared error on the training set size is presented.

Acknowledgments.

PAPER III. ML FOR
FREQUENCY RESPONSE

III.7 A Hyperparameter grid

To supplement Section III.4.2 we here provide a grid around the model and training parameter values specified. In particular, we choose the parameters (i) number of hidden layers, (ii) number of nodes in each layer, and (iii) the fraction of the training data used for the validation split. For each 3-tuple of parameters, we present in Table III.4 the mean squared error on unseen data from the data sets Uniform and Random 5. The data sets used for training was 200 000 points from the Random 5 training set.

Hyperparameter			Mean Squared Error	
Hidden Layers	Layer Size	Validation Split %	Uniform	Random 5
2	64	10	3.98e-5	1.17e-4
2	64	20	4.64e-5	1.53e-4
2	64	30	1.37e-4	1.44e-4
2	128	10	4.80e-5	8.45e-5
2	128	20	5.00e-5	8.74e-5
2	128	30	4.65e-5	9.61e-5
2	192	10	1.21e-5	7.38e-5
2	192	20	3.15e-5	7.98e-5
2	192	30	9.42e-6	8.47e-5
3	64	10	5.21e-5	8.25e-5
3	64	20	1.79e-5	7.91e-5
3	64	30	4.44e-5	9.35e-5
3	128	10	1.78e-5	6.01e-5
3	128	20	1.29e-5	5.75e-5
3	128	30	9.45e-5	5.75e-5
3	192	10	1.75e-5	5.09e-5
3	192	20	1.07e-5	5.20e-5
3	192	30	7.97e-6	5.55e-5
4	64	10	2.02e-5	7.40e-5
4	64	20	1.86e-5	6.26e-5
4	64	30	2.47e-5	8.25e-5
4	128	10	1.68e-5	5.34e-5
4	128	20	3.00e-5	5.60e-5
4	128	30	3.31e-5	5.46e-5
4	192	10	1.04e-5	4.91e-5
4	192	20	1.40e-5	5.39e-5
4	192	30	1.80e-5	5.27e-5

Table III.4: The mean squared errors on the unseen data Uniform and Random 5 for various values of the parameters. The numerical values of the mean squared errors are truncated.

References

[1] E. Skudrzyk. *The foundations of acoustics: basic mathematics and basic acoustics.* Springer Science & Business Media, 2012.

[2] BSEN ISO. "7235: 2003". In: *Acoustics–Laboratory measurement procedures for ducted silencers and air-terminal units – Insertion loss, flow noise and total pressure loss* (2003).

[3] J. Schmidhuber. "Deep learning in neural networks: An overview". In: *Neural networks* 61 (2015), pp. 85–117.

[4] I. Goodfellow, Y. Bengio, and A. Courville. *Deep Learning (Adaptive Computation and Machine Learning Series).* 2016.

[5] G. Strang. *Linear algebra and learning from data.* Wellesley-Cambridge Press, 2019.

[6] M. J. Bianco, P. Gerstoft, J. Traer, E. Ozanich, M. A. Roch, S. Gannot, and C.-A. Deledalle. "Machine learning in acoustics: Theory and applications". In: *The Journal of the Acoustical Society of America* 146.5 (2019), pp. 3590–3628.

[7] I. E. Lagaris, A. Likas, and D. I. Fotiadis. "Artificial neural networks for solving ordinary and partial differential equations". In: *IEEE transactions on neural networks* 9.5 (1998), pp. 987–1000.

[8] S. Ossandón, C. Reyes, and C. M. Reyes. "Neural network solution for an inverse problem associated with the Dirichlet eigenvalues of the anisotropic Laplace operator". In: *Computers & Mathematics with Applications* 72.4 (2016), pp. 1153–1163.

[9] J. Sirignano and K. Spiliopoulos. "DGM: A deep learning algorithm for solving partial differential equations". In: *Journal of computational physics* 375 (2018), pp. 1339–1364.

[10] J. Adler and O. Öktem. "Solving ill-posed inverse problems using iterative deep neural networks". In: *Inverse Problems* 33.12 (2017), p. 124007.

[11] J. Berg and K. Nyström. "A unified deep artificial neural network approach to partial differential equations in complex geometries". In: *Neurocomputing* 317 (2018), pp. 28–41.

[12] M. Raissi, P. Perdikaris, and G. E. Karniadakis. "Physics-informed neural networks: A deep learning framework for solving forward and inverse problems involving nonlinear partial differential equations". In: *Journal of Computational Physics* 378 (2019), pp. 686–707.

[13] M. Baymani, S. Effati, and A. Kerayechian. "A Feed-Forward Neural Network for Solving Stokes Problem". In: *Acta applicandae mathematicae* 116.1 (2011), p. 55.

[14] M. Baymani, S. Effati, H. Niazmand, and A. Kerayechian. "Artificial neural network method for solving the Navier–Stokes equations". In: *Neural Computing and Applications* 26.4 (2015), pp. 765–773.

PAPER III. ML FOR FREQUENCY RESPONSE

[15]   S. Ossandón and C. Reyes. "On the neural network calculation of the Lamé
        coefficients through eigenvalues of the elasticity operator". In: *Comptes Rendus
        Mecanique* 344.2 (2016), pp. 113–118.

[16]   S. Ossandón, C. Reyes, P. Cumsille, and C. M. Reyes. "Neural network ap-
        proach for the calculation of potential coefficients in quantum mechanics". In:
        Computer Physics Communications 214 (2017), pp. 31–38.

[17]   G. Rizzuti, A. Siahkoohi, and F. J. Herrmann. "Learned iterative solvers for
        the Helmholtz equation". In: *81st EAGE Conference and Exhibition 2019*.
        Vol. 2019(1). European Association of Geoscientists & Engineers. 2019, pp. 1–
        5.

[18]   K. Hornik, M. Stinchcombe, and H. White. "Universal approximation of an
        unknown mapping and its derivatives using multilayer feedforward networks".
        In: *Neural networks* 3.5 (1990), pp. 551–560.

[19]   K. Pettersson, A. Karzhou, and I. Pettersson. *FRRE1.* `https://github.com/
        klaspettersson/FrRe1`. 2020.

[20]   M. Abadi et al. *TensorFlow: Large-Scale Machine Learning on Heterogeneous
        Systems.* Software available from tensorflow.org. 2015. URL: `https://www.
        tensorflow.org`.

[21]   D. P. Kingma and J. Ba. "Adam: A method for stochastic optimization". In:
        arXiv preprint arXiv:1412.6980 (2014).

[22]   V. Hernandez, J. E Roman, and V. Vidal. "SLEPc: A scalable and flexible
        toolkit for the solution of eigenvalue problems". In: *ACM Transactions on
        Mathematical Software (TOMS)* 31.3 (2005), pp. 351–362.

[23]   F. Hecht. "New development in FreeFem++". In: *J. Numer. Math.* 20.3-4
        (2012), pp. 251–265. ISSN: 1570-2820. URL: `https://freefem.org`.

[24]   M. S. Alnæs et al. "The FEniCS Project Version 1.5". In: *Archive of Numerical
        Software* 3.100 (2015). DOI: `10.11588/ans.2015.100.20553`.

[25]   K. K. Choi and N.-H. Kim. *Structural sensitivity analysis and optimization 1:
        linear systems.* Springer Science & Business Media, 2006.

[26]   G. Allaire. *Numerical analysis and optimization: an introduction to mathe-
        matical modelling and numerical simulation.* Oxford university press, 2007.

[27]   J. Necas. "Les méthodes directes en théorie des équations elliptiques". In:
        (1967).

[28]   V. Komkov, K. K. Choi, and E. J. Haug. *Design sensitivity analysis of struc-
        tural systems.* Vol. 177. Academic press, 1986.

[29]   P. Grisvard. *Elliptic Problems in Nonsmooth Domains.* Vol. 69. SIAM, 1985.

[30]   W. Tucker. *Validated numerics: a short introduction to rigorous computations.*
        Princeton University Press, 2011.

[31]   G. Montavon, G. Orr, and K.-R. Müller. *Neural networks: tricks of the trade.*
        Vol. 7700. springer, 2012.

[32]   S. Reddi, M. Zaheer, D. Sachan, S. Kale, and S. Kumar. "Adaptive methods for nonconvex optimization". In: *NIPS* (2018).

PAPER III. ML FOR
FREQUENCY RESPONSE

PAPER IV

Acoustic Coefficient Inverse Problem in Pseudo-Frequency Domain[1]

Andrei Karzhou

UiT The Arctic University of Norway

Irina Pettersson

Chalmers University of Technology and Gothenburg University, Sweden

Larisa Beilina

Chalmers University of Technology and Gothenburg University, Sweden

Klas Pettersson

Freelance, Sweden

Abstract

We present a Lagrangian approach for the solution to an acoustic coefficient inverse problem. Given data in the pseudo-frequency domain, after the Laplace transform, we minimize a time-independent Tikhonov functional using the Lagrangian method. We study also the dependence of the reconstruction on the regularization terms in the Tikhonov functional.

---

[1]To appear in *Springer's conference proceeding Gas Dynamics with Applications in Industry and Life Sciences – On Gas Kinetic/Dynamics and Life Science Seminar, March 25–26, 2021 and March 17–18, 2022, Springer, Cham, Switzerland.*

IV.1   Introduction

This paper concerns an acoustics coefficient inverse problem (CIP). Namely, given a scattered field in a computational domain, we will determine the wave speed function in the time-harmonic acoustic wave equation. The technique combines the Lagrangian method and the conjugate gradient algorithm for the iterative update of the wave speed function.

In a uniform medium with constant material parameters, sound waves propagate with a constant speed, unless they are refracted, reflected, diffracted, or perturbed in some other manner. In the presence of a heterogeneity, local variations of the density of the medium cause a change in the field distribution when acoustic waves are traveling in the medium. In many cases it is possible to reconstruct material parameters of the medium by solving inverse problems given the observed data in the bulk or on the boundary of the domain of interest.

There are numerous practical applications of inverse problems, and in particular of CIPs. Among them are the subsurface imaging, nondestructive testing of materials and detection of landmines [1, 2, 3, 4], archaeology, construction of photonic crystals [5] and cloaking materials [6], remote sensing and medical imaging [7, 8].

Inverse problems are usually ill-posed problems, that is at least one of the three conditions for a well-posed problem (existence, uniqueness, or stability) is violated. One reason for this is that measurement data resulting from observations and experiments, the input data, are accompanied by inevitable errors, so the sought solutions to inverse problems will also be determined with an error. It turns out that most of the inverse problems in natural sciences are unstable, that is arbitrarily small errors in input data correspond to large errors in the computed solution to the inverse problem. To overcome these difficulties, one can use a regularizing functional introduced by Tikhonov (see [9] and [10]) and named after him. In the present work, we use an optimization approach, and minimize the regularized Tikhonov functional by minimizing a Lagrangian. Based on the optimality conditions for the Lagrangian, we formulate a conjugate gradient algorithm for the iterative update of the unknown function. The Lagrangian method is similar to the one applied in [1, 11, 12] for the solution to time-dependent CIPs. In many applications, computational domains are large, and the parameters of the media are approximately constant everywhere except for a small part, where the coefficients change. In such cases the domain decomposition method described in [11, 12, 13] is beneficial for the numerical solution to the CIP.

The rest of this paper is organized as follows. In Section IV.2, we formulate forward and inverse problems. In Section IV.3, we present the Tikhonov functionals to be minimized, and describe the Lagrangian approach to solve the CIP. The numerical method and results are presented in Sections IV.4–IV.5, as well as a case of noisy data in Section IV.6. In Section IV.7, we describe the Laplace transform of a sinusoidal impulse related to the model problem.

IV.2   Model problem in the pseudo-frequency domain

As a model problem, we consider a stationary boundary value problem stated in $\Omega = (0,1) \times (0,1) \subset \mathbf{R}^2$. The boundary of Ω consists of three parts (see Fig. IV.2.1):

$$\Gamma_1 = \{(x_1, x_2): \ 0 \le x_1 \le 1, \ x_2 = 1\}, \quad \Gamma_2 = \{(x_1, x_2): \ 0 \le x_1 \le 1, \ x_2 = 0\},$$
$$\Gamma_3 = \{(x_1, x_2): \ 0 \le x_2 \le 1, \ x_1 = 0\} \cup \{(x_1, x_2): \ 0 \le x_2 \le 1, \ x_1 = 1\}.$$
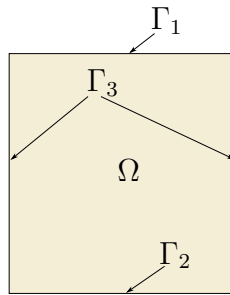

Figure IV.2.1: Computational domain Ω with boundary $\Gamma = \Gamma_1 \cup \Gamma_2 \cup \Gamma_3$.

For $s \ge 0$, let $u(s,x)$ be a unique solution to the following problem:

$$\Delta u(s,x) - s^2 a(x) u(s,x) = 0, \qquad\qquad x \in \Omega, \qquad\qquad \text{(IV.2.1)}$$
$$\nabla u(s,x) \cdot \nu + s\, u(s,x) = s, \qquad\qquad x \in \Gamma.$$

Here ν is the external unit normal. The forward problem consists of determining the solution $u(s,x)$ given the coefficient $a(x)$. The main goal of the present work is to solve the inverse problem, that is, to reconstruct the coefficient $a(x)$ given the data $\tilde{u}(s,x)$ in the pseudo-frequency domain, for $x \in \Omega$.

The weak form of (IV.2.1) reads: Find $u \in H^1(\Omega)$ such that

$$(\nabla u, \nabla \phi)_\Omega + \left(s^2 a\, u, \phi\right)_\Omega - (s\, u - s, \phi)_\Gamma = 0, \qquad\qquad \text{(IV.2.2)}$$

for any smooth test function $\phi \in C^1(\overline{\Omega})$, where

$$(u, v)_\Omega = \int_\Omega u \cdot v \, dx, \qquad (u, v)_\Gamma = \int_\Gamma u \cdot v \, d\sigma.$$

The motivation for using (IV.2.1) in the reconstruction of a given the data $\tilde{u}(s,x)$ in the pseudo-frequency domain is that (IV.2.1) can be obtained by applying the Laplace transform to the time-domain wave equation, where an absorbing boundary condition is assumed on the boundary Γ, and the wave is initialized by a sinusoidal impulse. Namely, consider the following time-dependent problem:

$$a(x)\partial_{tt} U(t,x) - \Delta U(t,x) = 0, \qquad\qquad (t,x) \in (0,T] \times \Omega,$$
$$\nabla U \cdot \nu + \partial_t U = f_\omega(t), \qquad\qquad (t,x) \in (0,T] \times \Gamma, \qquad \text{(IV.2.3)}$$
$$U(0,x) = \partial_t U(0,x) = 0, \qquad\qquad x \in \Omega,$$

where, for a fixed angular frequency $\omega > 0$,

$$f_\omega(t) = \begin{cases} \dfrac{\omega^2}{2\pi}\sin(\omega t), & \text{for } t \in \left(0, \dfrac{2\pi}{\omega}\right], \\ 0, & \text{otherwise.} \end{cases}$$

Denote the Laplace transform of $U(t, x)$ by $\mathcal{L}\{U\} = u(s, x)$. It will be showed below (see Lemma 1), that $\mathcal{L}\{f_\omega\}(s)$ converges in the sense of distributions to $\mathcal{L}\{\delta'\}(s) = s$, as $\omega \to \infty$, where the derivative of the delta function $\delta'(t)$ is defined on smooth test functions $\varphi \in C_0^\infty(\mathbf{R})$ by $\langle \delta', \varphi \rangle = -\varphi(0)$. In this way, as $\omega \to 0$, we obtain (IV.2.1). Note that, by the linearity of the problem, the solution with $\mathcal{L}\{f_\omega\}(s)$ present on the whole boundary can be regarded as a superposition of four solutions with $\mathcal{L}\{f_\omega\}(s)$ only on one of the sides at a time.

The spatial domain where a wave propagates might be demandingly large for numerical computation. To limit this domain, we impose boundary conditions that are intended to give a solution approximating the result in a larger domain. Such artificial boundary conditions are sometimes called absorbing, and a main difficulty is that physical absorbing boundary conditions may be nonlocal and thus computationally more expensive. For simplicity, we choose absorbing boundary conditions by introducing $\partial_t U$ on Γ.

Remark 1. One can also initiate the wave from one of the sides in (IV.2.1) or (IV.2.3), for example on Γ_1. With absorbing boundary conditions on $\Gamma_2 \cup \Gamma_3$, the stationary problem becomes

$$\begin{aligned} \Delta u - s^2 a(x) u &= 0, & x \in \Omega, \\ \nabla u \cdot \nu + s\, u &= s, & x \in \Gamma_1, \\ \nabla u \cdot \nu + s\, u &= 0, & x \in \Gamma_2 \cup \Gamma_3. \end{aligned} \qquad (\text{IV.2.4})$$

In this case it is more difficult to reconstruct small inclusions close to Γ_2, using the method of this paper.

IV.3 Lagrangian approach for CIP

To reconstruct the coefficient $a(x)$ given the data $\widetilde{u}(s, x)$ in Ω, we study the minimization problem for a Tikhonov functional using the Lagrangian method. We focus on investigating how the presence of derivatives ∇u, $\nabla\nabla u$ in the regularization term affects the reconstruction. We consider the following Tikhonov functional for three different choices of regularization:

$$J_{L^2}(u, a) = \frac{1}{2}\int_\Omega (u - \widetilde{u})^2\, dx + \frac{\gamma}{2}\int_\Omega (a - 1)^2\, dx, \qquad (\text{IV.3.1})$$

$$J_{H^1}(u, a) = \frac{1}{2}\int_\Omega (u - \widetilde{u})^2 + \frac{1}{2}\int_\Omega |\nabla(u - \widetilde{u})|^2\, dx + \frac{\gamma}{2}\int_\Omega (a - 1)^2\, dx, \qquad (\text{IV.3.2})$$

$$J_{H^2}(u, a) = \frac{1}{2}\int_\Omega (u - \widetilde{u})^2\, dx + \frac{1}{2}\int_\Omega |\nabla u - \nabla\widetilde{u}|^2\, dx \qquad (\text{IV.3.3})$$

$$+ \frac{1}{2}\int_\Omega |\nabla\nabla u - \nabla\nabla\widetilde{u}|^2\, dx + \frac{\gamma}{2}\int_\Omega (a - 1)^2\, dx,$$

subject to the constraint that u is the solution to problem (IV.2.1) with coefficient a, where $\nabla\nabla$ denotes the Hessian, and $\gamma > 0$ and s are treated as parameters. The function $\widetilde{u}$ represents the observed data. We assume that u and $\widetilde{u}$ are sufficiently smooth.

For each choice of the functional $J(u, a)$ in (IV.3.1)–(IV.3.3), we introduce the Lagrangian $L(u, a, \lambda)$:

$$L(u, a, \lambda) = J(u, a) - (\nabla u, \nabla \lambda)_\Omega - \left(s^2 au, \lambda\right)_\Omega + (s - su, \lambda)_\Gamma. \qquad \text{(IV.3.4)}$$

Now we compute the derivatives of the Lagrangian with respect to λ, u, and a, and apply the optimality condition. Equating $L'_\lambda(u, a, \lambda) = 0$ yields the direct problem (IV.2.1) with weak formulation (IV.2.2).

Differentiating (IV.3.4) with respect to u gives the adjoint problem in the weak form:

$$(\nabla \lambda, \nabla \varphi)_\Omega + (s^2\, a\, \lambda, \varphi)_\Omega + (s\lambda, \varphi)_\Gamma = \langle \partial_u J, \varphi \rangle, \qquad \text{(IV.3.5)}$$

for all $\varphi \in C^1(\overline{\Omega})$. For the three choices of the functional (IV.3.1)–(IV.3.3), we obtain the following derivatives:

$$\langle \partial_u J_{L^2}, \varphi \rangle = (u - \widetilde{u}, \varphi)_\Omega, \qquad \text{(IV.3.6)}$$
$$\langle \partial_u J_{H^1}, \varphi \rangle = (u - \widetilde{u}, \varphi)_\Omega + (\nabla(u - \widetilde{u}), \nabla\varphi)_\Omega, \qquad \text{(IV.3.7)}$$
$$\langle \partial_u J_{H^2}, \varphi \rangle = (u - \widetilde{u}, \varphi)_\Omega + (\nabla(u - \widetilde{u}), \nabla\varphi)_\Omega + (\nabla\nabla(u - \widetilde{u}), \nabla\nabla\varphi)_\Omega. \qquad \text{(IV.3.8)}$$

For the numerical computations, we are going to use the weak formulations (IV.3.6)–(IV.3.8). The corresponding strong formulations are derived in the standard way. For example, the strong formulation of (IV.3.5) with (IV.3.7) is

$$\begin{aligned} \Delta\lambda - s^2 a\lambda &= -(u - \widetilde{u}) + \Delta(u - \widetilde{u}), & x \in \Omega, \\ \nabla\lambda \cdot \nu + s\lambda &= 0, & x \in \Gamma. \end{aligned} \qquad \text{(IV.3.9)}$$

Then the Fréchet derivative of $J_{H^2}(u, a)$ at a given a, with $u = u(a)$ solving (IV.2.1), and $\lambda = \lambda(a)$ solving (IV.3.5), in the direction of small enough bounded δa is

$$J'_{H_2}(a)\delta a := \partial_a J_{H^2}(u(a), a)\delta a = \int_\Omega \delta a \left[-s^2 u\lambda + \gamma(a - 1) \right] dx.$$

This derivative will be be used in the gradient descent method, and we denote

$$g = -s^2\lambda u + \gamma(a - a_0). \qquad \text{(IV.3.10)}$$

Note that the extra terms containing the derivatives of u show up only in the adjoint problem, and affect neither the direct problem, nor the derivative of the Lagrangian with respect to a.

Remark 2 (Variational approach to CIP)**.** One can also apply the variational approach directly, avoiding introducing a Lagrangian. We consider, as above, the Tikhonov functionals (IV.3.1)–(IV.3.3) subject to the constraint that u is the solution to problem (IV.2.1) with coefficient a, and $\gamma > 0$ and s are treated as parameters. Note that in the Lagrangian approach, we do not assume that u solves

(IV.2.1). Here, we minimize functionals subject to a PDE constraint, and consider the functionals to depend on a only, denoting $J_{L^2} = J_{L^2}(a) = J_{L^2}(u(a), a)$, and so on. The function $\widetilde{u}$ is the observed data, that is a solution to (IV.2.1) with given coefficient a.

Denote the variational form of (IV.2.4) by $b(u, v) = l(v)$, that is

$$b(u, v) = \int_\Omega \nabla u \cdot \nabla v \, dx + s^2 \int_\Omega a \, u \, v \, dx + s \int_\Gamma uv \, d\sigma = s \int_\Gamma v \, d\sigma = l(v),$$

for all admissible test functions v. Then the Fréchet derivative of $J_{H^2}(a)$ at a given a in the direction of small enough bounded δa is given by

$$J'_{H^2}(a)\delta a = l'(\lambda) - b'(\lambda, u) + \gamma \int_\Omega \delta a(a - 1) \, dx$$

$$= \int_\Omega \delta a \big[-s^2 u\lambda + \gamma(a - 1) \big] \, dx, \qquad (\text{IV.3.11})$$

noting that the derivatives of the bilinear and linear forms, with respect to a in the direction of δa, are

$$b'(u, v) = s^2 \int_\Omega \delta a \, uv \, dx, \qquad l'(v) = 0,$$

and λ solves the adjoin problem

$$b(\lambda, v) = \int_\Omega (u - \widetilde{u})v \, dx + \int_\Omega \nabla(u - \widetilde{u}) \cdot \nabla v \, dx + \int_\Omega \nabla\nabla(u - \widetilde{u}) \cdot \nabla\nabla v \, dx,$$

$$(\text{IV.3.12})$$

for all admissible test functions v. The linearizations of the functionals $J_{L^2}(a)$ and $J_{H^1}(a)$ are given by (IV.3.11), after suppressing the corresponding higher order terms in the adjoint problem (IV.3.12) accordingly.

IV.4   Algorithm

Reconstruction Algorithm

Fix a target $\widetilde{u}$ and $s \geq 0$.

Step 0. Choose an initial guess a^0, the function f_0, and let u^0 be the solution to the problem (IV.2.1) with $a = a^0$, and let λ^0 be the solution to the problem (IV.3.12) with $a = a^0$, $u = u^0$, and target $\widetilde{u}$.

Step 1 (Gradient descent). For $m \geq 1$, let a^m be defined by

$$a^m = a^{m-1} + \delta(s^2 u^{m-1}\lambda^{m-1} - \gamma(a^{m-1} - 1)), \qquad (\text{IV.4.1})$$

following the gradient descent of the considered J_{L^2}, J_{H^1}, J_{H^2} according to (IV.3.10), with suitable parameters $\delta, \gamma > 0$. In each step of the recursion, u^{m-1} is the solution

to (IV.2.1) with $a = a^{m-1}$, and λ^{m-1} is the solution to (IV.3.12) with $a = a^{m-1}$, $u = u^{m-1}$.

For the conjugate gradient method [14], Step 1 is adjusted as follows:

Step 1' (Conjugate gradient method). For $m \geq 1$, in place of (IV.4.1) in Step 1, let a^m be defined by

$$a^m = a^{m-1} + \delta d^{m-1},$$

where

$$d^n = \begin{cases} -g^n & \text{if } n = 0, \\ -g^n + \beta^n d^{n-1}, & \text{otherwise}, \end{cases}$$

and, by (IV.3.10) and the conjugate gradient method,

$$g^n = -s^2 u^n \lambda^n + \gamma(a^n - 1), \quad n \geq 0,$$

$$\beta^n = \frac{\int_\Omega (g^n)^2 \, dx}{\int_\Omega (g^{n-1})^2 \, dx}, \quad n \geq 1.$$

IV.5 Numerical results

To illustrate the performance of the selected functionals and the numerical method for the corresponding optimization problems with PDE constraints, we give two examples: Test 1 – The original coefficient $a(x)$ has three bumps, and Test 2 – $a(x)$ is an annulus with a bump inside. The computational domain will be $\Omega = (0,1)^2$ in both examples.

For the initial guess $a^0 = 1$, we follow the steps outlined in Section IV.4 to update the reconstructed coefficient a^m, and evaluate the relative L^2 error in the reconstruction.

To solve the direct and adjoint problems numerically, we use the numerical PDE tool FEniCS [15]. For a triangulation mesh of Ω, we use Lagrange finite elements. The data $\widetilde{u}$ in Ω are generated by solving (IV.2.1) for a given $a(x)$. The convergence is shown using both gradient descent and conjugate gradient descent method with the stopping criterion that the relative change of the functional between the neighboring iterations is less than a threshold.

In this section, we use the data without noise. A case of noisy data is considered in Section IV.6, which will also be exemplified by the coefficient $a(x)$ of Test 1.

IV.5.1 Test 1

In $\Omega = (0,1)^2$ we consider the following coefficient a, which consists of three bumps on top of the constant 1, as illustrated in Fig. IV.5.1:

$$a(x) = 1 + \sum_{i=1}^{3} C_i \exp\left(-\frac{|x - c_i|^2}{D_i}\right), \qquad \text{(IV.5.1)}$$

with $D_1 = D_2 = D_3 = 1/100$, and

$$C_1 = 4, \ c_1 = (1/4, 1/4); \quad C_2 = 10, \ c_2 = (3/4, 3/4); \quad C_3 = 7, \ c_3 = (7/20, 3/4).$$

Given $\widetilde{u}$ in Ω, generated by solving (IV.2.1) with $a(x)$ defined in (IV.5.1), we aim to reconstruct the coefficient. For the reconstruction algorithm, we set

$$a^0 = 1 \quad \text{in } \Omega,$$

and $s = 3$. For $m = 0, \ldots, 150$, we follow the reconstruction algorithm of Section IV.4, for the functionals J_{L^2}, J_{H^1}, J_{H^2}, given by (IV.3.1)–(IV.3.3), using the parameters $\delta = \gamma = 1/100$. Pictures of the resulting a^m, and the convergence graphs of J_{H^2} for both gradient descent and conjugate gradient method are shown in Fig. IV.5.1 and IV.5.2.
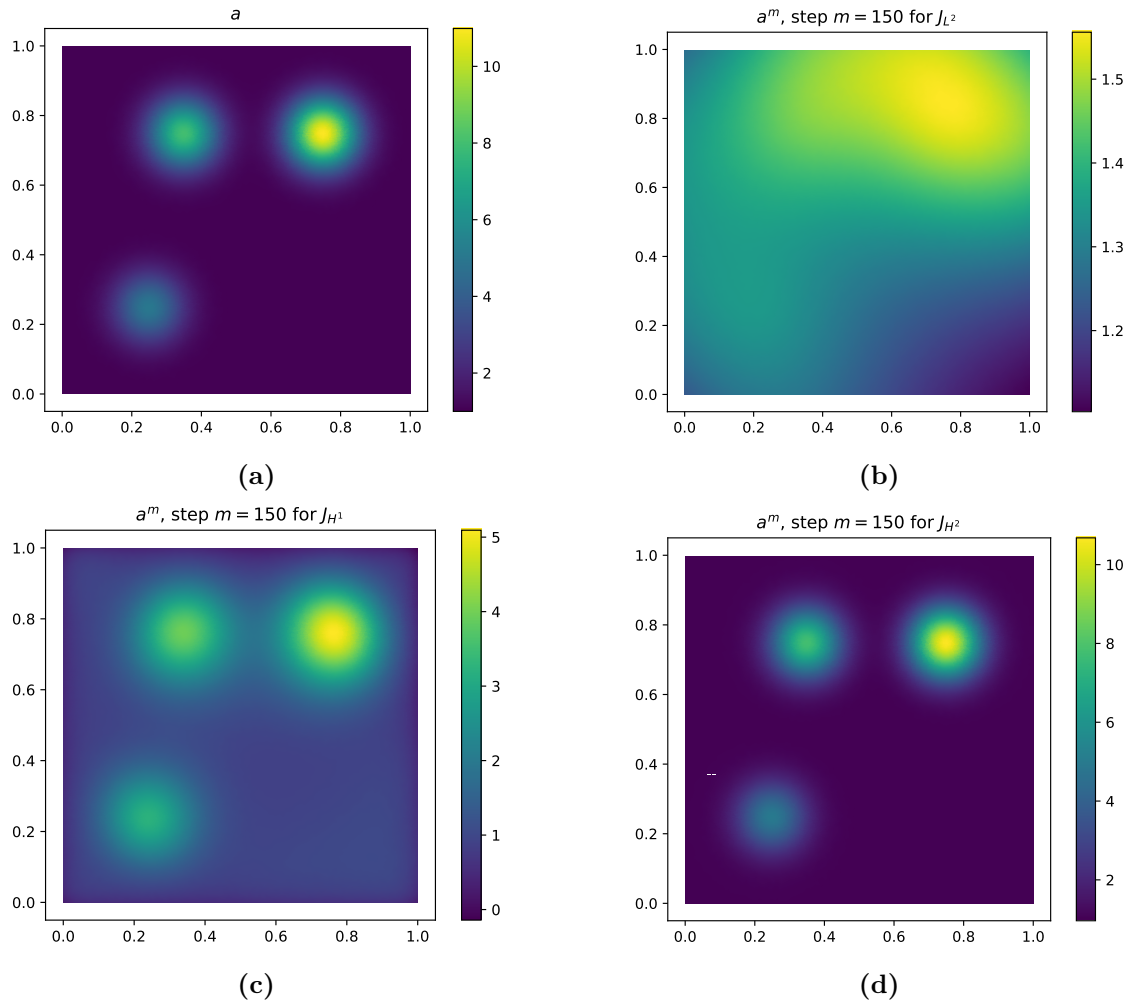

Figure IV.5.1: Reconstruction in Test 1: (a) Original $a(x)$ given by (IV.5.1); (b) Reconstruction using functional J_{L^2}; (c) Reconstruction using functional J_{H^1}; (d) Reconstruction using functional J_{H^2}.

In Fig. IV.5.1, we present the reconstruction for three bumps with different amplitudes, for the three functionals (IV.3.1)–(IV.3.3). We see that the presence of
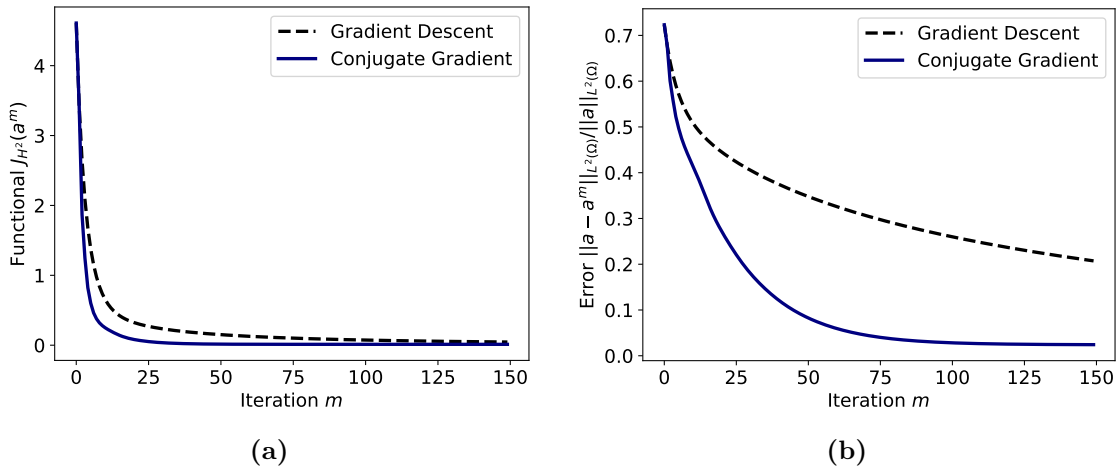
(a)   **(b)**

Figure IV.5.2: Convergence: (a) The value of the functional J_{H^2} vs. iteration number; (b) The relative error $\|a - a^m\|_{L^2(\Omega)}/\|a\|_{L^2(\Omega)}$ in Test 1.

the derivatives in the regularization term improves substantially the quality of the reconstruction. In Fig. IV.5.2, we show the functional value and the relative error $\|a - a^m\|_{L^2(\Omega)}/\|a\|_{L^2(\Omega)}$ depending on the number of iterations for gradient descent and conjugate gradient descent.

IV.5.2 Test 2

The second example is the reconstruction of an annulus with a bump inside. Specifically, the coefficient $a(x)$ is given by

$$a(x) = 1 + C \exp\left(-\frac{|x - c|^2}{D}\right) + C \exp\left(-\frac{\left||x - c|^2 - r^2\right|}{D_1}\right), \qquad (IV.5.2)$$

with

$$C = 4, \ c = (1/2, 1/2), \ r = 1/4, \ D = 1/100, \ D_1 = 1/20.$$

Given $\widetilde{u}$ in Ω, generated by solving (IV.2.1) with $a(x)$ defined in (IV.5.2), we aim to reconstruct the coefficient.

The value of the functional J_{H^2} and the relative L^2-error $\|a - a^m\|_{L^2(\Omega)}/\|a\|_{L^2(\Omega)}$ depending of the number of iterations are shown in Fig. IV.5.4.

IV.6   Noisy data

To evaluate the method for noisy data, we add Gaussian noise to $\widetilde{u}$. To compensate for the increased sensitivity this introduces in the reconstruction algorithm, we smooth $\widetilde{u}$ in the functionals (IV.3.1)–(IV.3.3) using a Savitzky-Golay filter [16]. Furthermore, we modify the gradient descent (IV.4.1) by adding a cutoff ϕ restricting a^m to stay at initial level in the vicinity of the boundary, as well as restricting the resulting a^m to stay withing a given range $[a_{\min}, a_{\max}]$:

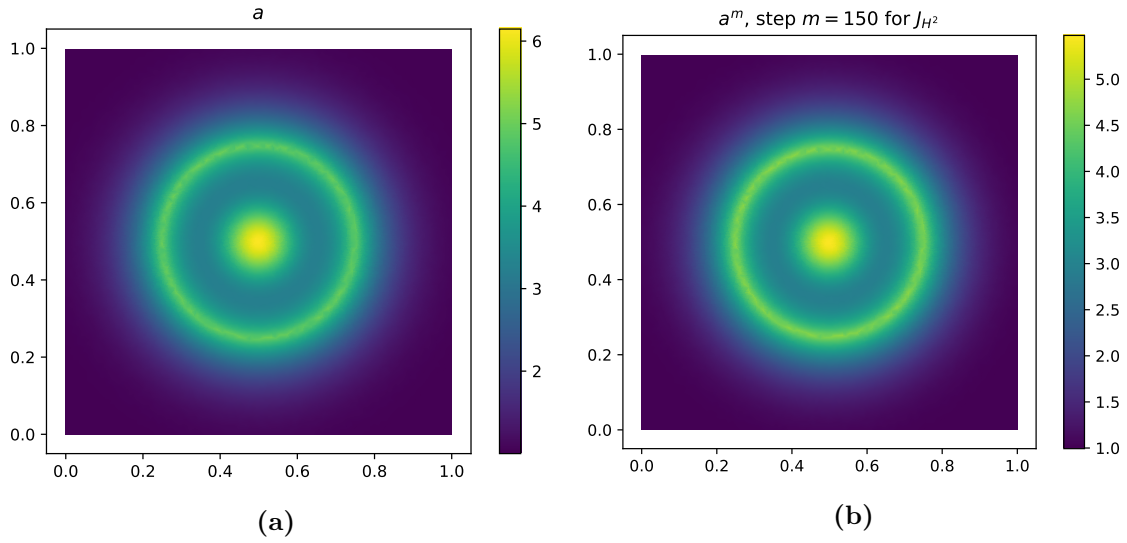$$a^m = a^{m-1} + \delta\phi(s^2 u^{m-1}\lambda^{m-1} - \gamma(a^{m-1} - 1)),$$

Figure IV.5.3: Reconstruction of a in Test 2: (a) Original $a(x)$ given by (IV.5.2); (b) The reconstruction using J_{H^2}.
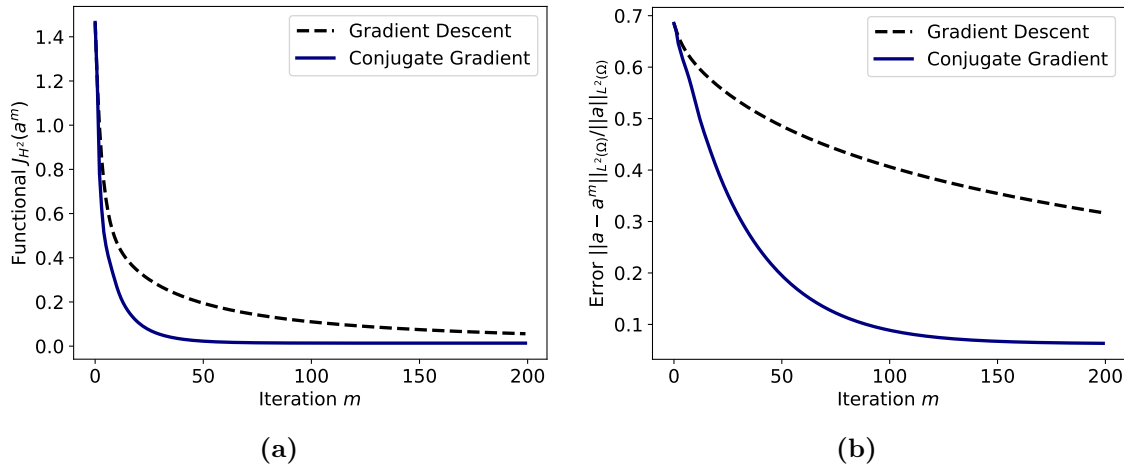

Figure IV.5.4: Convergence in Test 2: (a) Functional J_{H^2} vs. number of iterations; (b) The relative error $\|a - a^m\|_{L^2(\Omega)}/\|a\|_{L^2(\Omega)}$ in Test 2.

and if necessary apply the function $x \mapsto \min\{a_{\max}, \max\{a_{\min}, x\}\}$ on a^m. The conjugate gradient method is modified accordingly.

The noise is modelled by $\widetilde{u} + \alpha v$, where v is normally distributed $N(0, \hat{\sigma}(\widetilde{u})^2)$ with $\hat{\sigma}(\widetilde{u})$ being the numerically estimated standard deviation of the data $\widetilde{u}$, and α being the noise level.

The cutoff function ϕ is chosen as the following Butterworth filter:

$$\phi(x) = \prod_{i=1}^{2} \frac{1}{1 + (2(1 + 2b)x_i - (1 + 2b))^n}. \tag{IV.6.1}$$

As a numerical example we take Test 1 in Section IV.5.1, and use the parameter values specified therein, and set $a_{\min} = 1$, $a_{\max} = +\infty$ as restrictions of a. We consider the noise parameter values $\alpha = 0.05, 0.1$, and 0.5, which represent the

noise levels 5%, 10%, and 50%, respectively. For the cutoff defined in (IV.6.1), we use the parameter values $n = 40$ and $b = 1/40$. The obtained reconstructions are shown in Fig. IV.6.1 and IV.6.2.

After reconstructing a using the functionals J_{L^2}, J_{H^1}, and J_{H^2}, at a noise level of 5%, we observe that the smoothing prior regularizes a, as illustrated in Fig. IV.6.1. For our considered parameter values, the J_{H^1} functional performs best, and in Fig. IV.6.2 we compare various noise levels. We observe that at noise level 10%, the reconstruction is almost on par with the corresponding at 5% (Fig. IV.6.1), and even at a high level of noise 50%, one can visually recognize the original three bumps of Test 1.
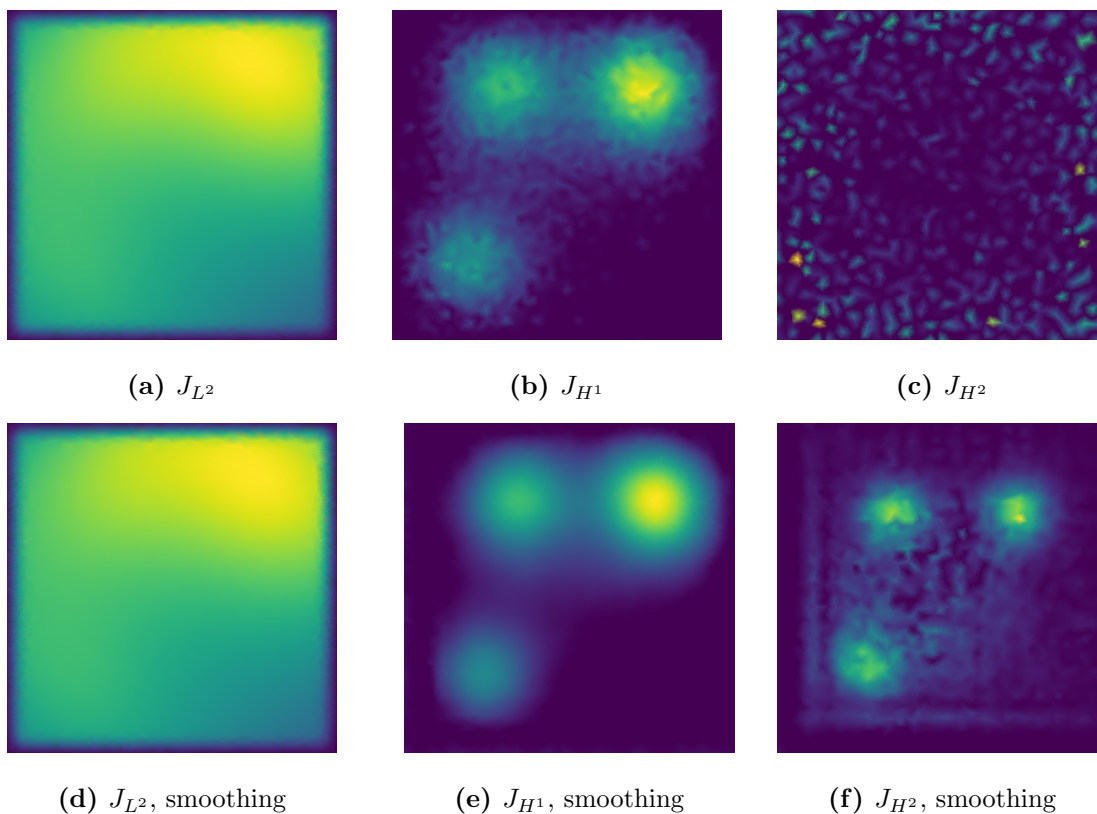

(a) J_{L^2} **(b)** J_{H^1} **(c)** J_{H^2}

(d) J_{L^2}, smoothing   **(e)** J_{H^1}, smoothing   **(f)** J_{H^2}, smoothing

Figure IV.6.1: Reconstruction of $a(x)$ in Test 1 with 5% noise, for functionals (IV.3.1)–(IV.3.3), with and without smoothing.

PAPER IV. ACOUSTIC COEFFICIENT INVERSE PROBLEM

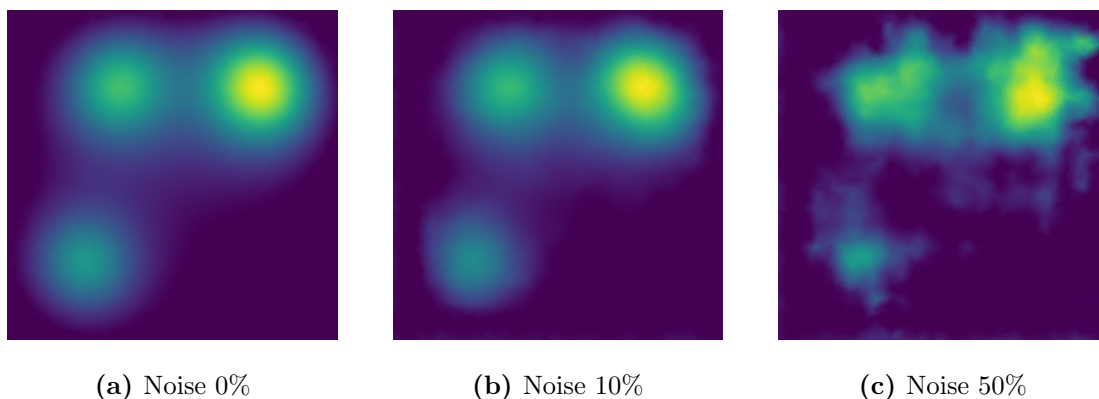(a) Noise 0%   (b) Noise 10%   (c) Noise 50%

Figure IV.6.2: Reconstruction in Test 1 using J_{H^1} and smoothing for various noise levels.

IV.7   Impulse excitation of wave equation

In numerical simulations, impulse excitations are often used to initiate an acoustic wave. For example, a sinusoidal excitation of finite duration is used as an approximation of the derivative of delta function $\delta'(t)$. In this section we justify such approximation. Indeed, let us introduce the sine-impulse $f_\omega(t)$ by

$$f_\omega(t) = \begin{cases} \dfrac{\omega^2}{2\pi}\sin\left(\omega t\right), & \text{for } t \in \left(0, \dfrac{2\pi}{\omega}\right], \\ 0, & \text{otherwise.} \end{cases} \tag{IV.7.1}$$

The following statement holds:

Lemma IV.7.1. *In the sense of distributions, $f_\omega(t)$ converges to the derivative of the delta function, that is*

$$\langle f_\omega, \varphi \rangle \to -\varphi'(0) = \langle \delta', \varphi \rangle, \quad \text{as } \omega \to \infty, \tag{IV.7.2}$$

for any test function φ. Moreover, the corresponding Laplace transforms converge pointwise:

$$\mathcal{L}\{f_\omega\}(s) \to \mathcal{L}\{\delta'\}(s) = s, \quad \text{as } \omega \to \infty. \tag{IV.7.3}$$

Proof. Clearly, $\sin(\omega t)$ is positive for $t \in (0, \frac{\pi}{\omega})$ and negative for $t \in (\frac{\pi}{\omega}, \frac{2\pi}{\omega})$. The function $f_\omega(t)$ can be written as

$$f_\omega(t) = \frac{\omega}{\pi}\left[\frac{\omega}{2}\sin(\omega t)\mathbb{1}_{[0,\frac{\pi}{\omega}]} + \frac{\omega}{2}\sin(\omega t)\mathbb{1}_{[\frac{\pi}{\omega},\frac{2\pi}{\omega}]}\right] = \frac{\omega}{\pi}(g_\omega(t) + h_\omega(t)). \tag{IV.7.4}$$

Since

$$\frac{\omega}{2}\int_0^{\pi/\omega}\sin(\omega t)\,dt = 1,$$

by the mean-value theorem, we have for any smooth φ,

$$\left| \int_{\mathbf{R}} g_\omega(t)\varphi(t)\, dt - \varphi\Big(\frac{\pi}{2\omega}\Big) \right| = \left| \frac{\omega}{2} \int_0^{\pi/\omega} \sin(\omega t)\, dt - \varphi\Big(\frac{\pi}{2\omega}\Big) \right|$$

$$\leq \frac{\omega}{2} \int_0^{\pi/\omega} \sin(\omega t) \big|\varphi(\xi)\big| \Big|t - \frac{\pi}{2\omega}\Big|\, dt \leq \frac{\pi}{2\omega} \max_{0 \leq \xi \leq \pi/(2\omega)} \varphi'(\xi) \int_0^{\pi/\omega} \frac{\omega}{2} \sin(\omega t)\, dt.$$

Thus,

$$\int_{\mathbf{R}} g_\omega(t)\varphi(t)\, dt \to \varphi\Big(\frac{\pi}{2\omega}\Big), \quad \omega \to \infty. \tag{IV.7.5}$$

Similarly,

$$\int_{\mathbf{R}} h_\omega(t)\varphi(t)\, dt \to -\varphi\Big(\frac{3\pi}{2\omega}\Big), \quad \omega \to \infty, \tag{IV.7.6}$$

where the sign in (IV.7.6) comes from the sign of sine on the corresponding interval. Note also that $\varphi(t_0) = \langle \delta(t - t_0), \varphi \rangle$.

Combining (IV.7.4)–(IV.7.6) and using the triangle inequality, we obtain

$$\frac{\pi}{\omega} \int_{\mathbf{R}} f_\omega(t)\varphi(t)\, dt = \int_{\mathbf{R}} g_\omega(t)\varphi(t)\, dt - \varphi\Big(\frac{\pi}{2\omega}\Big) + \int_{\mathbf{R}} h_\omega(t)\varphi(t)\, dt + \varphi\Big(\frac{3\pi}{2\omega}\Big)$$

$$+ \Big(\varphi\Big(\frac{\pi}{2\omega}\Big) - \varphi\Big(\frac{3\pi}{2\omega}\Big)\Big),$$

and thus,

$$\int_{\mathbf{R}} f_\omega(t)\varphi(t)\, dt + \frac{\omega}{\pi}\Big(\varphi\Big(\frac{3\pi}{2\omega}\Big) - \varphi\Big(\frac{\pi}{2\omega}\Big)\Big) \to 0, \quad \omega \to \infty. \tag{IV.7.7}$$

Applying the mean-value theorem one more time, we get

$$\int_{\mathbf{R}} f_\omega(t)\varphi(t)\, dt \to -\varphi'(0), \quad \omega \to \infty.$$

This proves (IV.7.2).

The second statement (IV.7.3) follows from the first one and the Lévy continuity theorem for Laplace transform. In this case, it can also be proved directly, since the Laplace transform of f_ω can be computed exactly:

$$\mathcal{L}\{f_\omega\} = \frac{1}{2\pi}\frac{\omega^3}{\omega^2 + s^2}\Big(1 - e^{-\frac{2\pi}{\omega}s}\Big).$$

By the l'Hôpital rule, $\mathcal{L}\{f_\omega\} \to s$ as $\omega \to \infty$. $\qquad\square$

Conclusion

We present a solution to a CIP problem in the case when the data is given in the pseudo-frequency domain, say after an application of the Laplace transform.

We employ the Lagrangian approach for the optimization of the Tikhonov functional. The focus of the present numerical study is on the effect of derivatives in the functional on the reconstruction. We consider functionals with L^2, H^1, and H^2 regularizing terms for different arrangements of inclusions. The standard functional with a penalty term being the square of the L^2-norm does not produce satisfactory reconstruction results. The best reconstruction for smooth data is obtained, as expected, for the functional containing second derivatives of the solution to the direct problem, in combination with the conjugate gradient method for the functional minimization. For noisy data, we observe that the H^1 functional performs best in combination with suitable smoothing of the input data and constraining of a during the reconstruction procedure.

Acknowledgments

References

[1] L. Beilina, N. T. Thanh, M. V. Klibanov, and J. B. Malmberg. "Reconstruction of shapes and refractive indices from backscattering experimental data using the adaptivity". In: *Inverse Problems* 30.10 (2014), p. 105007.

[2] A. V. Kuzhuget, L. Beilina, M. V. Klibanov, Anders Sullivan, Lam Nguyen, Michael A Fiddy, ARL Team, et al. "Blind backscattering experimental data collected in the field and an approximately globally convergent inverse algorithm". In: *Inverse Problems* 28.9 (2012), p. 095007.

[3] N. T. Thanh, L. Beilina, M. V. Klibanov, and M. A. Fiddy. "Reconstruction of the refractive index from experimental backscattering data using a globally convergent inverse method". In: *SIAM Journal on Scientific Computing* 36.3 (2014), B273–B293.

[4] N. T. Thanh, L. Beilina, M. V. Klibanov, and M. A. Fiddy. "Imaging of buried objects from experimental backscattering time-dependent measurements using a globally convergent inverse algorithm". In: *SIAM Journal on Imaging Sciences* 8.1 (2015), pp. 757–786.

[5] J. D. Joannopoulos, S. G. Johnson, J. N. Winn, and R. D. Meade. "Molding the flow of light". In: *Princet. Univ. Press. Princeton, NJ [ua]* (2008).

[6] A. Greenleaf, Y. Kurylev, M. Lassas, and G. Uhlmann. "Cloaking devices, electromagnetic wormholes, and transformation optics". In: *SIAM review* 51.1 (2009), pp. 3–33.

[7] M. Pastorino. *Microwave imaging.* John Wiley & Sons, 2010.

[8] O. Scherzer. *Handbook of mathematical methods in imaging.* Springer Science & Business Media, 2010.

[9] A. N. Tikhonov. "On the solution of ill-posed problems and the method of regularization". In: *Doklady akademii nauk*. Vol. 151. 3. Russian Academy of Sciences. 1963, pp. 501–504.

[10] K. Ito and B. Jin. *Inverse problems: Tikhonov theory and algorithms*. Vol. 22. World Scientific, 2014.

[11] L. Beilina. "Domain decomposition finite element/finite difference method for the conductivity reconstruction in a hyperbolic equation". In: *Communications in Nonlinear Science and Numerical Simulation* 37 (2016), pp. 222–237.

[12] J. B. Malmberg and L. Beilina. "An Adaptive Finite Element Method in Quantitative Reconstruction of Small Inclusions from Limited Observations". In: *Appl. Math* 12.1 (2018), pp. 1–19.

[13] L. Beilina. *Adaptive hybrid FEM/FDM methods for inverse scattering problems*. Chalmers Tekniska Hogskola (Sweden), 2002.

[14] R. Fletcher and C. M. Reeves. "Function minimization by conjugate gradients". In: *The computer journal* 7.2 (1964), pp. 149–154.

[15] M. S. Alnæs et al. "The FEniCS Project Version 1.5". In: *Archive of Numerical Software* 3.100 (2015). DOI: 10.11588/ans.2015.100.20553.

[16] A. Savitzky and M. J. E. Golay. "Smoothing and differentiation of data by simplified least squares procedures." In: *Analytical chemistry* 36.8 (1964), pp. 1627–1639.

PAPER IV. ACOUSTIC COEFFICIENT INVERSE PROBLEM